

Measurement of the Cross Section for Production
of Two Isolated Prompt Photons in 1.8-TeV
Proton-Antiproton Collisions

Mikio TAKANO

A dissertation submitted to the Doctoral Program
in Physics, the University of Tsukuba, in partial
fulfillment of the requirements for the degree
of Doctor of Philosophy in Physics

June, 1994

Abstract

We present measurements from events with two isolated prompt photons in $\bar{p}p$ collisions at $\sqrt{s} = 1.8$ TeV. The data were accumulated to an integrated luminosity of 4.3 pb^{-1} . Dominant backgrounds to prompt photons are single neutral mesons decaying into multiple photons, which are dissociated from jets. To subtract the backgrounds, the photon identification by the lateral shower profile measured with the strip chamber embedded in the central electromagnetic calorimeter is applied to the data. We obtain $49 \pm 15(\text{stat}) \pm_{-14}^{+20}(\text{syst})$ events in the final diphoton data set. The diphoton events include 1.8 ± 0.6 jets with transverse energy of 4.5 ± 1.9 GeV on average, but no large missing transverse energy. Thus the two-photon system have transverse momentum of 5.1 ± 1.1 GeV/ c on average. The event topology of diphoton production is comparable with that of W boson production. The cross section for photons with transverse momentum p_T in the range of $10 < p_T < 29$ [GeV/ c] is $95 \pm 28(\text{stat}) \pm_{-27}^{+38}(\text{syst})$ pb. The differential cross section, measured as a function of p_T of each photon, is about 3 times what a next-to-leading-logarithm calculation predicts.

Acknowledgements

I would like to thank my advisor, Kunitaka Kondo, for giving me the opportunity to join the CDF experiment and for his support throughout my graduate years. I am also grateful for his careful reading of the text.

I would like to thank Shigeyuki Miyashita who discussed the analysis carefully and gave me many suggestions. I learned a considerable amount from him.

I would like to thank Robert Blair, Stephen Kulmann, Robert M. Harris, and Jae-Chul Yun for their encouragement and advice on the photon analysis.

I would like to thank Teresa Rodrigo and Terence Watts for their careful discussion about the analysis.

I thank Shoji Mikamo who suggested including the diphoton data in the offline DST production.

The great success of the CDF experiment is a result of patient and continuous work of the CDF collaboration.

I thank the Fermilab staff and the technical staffs of the participating institutions for their vital contributions.

I thank Carol Picciolo, Kyoko Kunori, Kazuko Kumashiro, Mutsumi Uenishi, and Yoko Uji-ie for their supports through their secretary work.

I also wish to thank B.Bailey, J.F.Owens, and J.Ohnemus for the results of their calculation.

This work was supported by the U.S. Department of Energy and National Science Foundation, the Italian Istituto Nazionale di Fisica Nucleare, the Ministry of Science, Culture and Education of Japan, the Natural Sciences and Engineering Research Council of Canada, and the Alfred P. Sloan Foundation.

The CDF Collaboration

F. Abe,¹² M. Albrow,⁶ D. Amidei,¹⁵ C. Anway-Wiese,³ G. Apollinari,²³ M. Atac,⁶
 P. Auchincloss,²² P. Azzi,¹⁷ N. Bacchetta,¹⁶ A. R. Baden,⁸ W. Badgett,¹⁵ M. W. Bailey,²¹
 A. Bamberger,^{6,a} P. de Barbaro,²² A. Barbaro-Galtieri,¹³ V. E. Barnes,²¹ B. A. Barnett,¹¹
 P. Bartalini,²⁰ G. Bauer,¹⁴ T. Baumann,⁸ F. Bedeschi,²⁰ S. Behrends,² S. Belforte,²⁰
 G. Bellettini,²⁰ J. Bellinger,²⁸ D. Benjamin,²⁷ J. Benloch,¹⁴ J. Bensinger,² A. Beretvas,⁶
 J. P. Berge,⁶ S. Bertolucci,⁷ K. Biery,¹⁰ S. Bhadra,⁹ M. Binkley,⁶ D. Bisello,¹⁷ R. Blair,¹
 C. Blocker,² A. Bodek,²² V. Bolognesi,²⁰ A. W. Booth,⁶ C. Boswell,¹¹ G. Brandenburg,⁸
 D. Brown,⁸ E. Buckley-Geer,⁶ H. S. Budd,²² G. Busetto,¹⁷ A. Byon-Wagner,⁶ K. L. Byrum,¹
 C. Campagnari,⁶ M. Campbell,¹⁵ A. Caner,⁶ R. Carey,⁸ W. Carithers,¹³ D. Carlsmith,²⁸
 J. T. Carroll,⁶ R. Cashmore,^{6,a} A. Castro,¹⁷ Y. Cen,¹⁸ F. Cervelli,²⁰ K. Chadwick,⁶
 J. Chapman,¹⁵ G. Chiarelli,⁷ W. Chinowsky,¹³ S. Cihangir,⁶ A. G. Clark,⁶ M. Cobal,²⁰
 D. Connor,¹⁸ M. Contreras,⁴ J. Cooper,⁶ M. Cordelli,⁷ D. Crane,⁶ J. D. Cunningham,²
 C. Day,⁶ F. DeJongh,⁶ S. Dell'Agnello,²⁰ M. Dell'Orso,²⁰ L. Demortier,²³ B. Denby,⁶
 P. F. Derwent,¹⁵ T. Devlin,²⁴ M. Dickson,²² S. Donati,²⁰ R. B. Drucker,¹³ A. Dunn,¹⁵
 K. Einsweiler,¹³ J. E. Elias,⁶ R. Ely,¹³ S. Eno,⁴ S. Errede,⁹ A. Etchegoyen,^{6,a} B. Farhat,¹⁴
 M. Frautschi,¹⁶ G. J. Feldman,⁸ B. Flaughner,⁶ G. W. Foster,⁶ M. Franklin,⁸ J. Freeman,⁶
 H. Frisch,⁴ T. Fuess,⁶ Y. Fukui,¹² G. Gagliardi,²⁰ A. F. Garfinkel,²¹ A. Gauthier,⁹ S. Geer,⁶
 D. W. Gerdes,¹⁵ P. Giannetti,²⁰ N. Giokaris,²³ P. Giromini,⁷ L. Gladney,¹⁸ M. Gold,¹⁶
 J. Gonzalez,¹⁸ K. Goulianos,²³ H. Grassmann,¹⁷ G. M. Grieco,²⁰ R. Grindley,¹⁰ C. Grosso-
 Pilcher,⁴ C. Haber,¹³ S. R. Hahn,⁶ R. Handler,²⁸ K. Hara,²⁶ B. Harral,¹⁸ R. M. Harris,⁶
 S. A. Hauger,⁵ J. Hauser,³ C. Hawk,²⁴ T. Hessing,²⁵ R. Hollebeek,¹⁸ L. Holloway,⁹
 A. Hölscher,¹⁰ S. Hong,¹⁵ G. Houk,¹⁸ P. Hu,¹⁹ B. Hubbard,¹³ B. T. Huffman,¹⁹ R. Hughes,²²
 P. Hurst,⁸ J. Huth,⁶ J. Hysten,⁶ M. Incagli,²⁰ T. Ino,²⁶ H. Iso,²⁶ H. Jensen,⁶ C. P. Jessop,⁸
 R. P. Johnson,⁶ U. Joshi,⁶ R. W. Kadel,¹³ T. Kamon,²⁵ S. Kanda,²⁶ D. A. Kardelis,⁹
 I. Karliner,⁹ E. Kearns,⁸ L. Keeble,²⁵ R. Kephart,⁶ P. Kesten,² R. M. Keup,⁹ H. Keutelian,⁶
 D. Kim,⁶ S. B. Kim,¹⁵ S. H. Kim,²⁶ Y. K. Kim,¹³ L. Kirsch,² K. Kondo,²⁶ J. Konigsberg,⁸
 K. Kordas,¹⁰ E. Kovacs,⁶ M. Krasberg,¹⁵ S. E. Kuhlmann,¹ E. Kuns,²⁴ A. T. Laasanen,²¹

S. Lammel,³ J. I. Lamoureux,²⁸ S. Leone,²⁰ J. D. Lewis,⁶ W. Li,¹ P. Limon,⁶ M. Lindgren,³ T. M. Liss,⁹ N. Lockyer,¹⁸ M. Loreti,¹⁷ E. H. Low,¹⁸ D. Lucchesi,²⁰ C. B. Luchini,⁹ P. Lukens,⁶ P. Maas,²⁸ K. Maeshima,⁶ M. Mangano,²⁰ J. P. Marriner,⁶ M. Mariotti,²⁰ R. Markeloff,²⁸ L. A. Markosky,²⁸ J. A. J. Matthews,¹⁶ R. Mattingly,² P. McIntyre,²⁵ A. Menzione,²⁰ E. Meschi,²⁰ T. Meyer,²⁵ S. Mikamo,¹² M. Miller,⁴ T. Mimashi,²⁶ S. Miscetti,⁷ M. Mishina,¹² S. Miyashita,²⁶ Y. Morita,²⁶ S. Moulding,²³ J. Mueller,²⁴ A. Mukherjee,⁶ T. Muller,³ L. F. Nakae,² I. Nakano,²⁶ C. Nelson,⁶ D. Neuberger,³ C. Newman-Holmes,⁶ J. S. T. Ng,⁸ M. Ninomiya,²⁶ L. Nodulman,¹ S. Ogawa,²⁶ C. Pagliarone,²⁰ R. Paoletti,²⁰ V. Papadimitriou,⁶ A. Para,⁶ E. Pare,⁸ S. Park,⁶ J. Patrick,⁶ G. Pauletta,²⁰ L. Pescara,¹⁷ T. J. Phillips,⁵ A. G. Piacentino,²⁰ R. Plunkett,⁶ L. Pondrom,²⁸ J. Proudfoot,¹ F. Ptohos,⁸ G. Punzi,²⁰ D. Quarrie,⁶ K. Ragan,¹⁰ G. Redlinger,⁴ J. Rhoades,²⁸ M. Roach,²⁷ F. Rimondi,^{6,a} L. Ristori,²⁰ W. J. Robertson,⁵ T. Rodrigo,⁶ T. Rohaly,¹⁸ A. Roodman,⁴ W. K. Sakumoto,²² A. Sansoni,⁷ R. D. Sard,⁹ A. Savoy-Navarro,⁶ V. Scarpine,⁹ P. Schlabach,⁸ E. E. Schmidt,⁶ O. Schneider,¹³ M. H. Schub,²¹ R. Schwitters,⁸ G. Sciacca,²⁰ A. Scribano,²⁰ S. Segler,⁶ S. Seidel,¹⁶ Y. Seiya,²⁶ G. Sganos,¹⁰ M. Shapiro,¹³ N. M. Shaw,²¹ M. Sheaff,²⁸ M. Shochet,⁴ J. Siegrist,¹³ A. Sill,²² P. Sinervo,¹⁰ J. Skarha,¹¹ K. Sliwa,²⁷ D. A. Smith,²⁰ F. D. Snider,¹¹ L. Song,⁶ T. Song,¹⁵ M. Spahn,¹³ P. Sphicas,¹⁴ A. Spies,¹¹ R. St. Denis,⁸ L. Stanco,¹⁷ A. Stefanini,²⁰ G. Sullivan,⁴ K. Sumorok,¹⁴ R. L. Swartz, Jr.,⁹ M. Takano,²⁶ K. Takikawa,²⁶ S. Tarem,² F. Tartarelli,²⁰ S. Tether,¹⁴ D. Theriot,⁶ M. Timko,²⁷ P. Tipton,²² S. Tkaczyk,⁶ A. Tollestrup,⁶ J. Tonnison,²¹ W. Trischuk,⁸ Y. Tsay,⁴ J. Tseng,¹¹ N. Turini,²⁰ F. Ukegawa,²⁶ D. Underwood,¹ S. Vejckik, III,¹⁵ R. Vidal,⁶ R. G. Wagner,¹ R. L. Wagner,⁶ N. Wainer,⁶ R. C. Walker,²² J. Walsh,¹⁸ A. Warburton,¹⁰ G. Watts,²² T. Watts,²⁴ R. Webb,²⁵ C. Wendt,²⁸ H. Wenzel,²⁰ W. C. Wester, III,¹³ T. Westhusing,⁹ S. N. White,²³ A. B. Wicklund,¹ E. Wicklund,⁶ H. H. Williams,¹⁸ B. L. Winer,²² J. Wolinski,²⁵ D. Y. Wu,¹⁵ X. Wu,²⁰ J. Wyss,¹⁷ A. Yagil,⁶ W. Yao,¹³ K. Yasuoka,²⁶ Y. Ye,¹⁰ G. P. Yeh,⁶ J. Yoh,⁶ M. Yokoyama,²⁶ J. C. Yun,⁶ A. Zanetti,²⁰ F. Zetti,²⁰ S. Zhang,¹⁵ W. Zhang,¹⁸ S. Zucchelli,^{6,a}

¹ Argonne National Laboratory, Argonne, Illinois 60439

² Brandeis University, Waltham, Massachusetts 02254

³ University of California at Los Angeles, Los Angeles, California 90024

- ⁴ *University of Chicago, Chicago, Illinois 60637*
- ⁵ *Duke University, Durham, North Carolina 27706*
- ⁶ *Fermi National Accelerator Laboratory, Batavia, Illinois 60510*
- ⁷ *Laboratori Nazionali di Frascati, Istituto Nazionale di Fisica Nucleare, Frascati, Italy*
- ⁸ *Harvard University, Cambridge, Massachusetts 02138*
- ⁹ *University of Illinois, Urbana, Illinois 61801*
- ¹⁰ *Institute of Particle Physics, McGill University, Montreal, and University of Toronto, Toronto, Canada*
- ¹¹ *The Johns Hopkins University, Baltimore, Maryland 21218*
- ¹² *National Laboratory for High Energy Physics (KEK), Japan*
- ¹³ *Lawrence Berkeley Laboratory, Berkeley, California 94720*
- ¹⁴ *Massachusetts Institute of Technology, Cambridge, Massachusetts 02139*
- ¹⁵ *University of Michigan, Ann Arbor, Michigan 48109*
- ¹⁶ *University of New Mexico, Albuquerque, New Mexico 87131*
- ¹⁷ *Universita di Padova, Istituto Nazionale di Fisica Nucleare, Sezione di Padova, I-35131 Padova, Italy*
- ¹⁸ *University of Pennsylvania, Philadelphia, Pennsylvania 19104*
- ¹⁹ *University of Pittsburgh, Pittsburgh, Pennsylvania 15260*
- ²⁰ *Istituto Nazionale di Fisica Nucleare, University and Scuola Normale Superiore of Pisa, I-56100 Pisa, Italy*
- ²¹ *Purdue University, West Lafayette, Indiana 47907*
- ²² *University of Rochester, Rochester, New York 15627*
- ²³ *Rockefeller University, New York, New York 10021*
- ²⁴ *Rutgers University, Piscataway, New Jersey 08854*
- ²⁵ *Texas A&M University, College Station, Texas 77843*
- ²⁶ *University of Tsukuba, Tsukuba, Ibaraki 305, Japan*
- ²⁷ *Tufts University, Medford, Massachusetts 02155*
- ²⁸ *University of Wisconsin, Madison, Wisconsin 53706*

Contents

1	Introduction	1
2	The Experimental Apparatus	7
2.1	The Accelerator Complex	7
2.2	The CDF Detector	10
2.2.1	Tracking Chambers	12
2.2.2	Calorimeters	14
2.2.3	Muon Detectors	19
2.2.4	Beam-Beam Counters (BBC)	20
2.2.5	Data Acquisition System	20
3	The Data Acquisition and Reduction	22
3.1	The Trigger Processors	22
3.2	Offline Event Selection	23
3.2.1	EM Cluster Finding	23
3.2.2	CES Cluster Finding	24
3.2.3	Lateral Tower Sharing Algorithm (LSHR)	30
3.2.4	Isolation	30
3.2.5	Selection Criteria for Diphoton Events	32

3.3	Missing E_T in the Diphoton Events	33
3.4	Study of Event Selection Efficiency	35
3.4.1	Level-2 Trigger Efficiency	37
3.4.2	HAD/EM Cut Efficiency	38
3.4.3	LSHR Cut Efficiency	42
3.4.4	Isolation Cut Efficiency	42
4	Photon Identification	47
4.1	Photon Identification Method	48
4.2	χ^2_{CES} Cut Efficiency	49
4.2.1	Photon Efficiency	50
4.2.2	Background Efficiency	52
4.3	Systematics in Photon Efficiency	60
4.3.1	Shower Fluctuations	62
4.3.2	Shower Shape	62
4.3.3	Gas Saturation	64
4.4	Systematics in Background Efficiency	65
5	Data Analysis	68
5.1	Final Event Selection	68
5.1.1	CES Cluster Selection	68
5.1.2	Geometrical Cut	71
5.1.3	Kinematical Cut	71
5.1.4	Final Diphoton Data	72
5.2	Acceptance Calculation	72

5.3	Background Subtraction	79
5.3.1	Diphoton Identification Method	79
5.3.2	Uncertainty in the background subtraction	82
6	Results	85
6.1	Event Topology	85
6.2	Cross Section	92
7	Conclusion	99
A	Diphoton Production Cross Section	100
B	Missing Transverse Energy Significance	106
C	Luminosity Calculation	109

List of Tables

1.1	Comparison of various experiments	4
2.1	Tevatron beam parameters	9
2.2	Summary of CDF calorimeters	14
3.1	Parameters in the CES standard shower profiles	26
3.2	Selection criteria for electrons in the Drell-Yan sample	36
3.3	Parameters for finding EM clusters	38
5.1	Selection criteria for photon candidates	73
5.2	Systematics in the geometrical acceptance	74
5.3	Statistics in the final diphoton data	82
6.1	Number of jets in a diphoton event	89
6.2	Diphoton differential cross section	93
6.3	Theoretical predictions of the diphoton cross section	97

List of Figures

1.1	Diphoton cross section and the reachable region in p_T	5
2.1	FNAL accelerator complex	8
2.2	The CDF detector	11
2.3	Central EM calorimeter	16
3.1	Lateral shower profiles	27
3.2	χ^2 distribution for W electrons	29
3.3	Isolation distribution for photon candidates	31
3.4	\cancel{E}_T significance for the diphoton data	34
3.5	Level-2 trigger efficiency	39
3.6	HAD/EM distribution for electrons in the Drell-Yan sample	41
3.7	LSHR distribution for electrons in the Drell-Yan sample	43
3.8	Border E_T simulation	45
3.9	Isolation cut efficiency	46
4.1	χ^2_{CES} cut efficiency	51
4.2	η mass distribution	53
4.3	χ^2_{Strip} distribution for photons from η decays	54
4.4	π^0 and η mass distribution	56

4.5	ρ^\pm mass distribution	58
4.6	χ^2_{CES} distribution for π^0 's from ρ^\pm decays	59
4.7	Systematics in photon efficiency	61
4.8	Systematics from photon-electron shower shapes	63
4.9	Systematics in background efficiency	67
5.1	Selection efficiency for CES clusters	70
5.2	Acceptance for p_T distribution	75
5.3	Acceptance for z distribution	76
5.4	Acceptance for $\Delta\phi$ distribution	77
5.5	Acceptance for k_T distribution	78
6.1	p_T ratio of two photons in the final diphoton data	86
6.2	$\Delta\phi$ in the diphoton events	88
6.3	k_T distribution	90
6.4	Mean k_T compared with other measurements	91
6.5	Differential cross section compared with UA2 data	95
6.6	Differential cross section compared with theoretical predictions	96
A.1	Feynman diagrams for the diphoton production	105

Chapter 1

Introduction

Hadrons, the generic term for mesons and baryons, have an interaction stronger than the electromagnetic interaction. This interaction is referred to as the strong interaction. Investigation of the strong interaction began with the spectroscopy of hadrons. The spectroscopy of hadrons has led us to the quark model which classifies various hadrons in terms of constituent quarks which are fermions with a quantum number referred to as flavor. The quark model must give quarks another quantum number called color so that two quarks with the same flavor in a hadron can be in the same spin state. The deep inelastic scattering of leptons off nucleons also showed that nucleon is made of constituent particles called partons which are consistent with quarks and massless gluons. Quantum chromodynamics (QCD) describes the strong interaction in terms of the quantum field created by color charges which both quarks and gluons carry. The theory is constructed on the analogy of Quantum electrodynamics (QED). The coupling α_s of the strong interaction becomes weaker at a shorter distance, so that partons are confined within a hadron and are almost free as long as they stay inside a hadron. The feature of the asymptotic freedom allows an application of the perturbative techniques to QCD calculations of hard scattering of partons involving a large momentum transfer.

Experiments of parton scattering normally involve observation of partons in the final states. The color charge of outgoing partons scattered off a hadron causes the vacuum polarization and creates many hadrons with no net color charge. This disintegration process

called fragmentation or hadronization adds more complications, not advantageous to study QCD. Because the kinematics of a scattered parton is determined only by observing final state hadrons coming from the parton, which is called a jet, it depends heavily on jet reconstruction algorithm. Also energy resolution of a hadron calorimeter is worse than that of an electromagnetic shower counter. These two factors make the jet final state ambiguous. In contrast with jets, one can study QCD much better by observing photons. Furthermore, the lowest-order subprocesses are limited to two for double prompt photon production (see Appendix A), while subprocesses for jet production are numerous. Thus several experiments have studied the double prompt photon production in hadron-hadron collisions [43, 44].

In 1982, R806 collaboration reported the first evidence of the diphoton production in hadron-hadron collisions at the CERN Intersecting Storage Rings (ISR) [1]. They observed 31 ± 16 events of the process $pp \rightarrow \gamma\gamma + X$ in which both photons have transverse momentum $p_T > 3 \text{ GeV}/c$ at the center-of-mass energy $\sqrt{s} = 63 \text{ GeV}$. The cross section was

$$\left. \frac{d^2\sigma}{dydM} \right|_{y=0} = 80 \pm 40 \text{ pb}/(\text{GeV}/c^2)$$

for the range of invariant mass $8 < M < 11 \text{ [GeV}/c^2]$. In addition, they measured the ratio of the cross section of the diphoton production to that of the Drell-Yan electron pair production, which was

$$\frac{\sigma(pp \rightarrow \gamma\gamma)}{\sigma(pp \rightarrow e^+e^-)} = 1.7 \pm 1$$

for $p_T > 3 \text{ GeV}/c$.

The Axial Field Spectrometer (AFS) collaboration studied the process $pp \rightarrow \gamma\gamma + X$ at $\sqrt{s} = 63 \text{ GeV}$ at the CERN ISR in 1986 [2]. They observed 23 ± 11 events of the diphoton production. The cross section was

$$\left. \frac{d^2\sigma}{dydM} \right|_{y=0} = 0.55 \pm 0.27 \text{ nb}/(\text{GeV}/c^2)$$

for $4 < M < 6 \text{ [GeV}/c^2]$ and the range of rapidity $|y| < 0.5$. The ratio of the cross section of the diphoton production to that of the Drell-Yan electron pair production was

$$\frac{\sigma(pp \rightarrow \gamma\gamma)}{\sigma(pp \rightarrow e^+e^-)} = 4.0 \pm 3.0$$

for $p_T > 2 \text{ GeV}/c$.

In 1985, NA3 collaboration reported the diphoton production by incident positive and negative beams (π^\pm and p) at $200 \text{ GeV}/c$ interacting with a carbon target at the CERN Super Proton Synchrotron (SPS) [3]. They observed the first experimental evidence for the diphoton production in pion-nucleon interactions. They measured the cross section, which was

$$\sigma(\pi^-C \rightarrow \gamma\gamma + X) = 1.22 \pm 0.35 \text{ nb}$$

for $p_T > 1.8 \text{ GeV}/c$ and $-0.4 < y^* < 1$ in the rest frame.

WA70 collaboration searched the diphoton production by $280\text{-GeV}/c$ π^- beam on a hydrogen target at the CERN SPS in 1989 [4]. They observed 138 ± 23 events of the diphoton production. The cross section was

$$\sigma(\pi^-p \rightarrow \gamma\gamma + X) = 54 \pm 9 \text{ pb}$$

for $p_T^{(1)} > 3.0 \text{ GeV}/c$ and $p_T^{(2)} > 2.75 \text{ GeV}/c$. In 1990, WA70 collaboration presented the correlations of the two photons [5]. They measured transverse momentum of the photon pair (k_T). The mean value of k_T was

$$\langle k_T \rangle = 1.29 \pm 0.10 \text{ GeV}/c.$$

UA1 collaboration reported six candidates of the diphoton production at the CERN $\bar{p}p$ collider at $\sqrt{s} = 630 \text{ GeV}$ in 1988 [6]. They obtained the cross section

$$\sigma_{\gamma\gamma} = 38 \pm 19 \pm 10 \text{ pb}$$

for $p_T > 12 \text{ GeV}/c$ and $|y| < 3$.

In 1992, UA2 collaboration also presented a measurement of the cross section for the diphoton production at the CERN $\bar{p}p$ collider at $\sqrt{s} = 630 \text{ GeV}$ [7]. They took the data corresponding to an integrated luminosity of 13.2 pb^{-1} , and they obtained 58.2 ± 13.4 events of the diphoton production for $p_T > 10 \text{ GeV}/c$ and $|y| < 0.76$.

The comparison of these various experiments is shown in Table 1.1 together with the experiment that we present in this thesis.

Experiment	\sqrt{s} [GeV]	p_T^{\min} [GeV/c]	x_T^{\min}	M [GeV/c ²]
R806 pp	63.0	3.0	0.095	$8 < M < 11$
AFS pp	63.0	2.0	0.063	$4 < M < 6$
NA3 $(\pi^\pm, p)C$	19.4	1.8	0.186	$M > 3.6$
WA70 π^-p	22.9	3.0	0.262	$M > 5.75$
UA1 $\bar{p}p$	630.0	20.0	0.063	$M > 24$
UA2 $\bar{p}p$	630.0	10.0	0.032	$M > 20$
This experiment	1800.0	10.0	0.011	$M > 20$

Table 1.1: Various experiments are compared concerning the center-of-mass energy, minimum p_T , minimum $x_T (= 2p_T/\sqrt{s})$, and mass range.

In this thesis we present the result of yet another data set obtained from proton-antiproton collisions at the center-of-mass energy $\sqrt{s} = 1.8$ TeV. The data were accumulated to an integrated luminosity of $\int \mathcal{L} dt = 4.3 \text{ pb}^{-1}$. We can study the diphoton production at lower $x_T (= 2p_T/\sqrt{s})$ than previous experiments. Comparison of the measured cross section with theoretical predictions is another important motivation of this experiment. A theoretical prediction [45] is shown in Figure 1.1. This is the lowest-order QCD calculation, and is described in Appendix A. The experimentally reachable region in p_T is also indicated in Figure 1.1. We could in principle separate gluon contribution to the cross section from that of quarks at extreme low p_T . Unfortunately, our lower end of p_T is limited by the trigger rate, and therefore no such clear separation is possible. The upper end is limited by the integrated luminosity. Thus we can investigate the diphoton production within the range of p_T from 10 GeV/c to about 25 GeV/c.

The plan for this thesis is as follows: In Chapter 2, the experimental apparatus is explained. In Chapter 3, the data acquisition, reduction, and definitions of several quantities used in this analysis are described, and the efficiency of the event selection is estimated. In Chapter 4, the identification method for photons is described, and the systematic uncertainties are discussed. In Chapter 5, the final event selection is described, and the acceptance

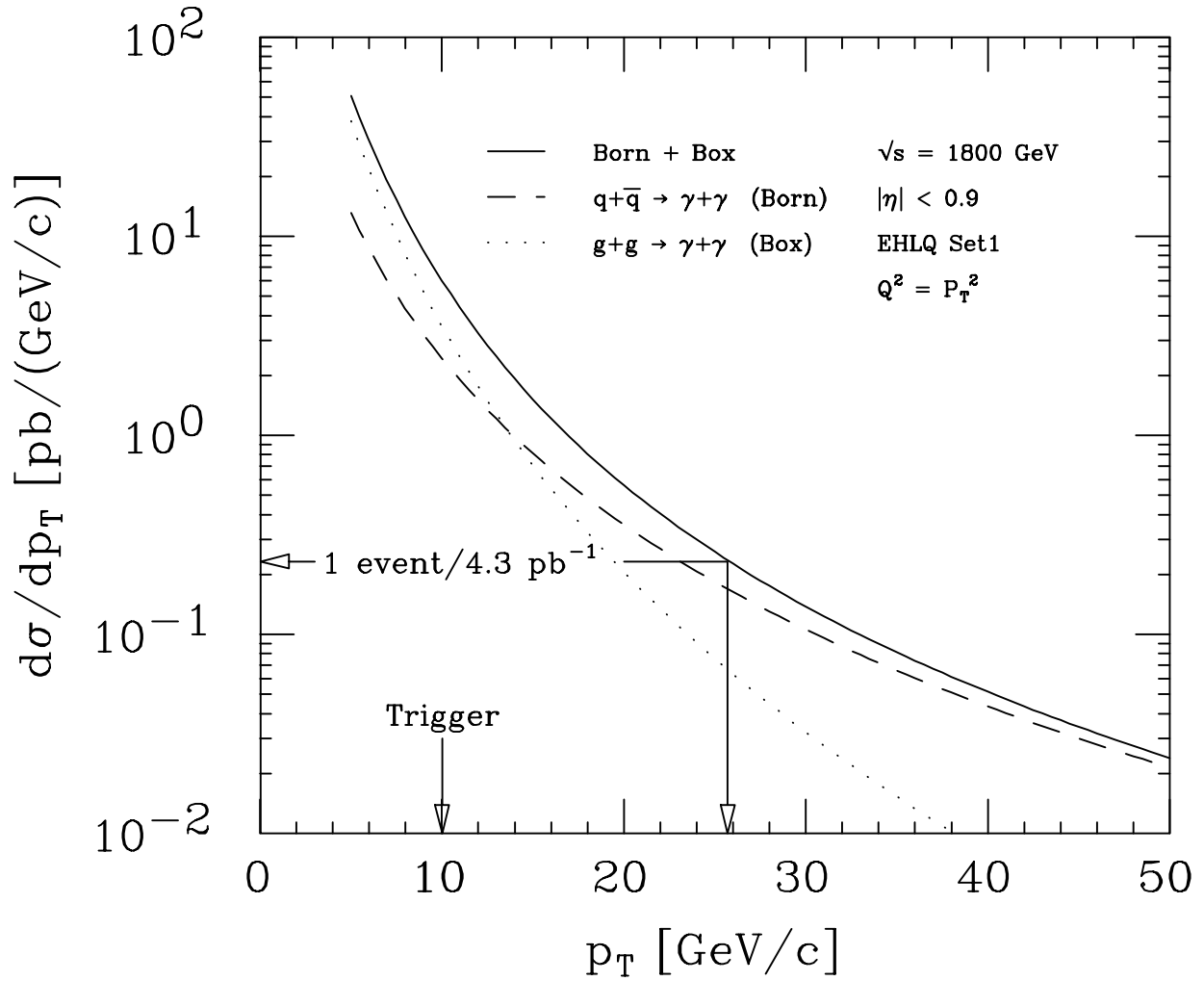


Figure 1.1: A theoretical prediction of the diphoton production including the two lowest-order diagrams (see Appendix A) is shown to indicate the p_T range measured in this experiment. The lower limit is bound by the trigger rate in data acquisition, while the upper limit comes from the integrated luminosity.

for diphoton events is estimated. Furthermore, the background subtraction to get diphoton events is explained, and the statistical and systematic uncertainties are discussed. The background subtraction is based on the photon identification method described in Chapter 4. In Chapter 6, the event topology and the cross section of the diphoton production are discussed. Finally, this study is summarized in Chapter 7.

In addition, there are three appendices: In Appendix A, theoretical predictions of the cross section for the diphoton production are summarized. The theoretical predictions are compared with the data in Chapter 6. In Appendix B, the missing transverse energy significance is explained. This quantity indicates likelihood of normal QCD events for a data set. The missing transverse energy significance for the diphoton data is discussed in Chapter 3. In Appendix C, the luminosity calculation to get the cross section from number of diphoton events is described.

Chapter 2

The Experimental Apparatus

A brief description of the accelerator complex at Fermilab is presented. The CDF detector located at B0 straight intersection of Tevatron consists of a large number of components. We describe these components relevant to this thesis in somewhat more detail.

2.1 The Accelerator Complex

The particle accelerator complex which makes proton-antiproton collisions at Fermilab consists of five stages. In the Cockcroft-Walton, a large DC voltage accelerates negative hydrogen ions to 750 keV. The Linac which is a 500-foot long linear accelerator accelerates the negative hydrogen ions coming from the Cockcroft-Walton to 200 MeV. The two electrons are stripped off the negative hydrogen ions. Protons are injected into the Booster which is a synchrotron with a radius of 250 feet located in a tunnel 20 feet below the ground. The protons accelerated by the Booster to 8 GeV are injected into the Main Ring which is a synchrotron with a radius of 1 km, and are accelerated to 150 GeV. The Main Ring consists of water-cooled magnets operated at room temperature in an underground tunnel. The Tevatron which consists of superconducting magnets cooled by liquid helium to 4.5 K lies under the Main Ring. The protons are accelerated to 900 GeV in the Tevatron. An overview of the accelerator complex is shown in Figure 2.1.

Figure 2.1: A schematic view of the FNAL accelerator complex is shown.

The Main Ring is also used to produce antiprotons. A pulse of 2×10^{12} protons accelerated to 120 GeV in the Main Ring are introduced to an antiproton production target every 2 seconds. About 10^7 antiprotons produced in the target are collected in a Debuncher ring and is made more dense by a process called stochastic cooling. The antiprotons accumulated in the Accumulator ring are cooled further. The Debuncher and Accumulator rings are operated at 8 GeV, the same energy as the Booster. Very dense bunches of antiprotons are extracted from the Accumulator ring, and are injected into the Main Ring at 8 GeV. The antiprotons are accelerated to 150 GeV in the Main Ring. The antiprotons circulate counterclockwise in the Main Ring and the Tevatron, whereas the protons circulate clockwise. Antiprotons passed down to the Tevatron are accelerated simultaneously with protons to 900 GeV.

Beam momentum	P	900 GeV/ c
Radius	ρ	1000 m
Number of bunches	N_B	6
Number of protons	N	7.0×10^{10} /bunch
Number of antiprotons	\bar{N}	2.5×10^{10} /bunch
Transverse emittance (p)	$\epsilon_{95\%}$	25π mm mrad
Transverse emittance (\bar{p})	$\bar{\epsilon}_{95\%}$	18π mm mrad
Beta	β	0.5 m
Initial lifetime	τ	20 hours
Luminosity	\mathcal{L}	1.8×10^{30} cm ⁻² s ⁻¹

Table 2.1: Summary of beam parameters corresponding to the best typical performance of the Tevatron collider.

Summary of Tevatron beam parameters is shown in Table 2.1. The emittance including

95% of the beam particles, $\epsilon_{95\%}$, is written as

$$\epsilon_{95\%} = 1.96\pi \cdot \epsilon \quad (2.1)$$

where ϵ denotes the transverse emittance described in Appendix C. We can calculate the luminosity \mathcal{L} from those beam parameters. The accelerator luminosity \mathcal{L} is given as

$$\mathcal{L} = N_B \cdot \frac{c}{2\pi\rho} \cdot \frac{N\bar{N}}{4\beta \frac{\epsilon + \bar{\epsilon}}{2} \cdot \frac{cP}{mc^2}} \quad (2.2)$$

where symbols are defined in Table 2.1. This formula is also mentioned in Appendix C. The luminosity \mathcal{L} was typically $1.8 \times 10^{30} \text{ cm}^{-2}\text{s}^{-1}$ during the 1988–1989 collider run.

2.2 The CDF Detector

A schematic view of the CDF detector is shown in Figure 2.2. The origin of the standard CDF coordinate system is the center of the CDF detector, which is the nominal interaction point. The positive Z axis is in the direction of the proton beam which runs from the west to the east at B0 straight intersection where the CDF detector is located. The positive Y axis is vertical. The positive X axis points out of the Tevatron ring. The polar angle θ is zero along positive Z axis. Instead of the polar angle, the pseudorapidity $\eta = -\ln \tan \frac{\theta}{2}$ is often used. The azimuthal angle ϕ is zero along the positive X axis and increases from the positive Y axis to the negative Y axis. The radius R is defined as a perpendicular distance from the Z axis, that is, the beam line. The standard CDF coordinate system is left-handed. Because the kinematics is described by the transverse momentum, pseudorapidity, and azimuthal angle, the CDF detector is approximately cylindrically symmetric, and the segmentation is roughly uniform in pseudorapidity and azimuthal angle.

The CDF detector consists of a central detector and two identical forward/backward detectors. The central detector is made up of the superconducting solenoid coil, steel magnet yoke, tracking chambers, electromagnetic shower counters, hadron calorimeters, and muon chambers. The forward/backward detectors are consisting of segmented time-of-flight counters, electromagnetic shower counters, hadron calorimeters, and muon toroidal spectrometers. In this chapter, we describe briefly each individual component of the CDF detector.

Figure 2.2: Cross section through a vertical plane of one half the CDF detector. The detector is symmetric about the midplane and roughly symmetric around the beam axis.

2.2.1 Tracking Chambers

There are three separate tracking systems in the CDF central detector. These tracking systems are inside the superconducting solenoid coil. Immediately outside the beam pipe, eight small vertex time projection chambers (VTPC) track charged particles and give good pointing in the θ direction to determine the event vertex. The central tracking chamber (CTC) is a large cylindrical drift chamber with excellent spatial and momentum resolutions, and is used to measure charged tracks in the central region. The central drift tubes (CDT) with high resolution charge division surrounding the CTC provide a correlated $R\phi$ - Z measurement. In the following, we describe briefly each individual component of tracking systems.

Vertex Time Projection Chamber (VTPC)

The VTPC [9] comprises of eight separate time projection chambers which are mounted end-to-end along the beam direction. The 287-cm total length of the chamber covers well the long interaction region ($\sigma_Z \approx 35$ cm). The VTPC contains a total of 3072 sense wires for the measurement of track coordinates in R - Z , and 3072 pads for the measurement of track coordinates in R - ϕ . Each module has a central high voltage grid that divides it into two 15.25-cm long drift regions. At the end of each drift region there are proportional chambers arranged in octants. Each octant has 24 anode sense wires and 24 cathode pads. The active area of the chamber extends from $R = 6.8$ cm to $R = 21$ cm.

Since particles detected by the calorimeters and other tracking chambers first pass through the VTPC, a considerable effort is made to minimize the mass of the VTPC and the beam pipe. The beam pipe, inside the VTPC, consists of a 5.08-cm diameter beryllium tube, with a wall thickness of 500 μm . The amount of material traversed is lowest over the angular region of full coverage by the CTC ($50^\circ < \theta < 130^\circ$). In this region a particle on average passes through less than 3.2% of a radiation length before entering the CTC. A photon can interact with the material and create an electron and a positron. The probability of the photon conversion is less than 2.5%.

The Z position resolution per hit is about 200 μm near the sense wires and about 550

μm for the longest drift times. The impact parameter of tracks with the primary vertex has the RMS of about 0.3 cm.

Central Tracking Chamber (CTC)

The CTC [10] is a 138-cm radius, 320-cm long cylindrical drift chamber which allows precise momentum measurements in the angular region $40^\circ < \theta < 140^\circ$ ($|\eta| < 1$). The chamber contains 84 layers of sense wires grouped into 9 superlayers. Five of the superlayers consist of 12 axial sense wires. Four stereo superlayers consist of 6 sense wires tilted by $\pm 3^\circ$ relative to the beam direction. The position resolution for each hit is better than $200 \mu\text{m}$ in $R\phi$ and 6 mm in Z . The momentum resolution is better than $\delta p_T/p_T^2 < 0.002 (\text{GeV}/c)^{-1}$. By using the constraint that the track originates at the interaction vertex, the improves to $\delta p_T/p_T^2 < 0.0011 (\text{GeV}/c)^{-1}$.

Central Drift Tube (CDT)

The CDT [11] consists of three layers of 3-m long, 1.27-cm diameter stainless steel tubes mounted on the outer cylindrical surface of the CTC, and just inside the superconducting solenoid coil. High accuracy $R\phi$ - Z information for tracking charged particles at a radius of 140 cm is obtained by making both drift time and charge division measurements. Typical resolutions are $200 \mu\text{m}$ in the azimuthal direction ($R\phi$) and 2.5 mm in the beam direction (Z).

Superconducting Solenoid Coil

The CTC which is in a uniform 1.4116-T magnetic field oriented along the beam direction provides precise momentum determination for charged particles produced in the central region. The magnetic field is produced by a 3-m diameter 5-m long superconducting solenoid coil. The overall radial thickness of the solenoid coil is 0.85 radiation length. The thickness can not be ignored to study the fluctuation and shape of electromagnetic showers in the central calorimeter. When the central calorimeter is tested with the test beam, the coil

simulator is put in front of the central calorimeter.

2.2.2 Calorimeters

All calorimeters in the CDF detector have projective tower geometry. The towers point at the nominal interaction point, that is, the origin of the CDF detector. Each tower is separated into two components in depth. In each tower, an electromagnetic (EM) shower counter is placed in front of a corresponding hadron (HAD) calorimeter. Each EM calorimeter has depth enough to contain an EM shower induced by an energetic electron or photon. Hence both energy of an electron and that of a photon are measured only with an EM calorimeter. While energy of a jet which is a collection of hadrons is measured with both EM and HAD calorimeters. Calorimeters in the CDF detector are summarized in Table 2.2 with respect to the η coverage, tower size $\Delta\eta \times \Delta\phi$, and energy resolution σ/E which is described as a function of the energy E measured in GeV. An operator symbol \oplus used in the energy resolution indicates a square root of addition in quadrature as $a \oplus b = \sqrt{a^2 + b^2}$. In the following, we describe each calorimeters.

Component	η range	$\Delta\eta \times \Delta\phi$	σ/E
CEM	$ \eta < 1.1$	$0.11 \times 15^\circ$	$13.5\%/\sqrt{E \sin \theta} \oplus 2\%$
PEM	$1.1 < \eta < 2.4$	$0.09 \times 5^\circ$	$28\%/\sqrt{E} \oplus 2\%$
FEM	$2.2 < \eta < 4.2$	$0.1 \times 5^\circ$	$25\%/\sqrt{E} \oplus 2\%$
CHA/WHA	$ \eta < 1.3$	$0.11 \times 15^\circ$	$75\%/\sqrt{E \sin \theta} \oplus 3\%$
PHA	$1.3 < \eta < 2.4$	$0.09 \times 5^\circ$	$90\%/\sqrt{E} \oplus 4\%$
FHA	$2.2 < \eta < 4.2$	$0.1 \times 5^\circ$	$130\%/\sqrt{E} \oplus 4\%$

Table 2.2: Every calorimeter is summarized with respect to the η coverage, tower size $\Delta\eta \times \Delta\phi$, and energy resolution σ/E . An operator symbol \oplus means $a \oplus b = \sqrt{a^2 + b^2}$. The energy resolution is described as a function of the energy E measured in GeV.

Central Electromagnetic Calorimeter (CEM)

The CEM [12] covers the region of $39^\circ < \theta < 141^\circ$ ($|\eta| < 1.1$) and 2π in ϕ , and consists of 48 modules which surround the superconducting solenoid coil. Each module covers $39^\circ < \theta < 90^\circ$ or $90^\circ < \theta < 141^\circ$ and 15° in ϕ . The end plates of the θ boundary are made of 1-inch thick iron, and the skin of the ϕ boundary is $\frac{3}{16}$ -inch thick steel. An inner aluminum base plate begins the CEM at a perpendicular radius of 68 inches from the beam line. Its normal 1 inch thickness is reduced in pockets down to $\frac{3}{8}$ inch. The average thickness is only 0.55 inch. 31 layers of 5-mm thick scintillator are assembled to form 10 projective towers, each subtending 0.11 in η and 15° in ϕ . Towers are numbered from 0 to 9 as $|Z|$ of the tower center increases as shown in Figure 2.3. 30 layers of $\frac{1}{8}$ -inch lead are inserted between scintillators. In order to maintain both a uniform radiation length thickness up to a proportional strip chamber embedded in each module and a uniform total thickness, as the polar angle varies, acrylic is substituted for lead in certain layers for towers. The thickness up to the proportional strip chamber from the aluminum base plate is $5 X_0$, and the total thickness is $18 X_0$. X_0 is a unit of the radiation length, and is equivalent to 6.37 g/cm^2 (0.56 cm) for lead. The energy resolution for electrons is well described as a function of both the energy measured in GeV and the polar angle.

$$\frac{\sigma}{E} = \frac{13.5\%}{\sqrt{E \sin \theta}} \oplus 2\% \quad (2.3)$$

The proportional strip chamber (CES) is inserted inside the stack between the eighth lead layer and the ninth scintillator layer in each module, and covers all ten towers. A three-piece aluminum extrusion is used as a base to form the cells which are 0.250 inch deep by 0.239 inch wide. 62 anode wires are strung in the beam direction in the cells and ganged together in pairs except for two edge wires. The logical channel width is 1.453 cm. The wires are divided at tower 4 and 5 boundary giving a total of 64 channels per module. The strips are copper-backed $\frac{1}{16}$ inch PC boards. The 128 cathode strips are oriented perpendicular to the wires. The width is 16.67 mm for towers 0 to 4 (69 strips, $6.16 < Z < 121.16$ [cm]) and 20.07 mm for towers 5 to 9 (59 strips, $121.16 < Z < 239.56$ [cm]). The position resolution is typically ± 2 mm for 50 GeV electrons.

Figure 2.3: Schematics of a module of the central electromagnetic calorimeter is show together with the local coordinate system.

End Plug Electromagnetic Calorimeter (PEM)

The PEM [14] covers $1.1 < |\eta| < 2.4$ and 2π in ϕ . Each of the two modules consists of four quadrants of $\Delta\phi = 90^\circ$ each. Each quadrant consists of 34 layers of proportional tube arrays with 2.7-mm thick lead absorber panels. The tube array are sandwiched by front and rear G-10 PC boards. Pads are etched on one side directly facing the tube array on the front G-10 PC board. In the polar angle, the segmentation is $\Delta\eta = 0.09$ between 1.41 and 2.4 in η , and smaller for $1.1 < |\eta| < 1.41$. The azimuthal segmentation is $\Delta\phi = 5^\circ$. Longitudinally cathode pads are ganged together at each of the polar coordinates (η, ϕ) into three projective towers. The first segment contains the first 5 layers, the second segment the next 24 layers, and the third segment the last 5 layers, respectively. The total thickness is $18 X_0$ in the Z direction. The energy resolution is described as

$$\frac{\sigma}{E} = \frac{28\%}{\sqrt{E}} \oplus 2\% \quad (2.4)$$

where the energy E is measured in GeV.

Besides the pads, the first 10 layers of the second longitudinal segment have strips of two types on the rear side G-10 panels. The patterns are orthogonal to each other. The five odd-numbered layers have θ -strips which are 32 arc-shaped strips of $\Delta\eta = 0.02$ stretched by 30° in ϕ , and the remaining five even-numbered layers have ϕ -strips which are 30 radial strips of $\Delta\phi = 1^\circ$. The coverage of these strips in polar angles is limited to the region of $1.2 < |\eta| < 1.84$. All five θ -strips are ganged together in depth at the same (η, ϕ) coordinates also forming well defined projective towers. The ϕ -strips are also ganged in the same way as the θ -strips. The θ - and ϕ -strips are useful for determining the center position of an EM shower in the region where the pad size is as large as the EM shower size.

Forward/Backward Electromagnetic Calorimeter (FEM)

The FEM [15] are located approximately 6.5 m from the interaction point and enclose the beam pipe at either end of the CDF detector. Each calorimeter consists of 30 sampling layers, each of which is composed of a 0.48-cm thick lead sheet and a chamber of gas proportional tubes. The total thickness is $25 X_0$ in the Z direction. Each cathode pad subtends 0.1 in η ,

and 5° in ϕ . The pads are ganged longitudinally into towers with two depth segmentations, both of which are 15 layers thick. The cathode pads are scaled in size every other layer so that the resultant towers project back to the nominal beam-beam interaction point. The energy resolution is described by

$$\frac{\sigma}{E} = \frac{25\%}{\sqrt{E}} \oplus 2\%, \quad (2.5)$$

where E is the energy measured in GeV.

Central and Endwall Hadron Calorimeter (CHA and WHA)

The CHA and WHA [16] covers the polar angle region of $30^\circ < \theta < 150^\circ$ ($|\eta| < 1.3$) and 2π in ϕ . The hadron calorimeter in the central region consists of 48 modules of the CHA and 48 modules of the WHA. Each hadron calorimeter module is divided into projective towers, each covering approximately 0.11 in η and 15° in ϕ , matching those of the CEM. This segmentation is fine enough that a jet will normally spread over more than one tower. The CHA module, covering polar angles between 45° and 135° , consists of 32 layers of 2.5-cm thick steel plate and 1.0-cm thick scintillator. The total thickness of the CHA is $4.7 \lambda_I$. λ_I is a unit of the nuclear interaction length, and is equivalent to 132 g/cm^2 (16.8 cm) for steel. The WHA module, covering polar angle regions of $30^\circ < \theta < 45^\circ$ and $135^\circ < \theta < 150^\circ$, consists 15 layers of 5.0-cm thick steel plate and 1.0-cm scintillator. The total thickness of the WHA is $4.5 \lambda_I$. The energy resolution of both calorimeters for pions is described as

$$\frac{\sigma}{E} = \frac{75\%}{\sqrt{E \sin \theta}} \oplus 3\%, \quad (2.6)$$

where E is the energy measured in GeV.

End Plug Hadron Calorimeter (PHA)

The PHA [8] covers the range of $1.3 < |\eta| < 2.4$ with full azimuthal coverage. This calorimeter are composed of 20 layers of 5.0-cm thick steel plate and 20 proportional chambers which are located between neighboring steel plates. The total thickness is $5.7 \lambda_I$ in the Z direction. The signals from each cathode pad at a certain η and ϕ are summed together to produce

the total energy signal for a given projective tower. Each projective tower has a size of $\Delta\eta \times \Delta\phi = 0.09 \times 5^\circ$. The energy resolution is described as

$$\frac{\sigma}{E} = \frac{90\%}{\sqrt{E}} \oplus 4\%, \quad (2.7)$$

where E is the energy measured in GeV.

Forward/Backward Hadron Calorimeter (FHA)

The FHA [17] covers the range of $2.2 < |\eta| < 4.2$ with full azimuthal coverage. Each of the forward and backward calorimeters are segmented into four independent sections. These calorimeter segments are each composed of 27 layers of 5.0-cm thick steel plate and 27 proportional chambers which are located between neighboring steel plates. The cathode surface of each of the proportional chambers has been segmented into 20 bins in η ($\Delta\eta = 0.1$) and 18 bins in ϕ ($\Delta\phi = 5^\circ$). The total thickness is $7.7 \lambda_I$ in the Z direction. Cathode pads at a certain η and ϕ on each of the 27 proportional chambers form a projective tower whose apex is the interaction point at a distance of 711 cm from the calorimeter face. The signals from each cathode pad at a certain η and ϕ are summed together to produce the total energy signal for a given projective tower. The energy resolution is described as

$$\frac{\sigma}{E} = \frac{130\%}{\sqrt{E}} \oplus 4\%, \quad (2.8)$$

where E is the energy measured in GeV.

2.2.3 Muon Detectors

There are two systems in the CDF detector to measure muons which penetrate the calorimeters. In the central detector, each module contains 4 layers of muon chambers (CMU) [18] outside of the hadron calorimeter. In each of the forward and backward regions there is a muon spectrometer (FMU) [19] consisting of large magnetized steel toroids with drift chamber planes and triggering scintillation counters. Since we are not concerned with muon detection in this thesis, not even for calculating the missing transverse momentum, we do not go into further detail. As described in Appendix B, the missing transverse momentum

is solely calculated from calorimetry energy deposits. This is justified as high- p_T muons are extremely rare and its contribution is negligible.

2.2.4 Beam-Beam Counters (BBC)

There is a plane of scintillation counters on the front face of each of the forward and backward calorimeters. These scintillation counters (BBC) [8] provide a minimum-bias trigger for the CDF detector, and are also used as the primary luminosity monitor. The BBC have excellent timing resolution ($\sigma < 200$ ps), hence provide the best measurement of the time of the interaction. A crude (± 4 cm) measurement of the vertex position is also obtained from the timing. The scintillation counters are arranged in a rectangle around the beam pipe. They cover the angular region (measured along either the horizontal or vertical axes) from 0.32° to 4.47° ($3.24 < |\eta| < 5.88$). The minimum bias trigger requires at least one counter in each plane to fire within a 15-ns window centered on the beam crossing time.

2.2.5 Data Acquisition System

The CDF data acquisition employs extensively a FASTBUS system coupled to the front-end electronics receiving signals from various parts of the CDF detector [21]. A special crate-based analog front-end system called the RABBIT system [20] is developed to deal with a large number of channels and a very large dynamic range for the calorimetry. Signals from the tracking chambers are sent to commercial FASTBUS TDC modules.

The trigger [22] uses the projective geometry of the calorimeter towers. Both electromagnetic and hadron calorimeter towers are summed into a trigger tower with a size of $\Delta\eta \times \Delta\phi = 0.2 \times 15^\circ$. This results in $42(\text{in } \eta) \times 24(\text{in } \phi)$ trigger towers for both EM and HAD calorimeters. The signals are weighted by $\sin\theta$ to get the transverse energy E_T deposited in the trigger tower.

The level-1 trigger requires that the sum of E_T for all towers with E_T over a tower threshold is greater than a trigger threshold. Both EM and HAD energies, or either one can be summed in every tower.

The level-2 trigger starts after the level-1 trigger has accepted an event. The level-2 trigger uses the same 42×24 trigger towers as the level-1 trigger for clustering trigger towers with E_T greater than a tower threshold. For every cluster a match is made to tracks found in the CTC by the fast hardware tracking processor [23].

The level-3 trigger system is designed to execute FORTRAN-77 filter algorithms as the last stage of online trigger selection. The system consists of Advanced Computer Programs (ACP) 32-bit processors installed in VME crates together with VME bus control and interface modules. Events which pass the level-3 filter algorithm are written to tapes for offline analysis.

The system through-put is approximately a few events/s which necessitates a rather elaborated trigger system. This is the reason for the lower limit of photon p_T as already mentioned in the introduction. Since the trigger process generates biases and affects acceptance of the data acquired, we describe somewhat more in detail the trigger process in the next chapter.

Chapter 3

The Data Acquisition and Reduction

The data analyzed in this thesis were accumulated to the integrated luminosity of 4.3 pb^{-1} during the 1988–1989 collider run. In this chapter, the trigger process and the subsequent data reduction are described. The trigger and data reduction efficiencies are also discussed in detail.

3.1 The Trigger Processors

The trigger process which diphoton events should pass through in the data acquisition consists of four levels. The level-0 trigger which selects inelastic collisions requires that the BBC's on both sides of the central detector are hit in coincidence. This is the minimum-bias trigger. The cross section of the level-0 trigger is about 47 mb.

The level-1 trigger uses fast outputs from calorimeters for fast decisions. In order to reduce the number of trigger towers, every two towers in η in the central calorimeter are combined to form a trigger tower. There are altogether $10(\text{in } \eta) \times 24(\text{in } \phi)$ trigger towers in the central region. Each trigger tower is divided into the electromagnetic (EM) and hadronic (HAD) parts. The fast outputs are weighted by $\sin \theta$ to get the transverse energies (E_T) in the trigger towers. The level-1 trigger for diphoton events requires the sum of E_T over all EM trigger towers with E_T of at least 4 GeV to be greater than 7 GeV. The cross section of

the level-1 trigger is about $79 \mu\text{b}$.

At the level-2 trigger, EM clusters are formed out of EM trigger towers. EM trigger towers with E_T of at least 4 GeV are selected as seed towers for finding level-2 EM clusters. If adjacent towers of a seed tower have EM E_T greater than the tower threshold of 3.6 GeV, the towers are included into the EM cluster. Until there is no adjacent tower with EM E_T over the tower threshold around the EM cluster, this clustering procedure is continued. The number of trigger towers in the level-2 EM cluster is limited to 15 towers. Furthermore, the level-2 EM cluster is required for a ratio of the hadronic transverse energy to the electromagnetic one, HAD/EM, to be less than 0.125. For diphoton events, the level-2 trigger requires two or more level-2 EM clusters with EM E_T greater than 10 GeV. The cross section of the level-2 trigger is about 92 nb.

At the level-3 trigger, a truncated version of the offline program is operating in ACP processors installed in parallel, but diphoton events pass through without any cuts.

3.2 Offline Event Selection

Algorithms for finding EM clusters and CES clusters, and selection criteria for diphoton events in the central region are described. The selection criteria consists of standard cuts for photons and electrons and an isolation cut for background reduction. In the CES cluster finding, a standard lateral shower profile is fitted to each CES cluster to determine the shower center position. A measure of the goodness of fit, χ_{CES}^2 , is used for identification of photons.

3.2.1 EM Cluster Finding

Photons and electrons are observed as energy clusters in an EM calorimeter. EM energy E^{EM} and HAD energy E^{HAD} measured in each tower are multiplied by $\sin \theta$ calculated from the tower center position and the event vertex position determined with the VTPC to be converted into transverse energies E_T^{EM} and E_T^{HAD} . The clustering algorithm in the central region finds out seed towers with E_T^{EM} greater than the seed tower threshold of 3 GeV, and

adds two neighboring towers in η with E_T^{EM} greater than the tower threshold of 0.1 GeV. The maximum cluster size is, therefore, limited to three towers in η ($\Delta\eta = 0.3$) and to one tower in ϕ ($\Delta\phi = 15^\circ$) in the central region.

The clustering algorithm requires a ratio of the HAD energy E^{HAD} to the EM energy E^{EM} in the EM cluster, HAD/EM, to be less than 0.125 because the EM calorimeters in the CDF detector can contain most of an EM shower. Only the EM energy of the EM cluster is treated as the cluster energy, but the HAD energy is not taken into account for the cluster energy. After finding CES strip clusters matching an EM cluster, which is described in the next section, the transverse energy of the EM cluster, E_T , are defined as

$$E_T = \frac{R_{\text{CES}}}{\sqrt{R_{\text{CES}}^2 + (Z_{\text{CES}} - Z_{\text{Vertex}})^2}} \cdot E, \quad (3.1)$$

where R_{CES} is the perpendicular distance from the beam line to the CES, Z_{CES} is the Z position of the CES strip cluster with the highest energy, Z_{Vertex} is the event vertex position determined by the VTPC, and E is the EM cluster energy.

3.2.2 CES Cluster Finding

The lateral shower profiles projected onto the wire view and onto the strip view are observed with the CES placed near the shower maximum in the CEM. The CES clusters are found independently in the wire view and in the strip view. The clustering starts from a list of seed channels with energy greater than 0.5 GeV, ordered in decreasing energy, and includes 11 channels centered on the seed channel. The CES clusters (wire clusters and strip clusters) must match with corresponding EM clusters.

If we know the standard shower profile of photons very well, the shower profile observed with the CES is useful for the separation of photons from the background dominated by neutral mesons decaying into photons. Unfortunately owing to lack of a photon test beam to learn the standard shower profile of photons, we must depend on that of electrons. Quantitative arguments on the estimation of the systematic uncertainty originating from using the shower profile of electrons instead of photons are discussed in the next chapter.

The standard shower profile in the wire view to be fitted to individual CES clusters,

f_{Wire} , is independent of the X position (a local coordinate in the direction perpendicular to wires) of the shower center and is symmetric about the shower center. Unlike the wire profile f_{Wire} , the strip profile f_{Strip} depends on the Z position of the shower center and is not symmetric about the shower center.

The Z dependence of the strip profile comes from the geometry of the CES. When a photon or an electron comes into the CEM at a polar angle θ , the EM shower is widened in the CES by a factor of $1/\sin \theta$. This widening can be removed by a change of the Z coordinate as $Z \rightarrow Z' = Z \sin \theta$. The asymmetry of the strip profile has two sources. Secondary particles of an EM shower pass through more material when they go on the high $|Z|$ side of the shower center because of traveling at more leaning angles than the primary photon or electron. Thus the high $|Z|$ side of the shower will produce more secondary particles. In addition, these secondary electrons and positrons will have a longer path in the CES and will produce proportionally more ionization. These two effects makes the strip profile asymmetric about the shower center.

In general, the strip profile can be decomposed into a symmetric profile,

$$f_{\text{Strip}}^{(\text{S})}(z') = \frac{1}{2} \{f_{\text{Strip}}(z') + f_{\text{Strip}}(-z')\} \quad (3.2)$$

and antisymmetric profile,

$$f_{\text{Strip}}^{(\text{A})}(z') = \frac{1}{2} \{f_{\text{Strip}}(z') - f_{\text{Strip}}(-z')\} \quad (3.3)$$

where z' is a position from the shower center in the Z' coordinate. The strip profile can be made up of the symmetric and antisymmetric standard shower profiles, $f_{\text{Strip}}^{(\text{S})}$ and $f_{\text{Strip}}^{(\text{A})}$, as

$$f_{\text{Strip}}(z') = f_{\text{Strip}}^{(\text{S})}(z') + f_{\text{Strip}}^{(\text{A})}(z') \cot \theta. \quad (3.4)$$

The wire and strip shower profiles, f_{Wire} and f_{Strip} , are normalized to unity. The integrals, from $-\infty$ to z' , of symmetric profiles in X and Z' are parameterized as shown below:

$$\begin{aligned} I_{\text{Wire}}(x) &= \int_{-\infty}^x f_{\text{Wire}}(x) dx \\ &= \frac{0.5}{1 + g_X} \left\{ \exp \left[-\frac{|x|}{b_{1X}} \left(1 + q_{1X} \frac{|x|}{b_{1X}} \right) \right] + g_X \exp \left[-\frac{|x|}{b_{2X}} \left(1 + q_{2X} \frac{|x|}{b_{2X}} \right) \right] \right\} \end{aligned} \quad (3.5)$$

$$\begin{aligned}
I_{\text{Strip}}^{(S)}(z') &= \int_{-\infty}^{z'} f_{\text{Strip}}^{(S)}(z') dz' \\
&= \frac{0.5}{1 + g_Z} \left\{ \exp \left[-\frac{|z'|}{b_{1Z}} \left(1 + q_{1Z} \frac{|z'|}{b_{1Z}} \right) \right] + g_Z \exp \left[-\frac{|z'|}{b_{2Z}} \left(1 + q_{2Z} \frac{|z'|}{b_{2Z}} \right) \right] \right\}
\end{aligned} \tag{3.6}$$

The energy dependence of parameters is fairly flat. The values of parameters in the symmetric standard shower profiles used for fitting to the data are shown in Table 3.1. The integral, from $-\infty$ to z' , of the antisymmetric profile can be parameterized as

$$I_{\text{Strip}}^{(A)}(z') = \int_{-\infty}^{z'} f_{\text{Strip}}^{(A)}(z') dz' \tag{3.7}$$

$$= (a + b|z'|) \exp \left[-\frac{|z'|}{b_3} \right]. \tag{3.8}$$

The energy dependence of the parameters a , b , and b_3 , is also flat. In reality, the Equation (3.8) is only approximative and requires a correction factor

$$C = 1 + 0.35 \exp \left[-\frac{|z'|}{5 \text{ cm}} \right] \tag{3.9}$$

to better fit to the data within 5 cm from the shower center. With this, the parameters are determined:

$$a = -0.026,$$

$$b = -0.022 \text{ cm}^{-1}, \text{ and}$$

$$b_3 = 1.60 \text{ cm}.$$

The standard shower profile, f_{Wire} , $f_{\text{Strip}}^{(S)}$, and $f_{\text{Strip}}^{(A)}$, and the integrated profile, I_{Wire} , $I_{\text{Strip}}^{(S)}$, and $I_{\text{Strip}}^{(A)}$ are numerically displayed in Figure 3.1.

The standard shower profile obtained from the test beam electrons is fitted to CES clusters by the least χ^2 method. The energy (E_{Wire} and E_{Strip}) and position (X_{Wire} and

	g	b_1 [cm]	b_2 [cm]	q_1	q_2
X (Wire)	0.311	0.472	2.065	-0.031	-0.044
Z (Strip)	0.269	0.583	2.182	-0.031	-0.044

Table 3.1: Parameters in the CES standard integral profiles I_{Wire} and $I_{\text{Strip}}^{(S)}$ are shown.

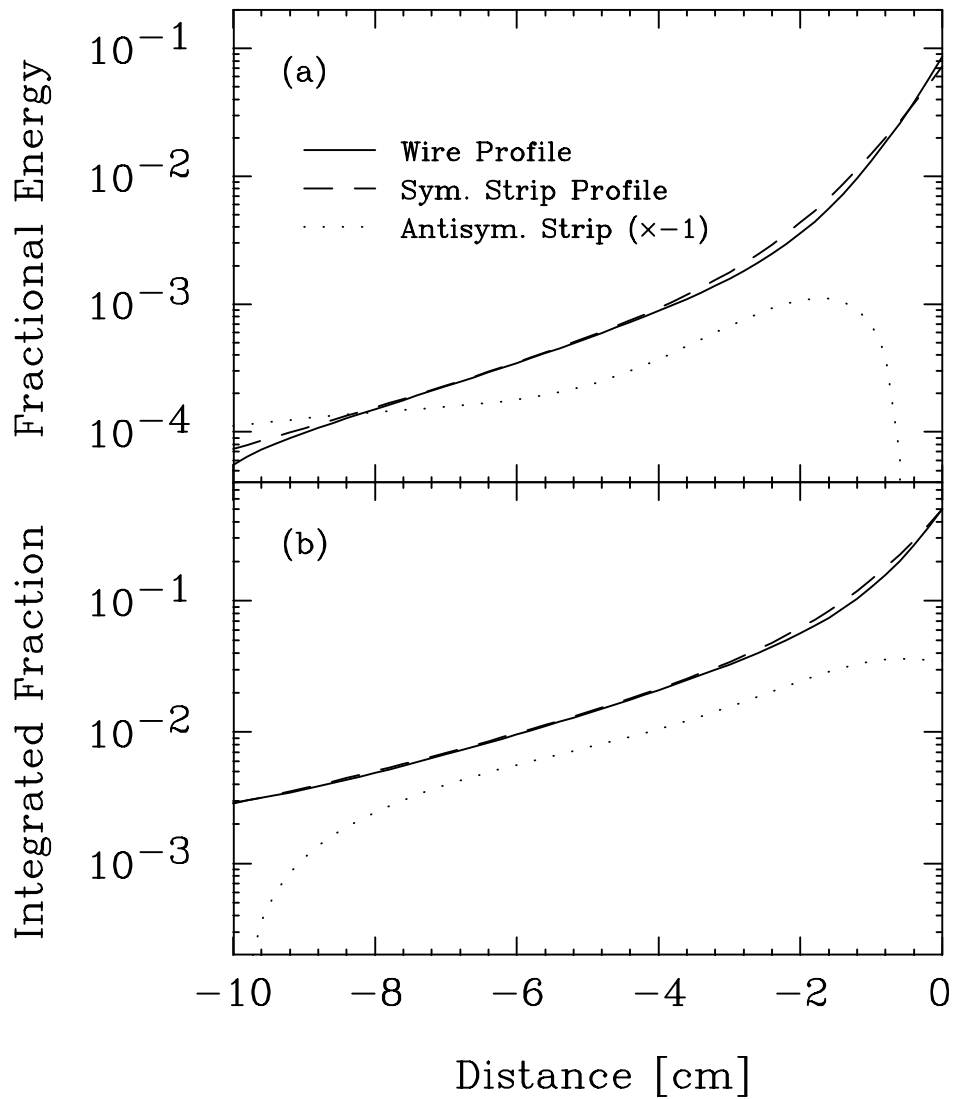


Figure 3.1: The lateral shower profiles and the integrals in the CES are shown: (a) f_{Wire} , $f_{\text{Strip}}^{(S)}$, and $f_{\text{Strip}}^{(A)}$, (b) I_{Wire} , $I_{\text{Strip}}^{(S)}$, and $I_{\text{Strip}}^{(A)}$.

Z_{Strip}) are free parameters in calculating χ^2 . The final χ^2 is calculated separately for the strip and wire clusters as:

$$\chi^2 = \frac{1}{4} \sum_{i=1}^{11} \frac{(y_i - \bar{y}_i)^2}{\sigma_i^2} \quad (3.10)$$

where i is the CES channel index, and y_i is the measured profile (either strip or wire) normalized to unity, \bar{y}_i is the standard profile, and σ_i^2 is the estimated variance of the standard profile \bar{y}_i . The standard profile \bar{y}_i to calculate the final χ^2 is defined as

$$\bar{y}_i = \int_{x_i^{\text{lower}}}^{x_i^{\text{upper}}} f(x) dx = I(x_i^{\text{upper}}) - I(x_i^{\text{lower}}) \quad (3.11)$$

where $f(x)$ is the standard shower profile $f_{\text{Wire}}(x)$ or $f_{\text{Strip}}(z')$, and $I(x)$ is the integrated profile $I_{\text{Wire}}(x)$ or $I_{\text{Strip}}(z')$. The standard shower profile f is integrated over the width of the i -th channel, from x_i^{lower} to x_i^{upper} , for \bar{y}_i .

The variance σ_i^2 depends on number of secondary electrons and positrons passing through the CES. In a naive model the number of secondary particles is proportional to the primary photon or electron energy. Therefore, the variance in the fractional number of secondary particles in each channel of a CES cluster is inversely proportional to the energy of the incident photon or electron, if the number of secondary particles fluctuates according to the Poisson distribution. More realistically, the position of the shower maximum has a logarithmic dependence on the primary energy, causing the fractional number of secondary particles in each channel of the CES cluster to have an additional weak dependence on the energy. The following energy scaling to form the variance is used:

$$\sigma_i^2(E) = \sigma_i^2(10 \text{ GeV}) \left(\frac{10 \text{ GeV}}{E} \right)^{0.747} \quad (3.12)$$

where

$$\sigma_i^2(10 \text{ GeV}) = (0.026)^2 + (0.096)^2 \cdot \bar{y}_i \quad (3.13)$$

is the variance for i -th channel in the standard profile determined from the 10-GeV electron test beam. The power 0.747 in Equation (3.12) is determined from the CES response measured in the test beam data.

The χ^2 distributions of electrons from W decays are shown in Figure 3.2 together with those from the QFL simulation which is a detector simulation for the CDF detector. The

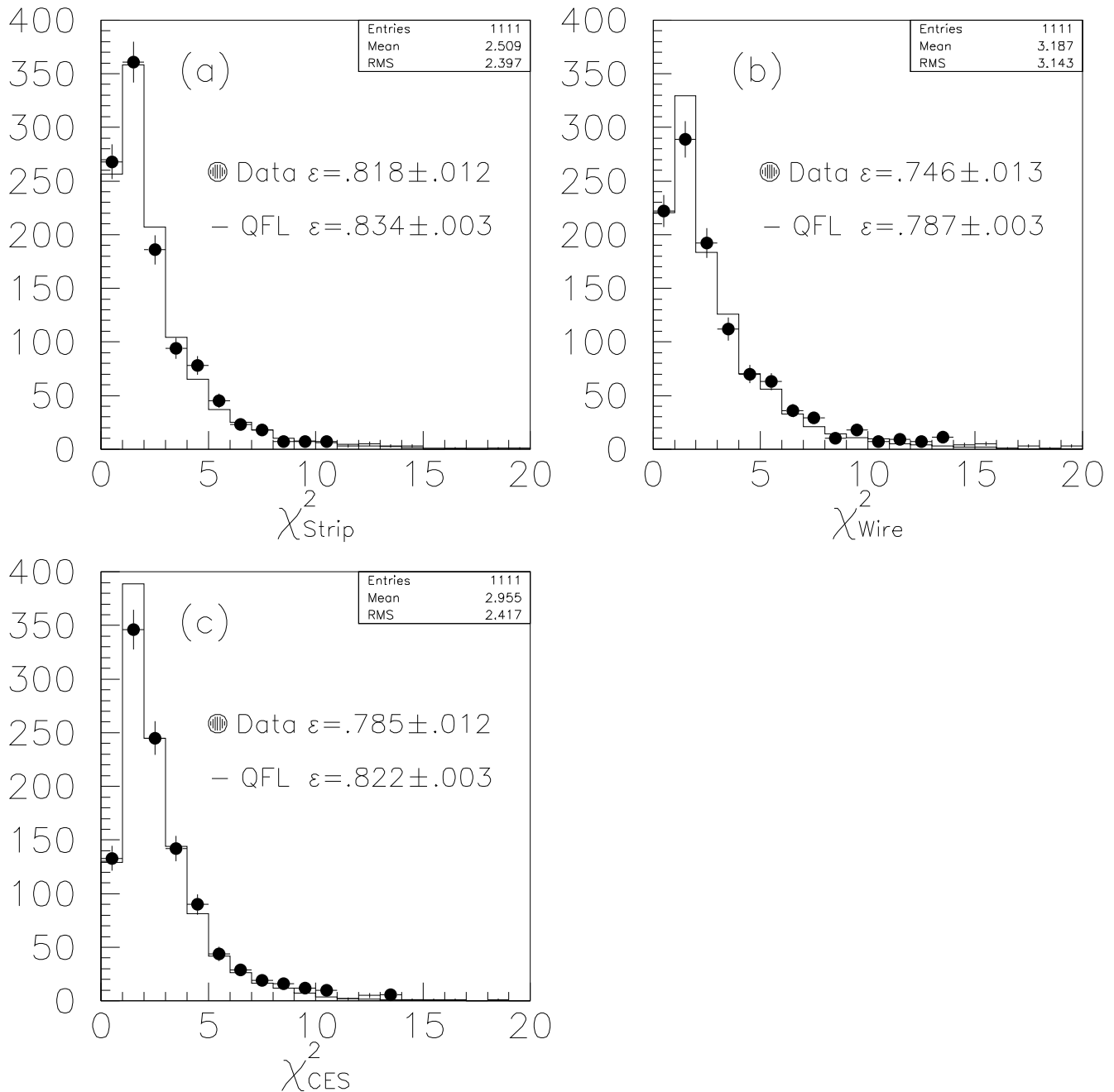
CES χ^2 for W Electrons From Data and QFL

Figure 3.2: The χ^2 's of electrons from W decays in the data (points) and QFL simulation (solid line) are shown: (a) χ^2_{Strip} , (b) χ^2_{Wire} , and (c) $\chi^2_{\text{CES}} = \frac{1}{2}(\chi^2_{\text{Strip}} + \chi^2_{\text{Wire}})$. The efficiencies of χ^2 cut at 4 are also shown.

simulation includes the affects of internal and external radiation, and the actual underlying event in W events. The efficiencies of the χ^2 cut at 4 are also shown in Figure 3.2. This indicates that the choice of the standard shower profile and the variance is reasonably good.

3.2.3 Lateral Tower Sharing Algorithm (LSHR)

An EM cluster in the central region is limited within three towers because an EM shower is contained at the most in three towers, even if the event vertex position is far from the nominal interaction point. LSHR is formulated from the three-tower sharing characteristic obtained from the electron test beam. The definition is

$$\text{LSHR} = 0.14 \sum_k \frac{M_k - P_k}{\sqrt{(0.14\sqrt{E})^2 + (\Delta P_k)^2}} \quad (3.14)$$

where the sum is over two towers adjacent to the seed tower. M_k is the measured energy in the adjacent tower. P_k is the expected energy in the adjacent tower from the standard shower profile with the EM cluster energy E , the event vertex position, and the Z position Z_{CES} of the CES cluster in the EM cluster. ΔP_k is the uncertainty in P_k associated with a 1-cm variation in Z_{CES} . The term of $0.14\sqrt{E}$ is the uncertainty in the EM cluster energy due to the CEM energy resolution.

3.2.4 Isolation

The isolation is a quantity which is effective to select prompt photons against the background. The dominant backgrounds to the prompt photons are neutral mesons such as π^0 , η , and K_S^0 dissociated from jets produced by QCD processes. Hence the backgrounds are not isolated. Thus, the isolation is required for both photons in the selection criteria for diphoton events. The border isolation I_{Border} is defined as a ratio of the sum of E_T deposited in the surrounding towers around an EM cluster to E_T of the EM cluster.

To look into the isolation distribution of photons in the data, the final selection criteria for photon candidates, listed in Table 5.1, are applied to both EM clusters except for the isolation cut, and only either photon candidate is required to pass the isolation cut. In Figure 3.3,

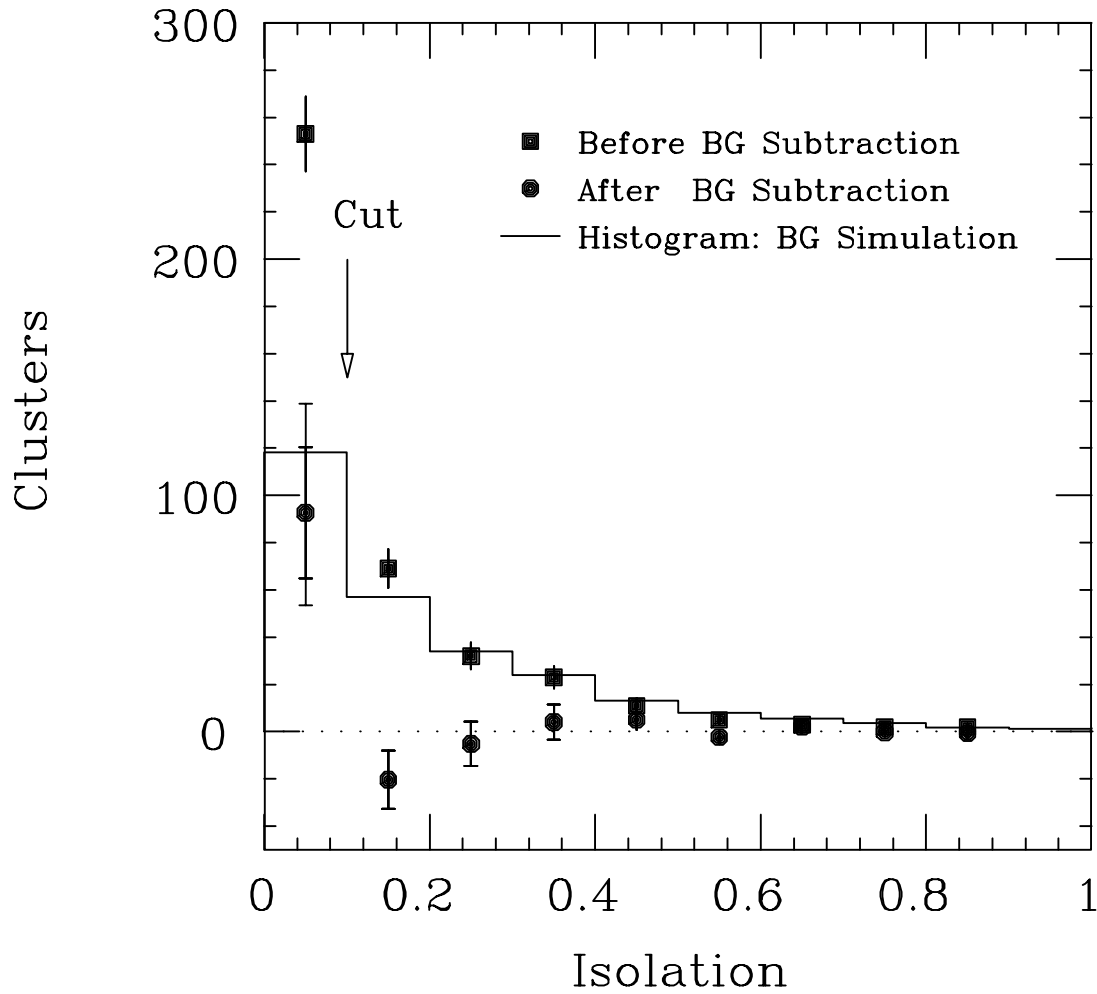


Figure 3.3: The isolation distributions for photon candidates in the diphoton data before (squares) and after (circles) the photon identification are shown. The isolation distribution for the QCD backgrounds simulated by PYTHIA and QFL (solid line) is also shown.

squares show the isolation distribution of photon candidates to which the isolation cut is not applied. The photon candidates include true photons and the background. We can subtract the background by using the photon identification method described in Chapter 5. Circles show the isolation distribution of true photons to which the isolation cut is not applied.

To study the isolation distribution for the backgrounds, the single prompt photon events are generated by a Monte Carlo event generator PYTHIA 5.4 [47, 48, 49], and those events which include a high- p_T neutral meson in the away-side jet are selected. Furthermore, responses of the CDF detector to these events are simulated with the QFL simulation. The same event selection criteria as the diphoton data are applied to the simulation data. The isolation distribution for the QCD backgrounds simulated by PYTHIA and QFL is presented by a solid line in Figure 3.3.

A significance of this distribution is that the data before the background subtraction (squares) show a large number of excess events above the QCD background (solid line) in the first bin. This is expected because prompt photons are better isolated than neutral mesons dissociated from jets. The diphoton contribution to the isolation distribution makes up this difference, and that is found only in the first bin. The isolation cut at 0.1 practically retains all photons, while eliminating a large portion of the QCD background.

3.2.5 Selection Criteria for Diphoton Events

For the diphoton data set, events which include two or more EM clusters with $E_T > 10$ GeV in the central region are selected. The EM clusters are required to satisfy the following:

- Each EM cluster is associated with no track.
- HAD/EM is less than $ABW = 0.055 + 0.045 \times E[\text{GeV}]/100$.
- LSHR is less than 0.2.
- The border isolation I_{Border} is less than 0.1.

After these requirements, 834 events remain in the diphoton data set.

3.3 Missing E_T in the Diphoton Events

Diphoton events like ordinary QCD events are expected to have no high- p_T neutrinos nor high- p_T muons whose energy the calorimeter can not directly measure. Hence the missing transverse energy \cancel{E}_T , which is the vector sum of total E_T over all towers, in the diphoton event should be centered around zero. We define the missing E_T significance as

$$S = \frac{\cancel{E}_T}{\sqrt{\Sigma E_T}}, \quad (3.15)$$

where ΣE_T is the scalar sum of total E_T over all towers. S_X and S_Y denote projection of S onto X and Y axes, respectively. Distributions of S_X and S_Y in the diphoton data selected by the criteria for diphoton events except for the isolation cut are shown in Figure 3.4 (a) and (b), respectively, together with Gaussian curves fitted to the data. The standard deviations of S_X and S_Y have the same value of $0.55 \pm 0.01 \text{ GeV}^{\frac{1}{2}}$. This value is consistent with that observed in the 1987 collider run, which was $0.6 \text{ GeV}^{\frac{1}{2}}$ [30]. As mentioned in Appendix B, the standard deviation is equivalent to an overall energy resolution divided by $\sqrt{2}$.

Slight offsets of S_X and S_Y is due to non-uniformity of the calorimeters, which is normally corrected in our analysis. The missing E_T significance S corrected for the offsets in S_X and S_Y is shown in Figure 3.4 (c). The S distribution is expected to be a bi-gaussian because the S_X and S_Y distributions are Gaussian as shown in Figure 3.4 (a) and (b). The bi-Gaussian fitted to the S distribution is also shown by a curve in Figure 3.4 (c). The fit parameter P_2 shown in Figure 3.4 (c) corresponds to the standard deviations in the S_X and S_Y distributions. The fitting is fairly good. Thus we can understand that the S distribution comes from the overall energy resolution of the calorimeters. Figure 3.4 (d) shows the missing E_T significance S in the final diphoton data described in Chapter 5 together with the bi-Gaussian fitted to the data, where S is corrected by the same way as Figure 3.4 (c). The S distribution in the final diphoton data is also consistent with the bi-Gaussian. The final diphoton data show no deviation from the expected QCD events.

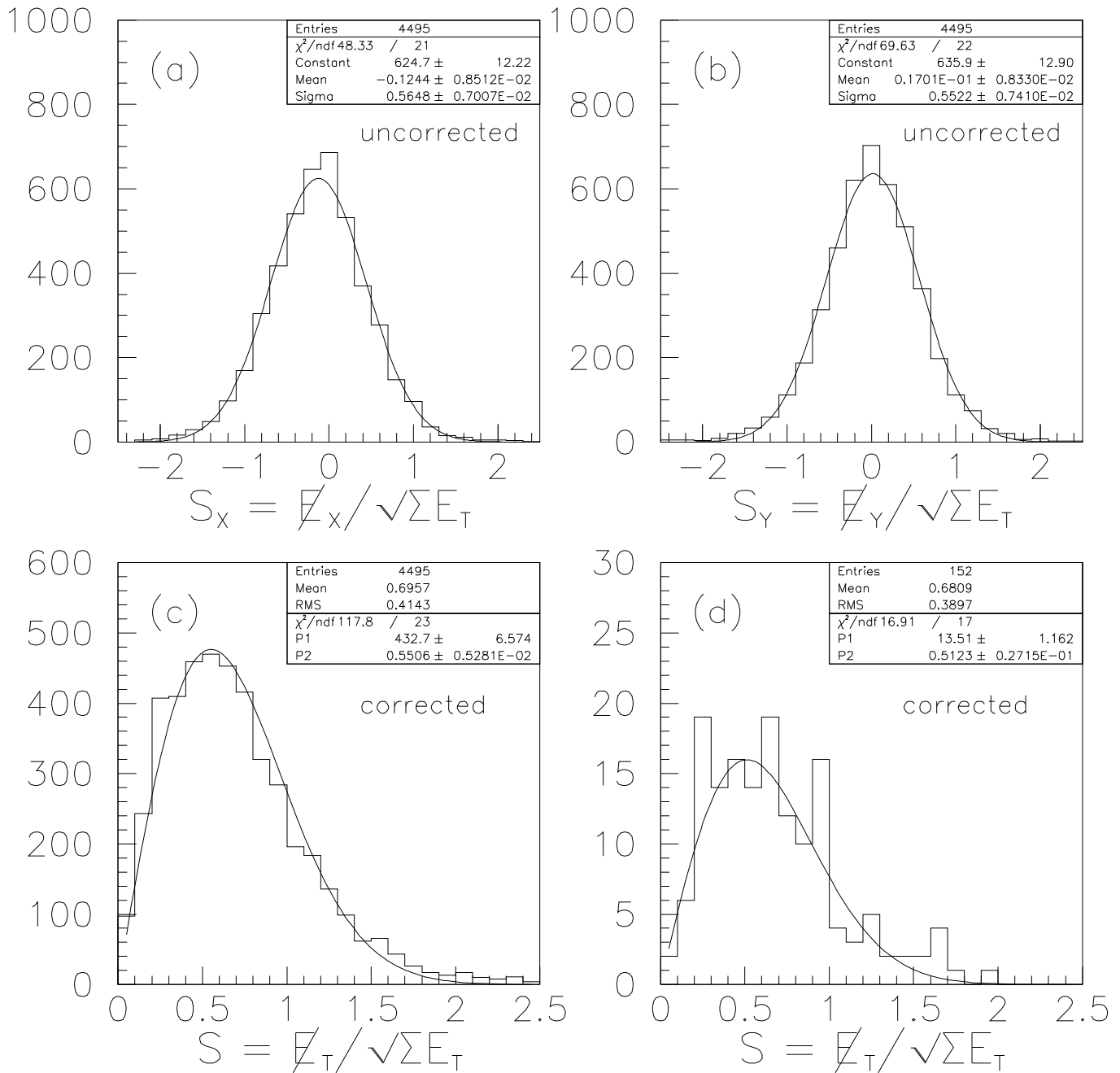


Figure 3.4: (a) The uncorrected S_X and (b) the uncorrected S_Y in the diphoton data are shown together with the Gaussians fitted to the data. (c) The corrected S is shown together with the bi-Gaussian fitted to the data. (d) The corrected S in the final diphoton data and the bi-Gaussian fitted to the data are shown.

3.4 Study of Event Selection Efficiency

To estimate efficiencies of cuts for the event selection, we use two samples which include electrons in the central region. One of them is the sample of Drell-Yan events ($q\bar{q} \rightarrow e^+e^-$), and the other is the sample of W events ($W \rightarrow e\nu$).

Events in the Drell-Yan sample are triggered by the dielectron trigger. This trigger requires two or more level-2 EM clusters with $E_T > 5$ GeV in the central region, each of which is associated with a level-2 track with $p_T > 4.8$ GeV/ c . One electron candidate in each event is required to satisfy tight selection criteria, while loose selection criteria are applied to the other electron candidate. These selection criteria for electron candidates are summarized in Table 3.2. Positions of a track (Z_{CTC} and X_{CTC}), observed by the CTC and extrapolated to the CES, are required to agree with positions determined by the CES (Z_{CES} and X_{CES}). VTCAND is a ratio of the number of hits for a track in the VTPC to the number of channels measuring the track. N_{Track} is the number of tracks observed by the CTC which are associated with an EM cluster. E/p is a ratio of E_T of an EM cluster to p_T of a track associated with the EM cluster. E/p of an electron should be around unity. The fiducial cuts reject an EM cluster when the shower center position determined by the CES is within either area listed below:

- $|X_{\text{CES}}| > 21$ cm.
- $|Z_{\text{CES}}| < 9$ cm.

In addition, the fiducial cuts reject a central EM cluster when the seed tower is within any area listed below:

- tower 9 ($1.0 < |\eta| < 1.1$).
- tower 7 of the chimney module.

The chimney module contains a region in which the cryogenic dewar for the superconducting solenoid coil is located.

CEM cluster selection	
Tight cuts	Loose cuts
$N_{\text{Track}} = 1$	$N_{\text{Track}} = 1$
Fiducial cuts	Fiducial cuts
$ Z_{\text{CTC}} - Z_{\text{CES}} < 3.0 \text{ cm}$	$ Z_{\text{CTC}} - Z_{\text{CES}} < 3.0 \text{ cm}$
$ X_{\text{CTC}} - X_{\text{CES}} < 1.5 \text{ cm}$	$ X_{\text{CTC}} - X_{\text{CES}} < 1.5 \text{ cm}$
$E/p < 1.5$	$E/p < 1.5$
$\chi_{\text{Strip}}^2 < 15$	
VTCAND > 0.2	
HAD/EM < ABW	
LSHR < 0.2	

Table 3.2: Cuts for the Drell-Yan sample, which is used for estimating efficiencies of the level-2 trigger, HAD/EM cut, and LSHR cut, are summarized.

Every event in the $W \rightarrow e\nu$ sample is required to contain one electron with large transverse energy in the central region. Selection criteria of an electron candidate for the $W \rightarrow e\nu$ sample are listed below:

- $E_T > 25 \text{ GeV}$.
- CEM fiducial cuts.
- $\Delta\phi > 1.5^\circ$ from wedge ϕ boundary.
- $|Z_{\text{CTC}} - Z_{\text{CES}}| < 3.0 \text{ cm}$.
- $|X_{\text{CTC}} - X_{\text{CES}}| < 1.5 \text{ cm}$.
- HAD/EM < 0.10.
- LSHR < 0.2.
- $E/p < 1.5$ if $p_T > 20 \text{ GeV}/c$.

In addition, each event is required to satisfy the following cuts:

- $E_T > 25$ GeV.
- $|Z_{\text{Vertex}}| < 60$ cm.

Each event are required to have large missing transverse energy for an evidence of a neutrino from a W decay. When the Z position of the event vertex is far away from the center of the CDF detector, a gap with no calorimetry appears between the plug and forward calorimeters. Thus the Z position of the event vertex, Z_{Vertex} , must be around the nominal interaction point.

The Drell-Yan sample is used for studying efficiencies of the level-2 trigger, the HAD/EM cut, and the LSHR cut. The W electron sample is used to estimating the efficiency of the isolation cut.

3.4.1 Level-2 Trigger Efficiency

The tower sizes, the thresholds for seed towers, the tower thresholds, and the limit of number of towers for clustering are different between the level-2 trigger process and the offline DST¹ production as summarized in Table 3.3. Furthermore, in the offline DST production, the transverse energy is calculated with respect to the event vertex, while in the level-2 trigger process the transverse energy is calculated with respect to the nominal interaction point, that is, the origin of the CDF coordinate system. These differences give rise to inefficiency of the level-2 trigger for photons and electrons with $E_T > 10$ GeV.

Electron candidates in the Drell-Yan sample is used to study the correlation between transverse energies of a level-2 EM cluster and an offline one, E_T^{Level2} and E_T , in the central region. Events in the Drell-Yan sample are triggered by a dielectron trigger which requires two or more level-2 EM clusters with $E_T > 5$ GeV to be associated with a level-2 track having $p_T > 4.8$ GeV/ c . Electron candidates are selected by the following cuts:

- $E_T > 5$ GeV

¹Data Summary Tape

	Threshold [GeV]		Tower size	Towers	HAD/EM
	Seed	Shoulder	$(\Delta\eta \times \Delta\phi)$	$(\eta \times \phi)$	
Level 2	4.0	3.6	$0.2 \times 15^\circ$	15×1	0.125
Offline	3.0	0.1	$0.1 \times 15^\circ$	3×1	0.125

Table 3.3: Thresholds for finding EM clusters in the level-2 trigger and those for the offline DST production are summarized.

- $N_{\text{Track}} = 1$
- $\text{HAD/EM} < \text{ABW}$
- $\text{LSHR} < 0.2$
- $|Z_{\text{CTC}} - Z_{\text{CES}}| < 3.0 \text{ cm}$
- $|X_{\text{CTC}} - X_{\text{CES}}| < 1.5 \text{ cm}$
- $E/p < 1.5$

The level-2 trigger efficiency is probability that a level-2 EM cluster corresponding to an offline EM cluster is over the trigger threshold of $E_{\text{T}}^{\text{Level2}} = 10 \text{ GeV}$. This is evaluated from the correlation between $E_{\text{T}}^{\text{Level2}}$ and E_{T} of electrons in the Drell-Yan sample. Figure 3.5 shows the trigger efficiency ϵ_{L2T} as a function of E_{T} of an EM cluster. The error bars are statistical uncertainties. This uncertainty in the level-2 trigger efficiency gives rise to the systematic uncertainty in the cross section for diphoton production. The level-2 trigger is fully efficient for photons and electrons with $E_{\text{T}} > 13 \text{ GeV}$ as shown in Figure 3.5.

3.4.2 HAD/EM Cut Efficiency

The HAD/EM cut at 0.125 applied at the clustering stage is actually loose and can be tightened for photons and electrons. The tight cut value defined by $\text{ABW} = 0.055 + 0.045 \times E[\text{GeV}]/100$ is used to reduce the background further.

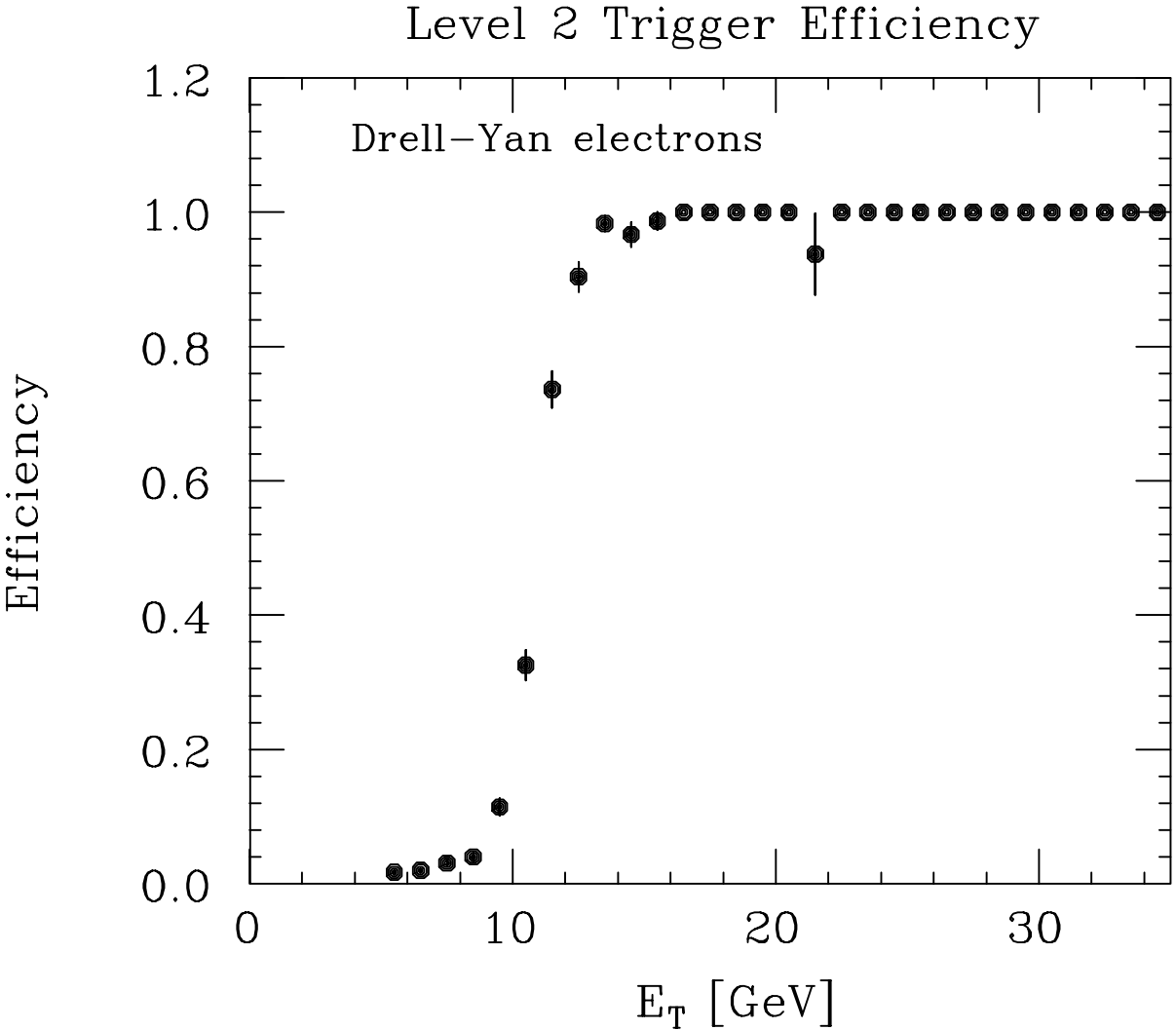


Figure 3.5: The level-2 trigger efficiency is presented. The efficiency is evaluated by using electrons in the Drell-Yan sample.

For validity of the HAD/EM cut at ABW, electron candidates in the Drell-Yan sample are used. Events are required for two or more electron candidates in the central region to pass the following cuts:

- $E_T > 5$ GeV.
- Tight CEM cuts for the Drell-Yan sample except for the HAD/EM cut.
- $I(R = 0.4) < 0.1$.

$I(R = 0.4)$ is cone isolation which is defined as

$$I(R = 0.4) = \frac{E_T^{\text{Cone}} - E_T}{E_T} \quad (3.16)$$

where E_T^{Cone} is the transverse energy in a cone centered on the EM cluster, and E_T is the transverse energy of the EM cluster. The cone includes all towers within a radius $R = \sqrt{\Delta\eta^2 + \Delta\phi^2} = 0.4$ where $\Delta\eta$ and $\Delta\phi$ (in radian) are differences between a tower center position and the EM cluster position in η and in ϕ , respectively.

Each event in this Drell-Yan sample must obviously contain at least one electron candidate passing the tight HAD/EM cut at ABW but another electron candidate to which the tight HAD/EM cut is not applied. Figure 3.6 shows HAD/EM – ABW for electron candidates to which are not applied the tight HAD/EM cut in this Drell-Yan sample. Four of 518 electron candidates fail the tight HAD/EM cut at ABW. The efficiency is $99.2 \pm 0.4\%$ for electron candidates with $E_T > 5$ GeV, where the error is the statistical uncertainty. For high- E_T electrons, we have the $W \rightarrow e\nu$ data collected by the \cancel{E}_T selection which is independent of the tight HAD/EM cut for electrons. For electrons in the $W \rightarrow e\nu$ data, the efficiency of the HAD/EM cut at ABW is 0.99 ± 0.01 [32]. This is comparable with the HAD/EM cut efficiency for low- p_T electrons in the Drell-Yan sample. Thus the HAD/EM cut at ABW is fully efficient for photons and electrons with approximately $5 < E_T < 40$ GeV.

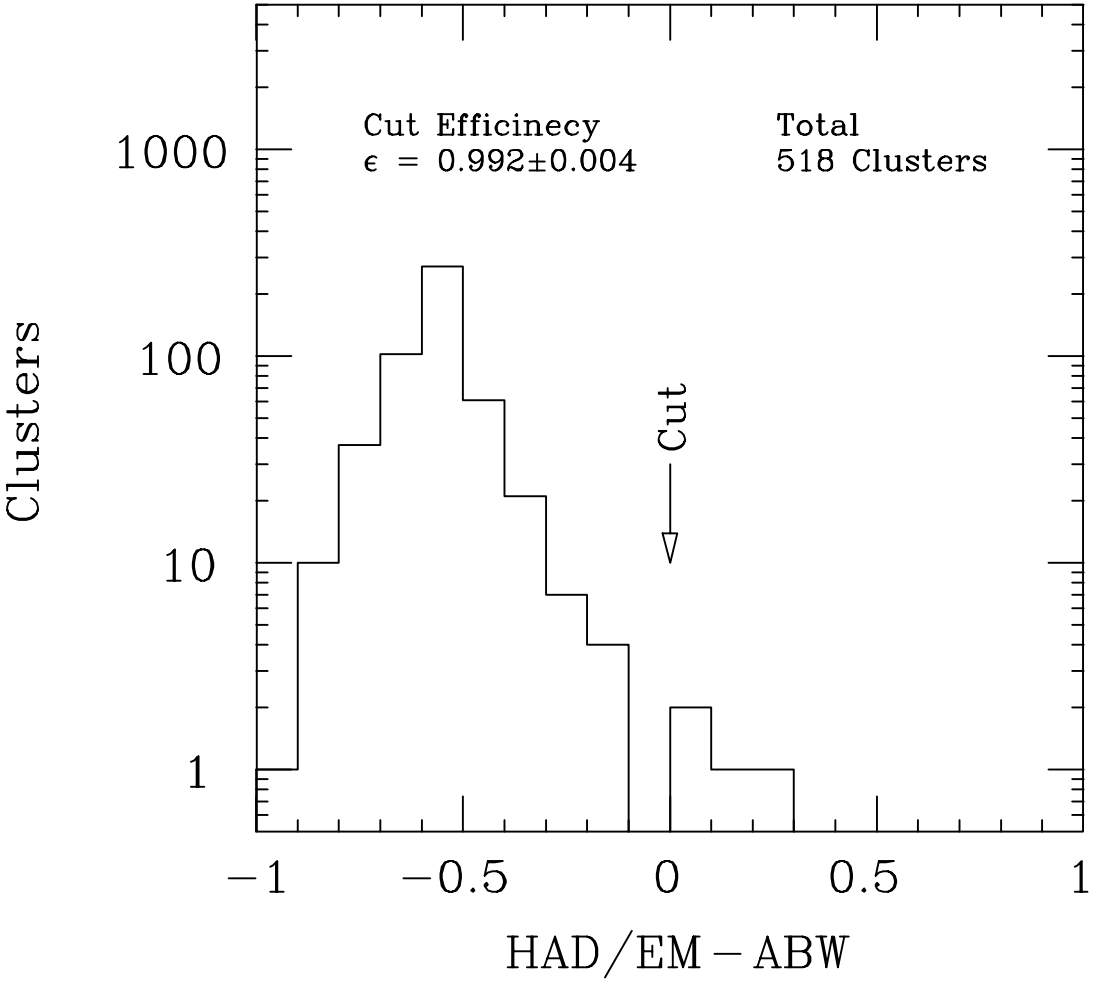


Figure 3.6: The $HAD/EM - ABW$ distribution for electrons in the Drell-Yan sample is shown. The efficiency of the HAD/EM cut at ABW for electrons is also presented.

3.4.3 LSHR Cut Efficiency

The LSHR cut at 0.2 is applied to EM clusters in the diphoton event selection, but the cut is loose for photons and electrons. To estimate the LSHR cut efficiency, electron candidates in the Drell-Yan sample are used. Events are required for two or more electron candidates in the central region to pass the following cuts:

- $E_T > 5$ GeV.
- Tight CEM cuts for the Drell-Yan sample except for the LSHR cut.
- $I(R = 0.4) < 0.1$.

Each event in this Drell-Yan sample must obviously contain at least one electron candidate passing the LSHR cut at 0.2 but another electron candidate to which no LSHR cut is applied. Figure 3.7 shows LSHR for electron candidates to which are applied no LSHR cut in this Drell-Yan sample. 11 of 525 electron candidates fail the LSHR cut at 0.2. The efficiency is $97.9 \pm 0.6\%$ for electron candidates with $E_T > 5$ GeV, where the error is the statistical uncertainty. For high- E_T electrons, we have the $W \rightarrow e\nu$ data collected by the \cancel{E}_T selection which is independent of the LSHR cut for electrons. For electrons in the $W \rightarrow e\nu$ data, the LSHR cut efficiency is 0.97 ± 0.01 [32]. This is comparable with the LSHR cut efficiency for low- E_T electrons in the Drell-Yan sample. Thus LSHR cut is fully efficient for photons and electrons with approximately $5 < E_T < 40$ GeV.

3.4.4 Isolation Cut Efficiency

As we have discussed in Section 3.2.4, the isolation is a useful quantity to reduce the background to prompt photons. However, even a prompt photon can be associated with background particles around itself. Such background activity is referred to as an underlying event.

To estimate the efficiency of the border isolation cut for photons in diphoton events, we study the underlying event in the $W \rightarrow e\nu$ sample in which no isolation cut is applied to

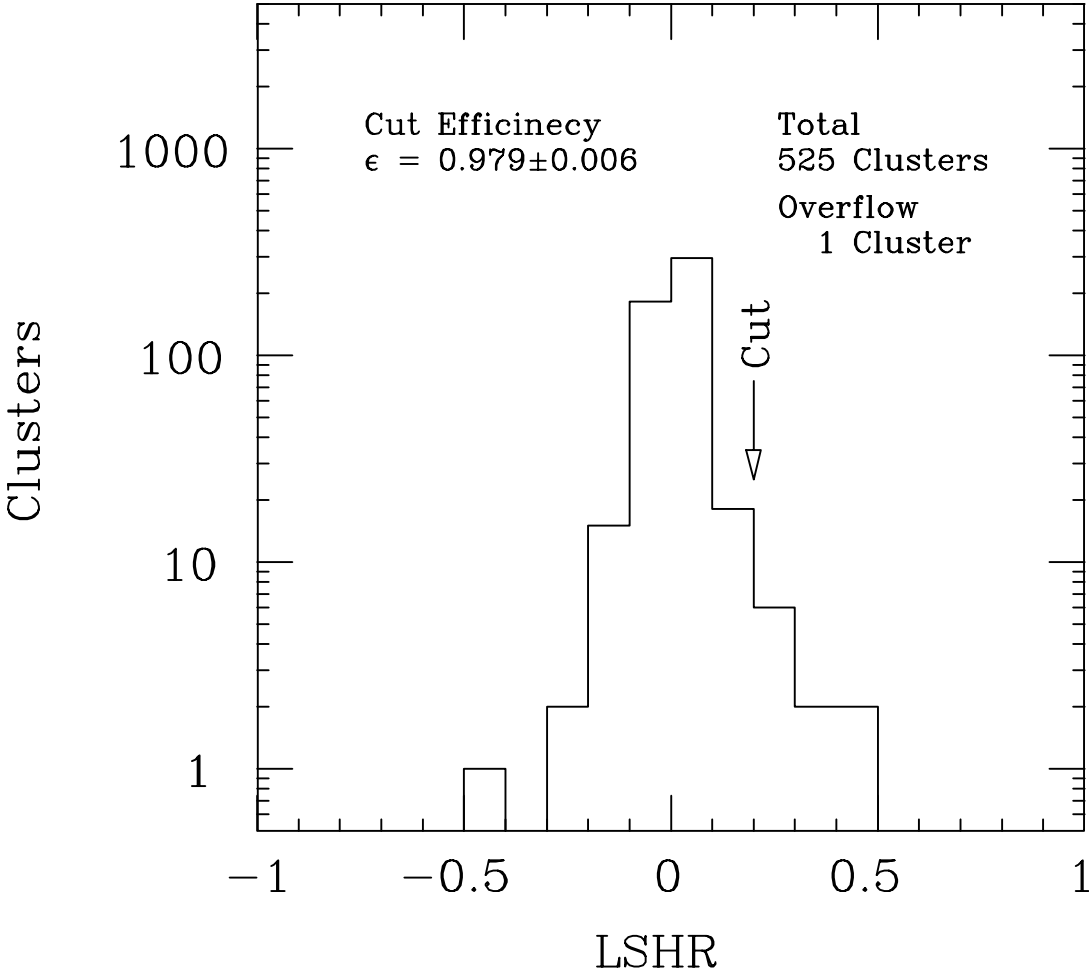


Figure 3.7: The LSHR distribution for electrons in the Drell-Yan sample is shown. The LSHR cut efficiency at 0.2 for electrons is also presented.

electrons. The border E_T around photons in diphoton events is shown by circles in Figure 3.8. Squares shows the border E_T around electrons in $W \rightarrow e\nu$ events. Both events are simulated by PYTHIA without the detector simulation. The border E_T for the simulation is defined as the sum of p_T of particles except for a photon or an electron within the window of $\Delta\eta \times \Delta\phi = 0.4 \times 30^\circ$ centered on the photon or the electron. The expectation by PYTHIA is that the border E_T in diphoton events is similar to that in W events. This justifies the use of the $W \rightarrow e\nu$ sample to study the isolation cut efficiency for photons in diphoton events. Detail discussion on the similarity between W and diphoton productions is made in Chapter 6.

The border E_T around electrons in the $W \rightarrow e\nu$ sample is shown in Figure 3.9 (b). When an electron has transverse energy of E_T , the efficiency of the border isolation cut at 0.1 for the electron is probability that the electron has the border E_T of $0.1 \times E_T$ around itself. The probability is estimated from Figure 3.9 (b). Thus we get the efficiency of the border isolation cut for photons in diphoton events, which is shown as a function of E_T of a photon in Figure 3.9 (a). The error bars are statistical uncertainties. Because the underlying event in W events instead of diphoton events is used to estimate the efficiency, the value of correction $\pm(1 - \epsilon_{\text{ISO}})$ is taken as the systematic uncertainty in the isolation cut efficiency.

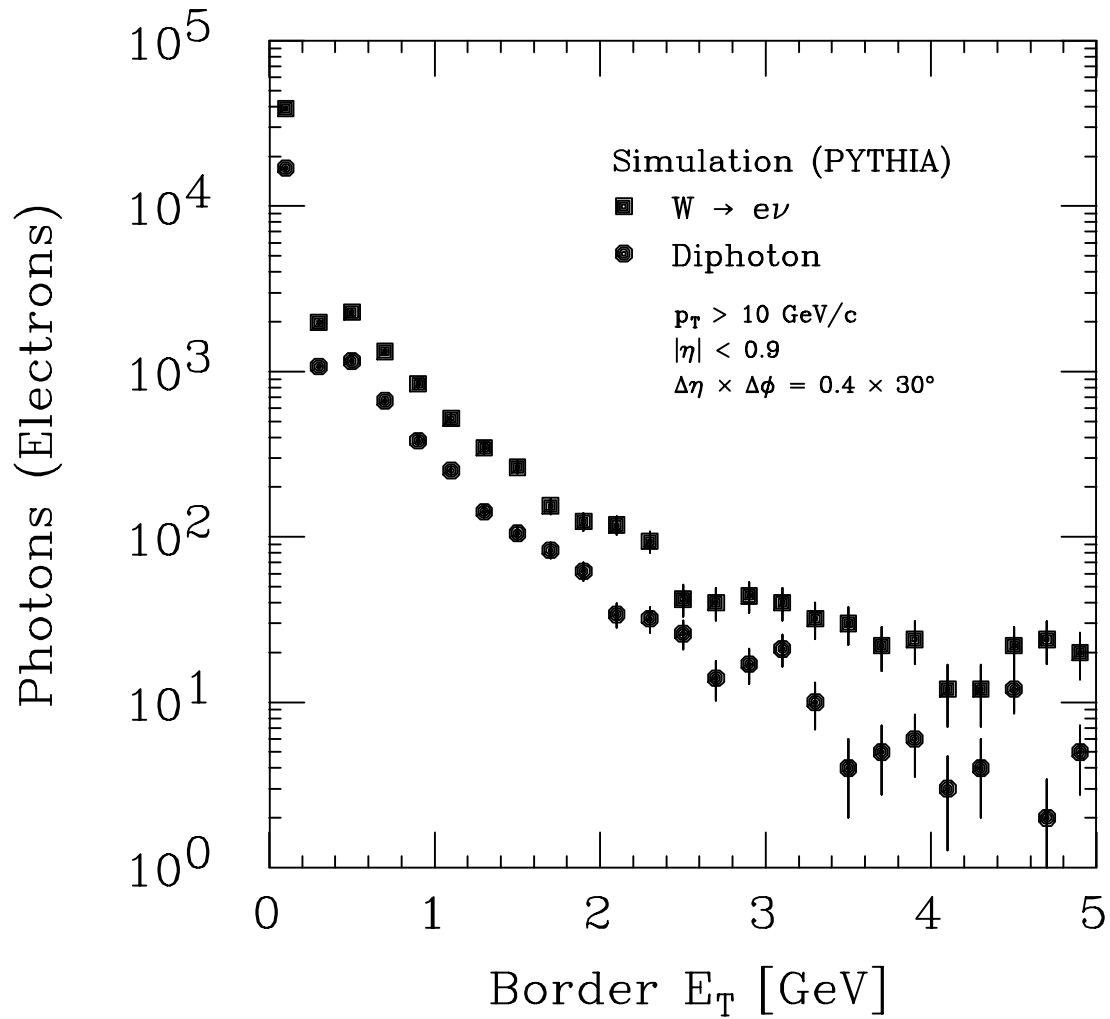


Figure 3.8: The border E_T for photons in diphoton events is shown by circles. Squares show the border E_T for W electrons. These events are simulated by PYTHIA without the detector simulation.

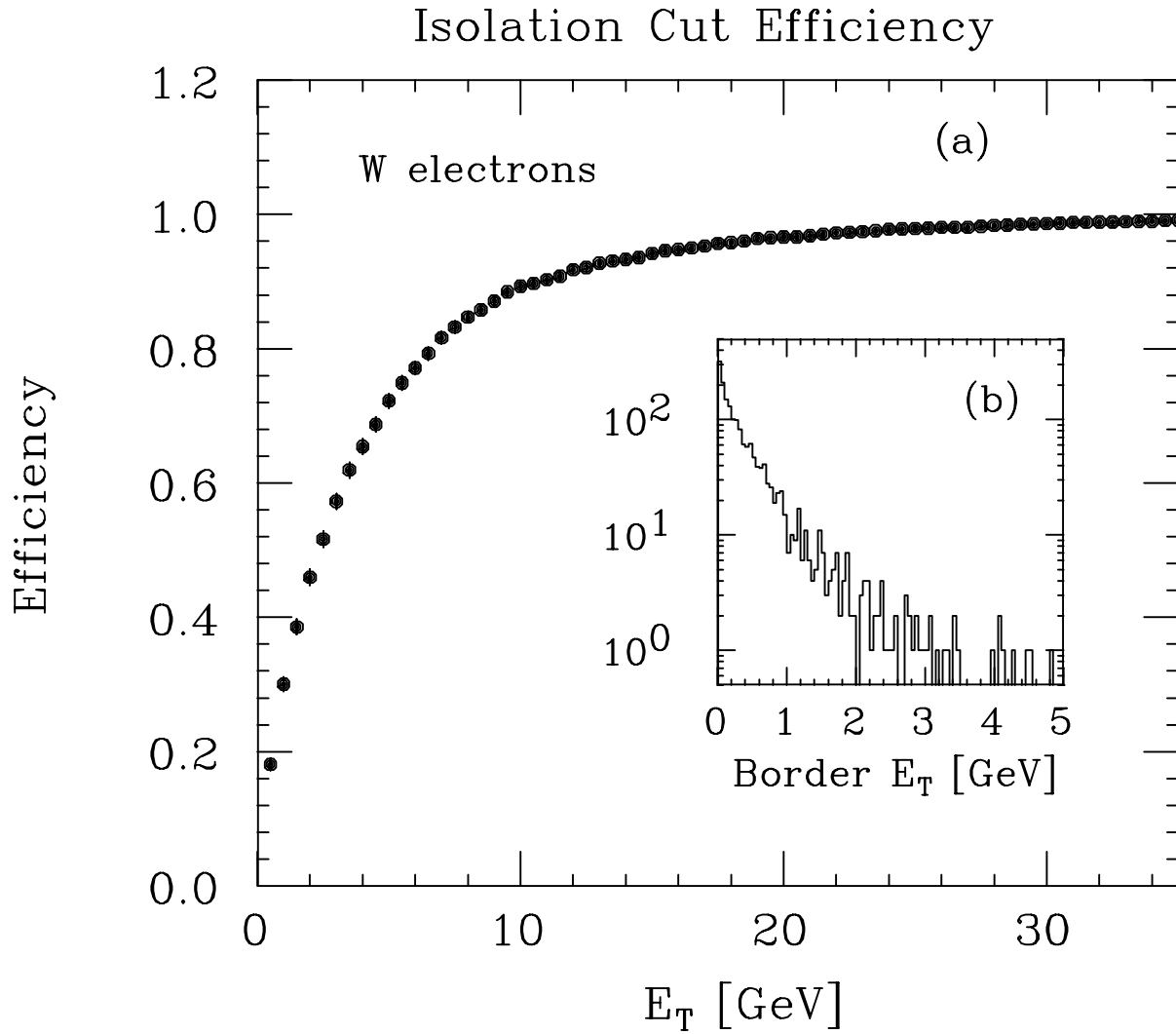


Figure 3.9: (a) The isolation cut efficiency at 0.1 for electrons in the W sample is shown. (b) The border E_T of electrons in the W sample is shown, which is used for estimating the isolation cut efficiency.

Chapter 4

Photon Identification

The dominant backgrounds to prompt photons are neutral mesons decaying into multiple photons, which are dissociated from jets. The event selection criteria, in particular the HAD/EM cut and the isolation cut, reduce these backgrounds, but single neutral mesons still remain in the diphoton data. Because two photons from a π^0 with $p_T = 10$ GeV/ c separate only by 5 cm in the CES, we do not always reconstruct π^0 's from two CES clusters. However, we can subtract the background from photon candidates statistically, because the EM shower profiles of multiple photons, which observed in the CES, differ from those of single photons. This photon identification can be applied to photon candidates with $p_T < 35$ GeV/ c as mentioned later.

In the central region, an additional leverage can be obtained from the CDT, which acts almost like a preshower counter. Photon identification by a preshower counter is superior as it is independent of photon momentum. In fact, a study showed that indeed the CDT was capable for identifying photons of higher momentum [24, 25]. Since there are few events in the range of $p_T > 35$ GeV/ c as shown in Figure 1.1, the CDT method, however, is not used in this analysis.

The plug EM calorimeter (PEM) contains the strip chamber near the shower maximum, which allows identification of photons by the same way as the CES method. Furthermore, the PEM has not only three longitudinal segments in each tower but also an anode readout for every layer. A measurement of the EM shower development in depth also allows identification

of photons. But photons in the plug region are not used in this analysis because the method of photon identification with the plug EM calorimeter is still under study.

In this chapter, the identification method for photons with the CES and the systematics are described.

4.1 Photon Identification Method

The CES provides lateral profiles of an EM shower projected onto the the Z axis in strips and onto the X axis in wires as described in Section 3.2.2. CES strip and wire clusters, which consist of 11 channels in each view, are found out in every EM cluster. A neutral meson, such as π^0 and η , with low p_T usually generate two separate CES clusters in an EM cluster, and can be rejected. Two photons from a neutral meson with high p_T are mostly observed as a single CES cluster. In this case, we use a statistical method to separate single photons from multiple photons. The standard shower profiles obtained from test beam electrons are fitted to the wire and strip clusters to get positions and energies of the CES clusters. Furthermore, χ_{Strip}^2 and χ_{Wire}^2 are obtained as a measure of goodness of fit. The average of χ^2 's for strip and wire clusters, $\chi_{\text{CES}}^2 = \frac{1}{2}(\chi_{\text{Strip}}^2 + \chi_{\text{Wire}}^2)$, is used for the photon identification.

We use the χ_{CES}^2 cut at $\chi_{\text{CES}}^2 = 4$ to separate photons from the background. Let N_F be the number of EM clusters which fail the χ_{CES}^2 cut in a sample of photon candidates, and let N_P be the number of EM clusters which pass the χ_{CES}^2 cut in the same sample. If we know the efficiency ϵ_{π^0} for neutral mesons to pass the χ_{CES}^2 cut and the efficiency ϵ_γ for single photons to pass the χ_{CES}^2 cut, we can express N_F and N_P from the efficiencies, ϵ_{π^0} and ϵ_γ , and the true numbers of neutral mesons and single photons, W_{π^0} and W_γ . The equation is written as

$$\begin{pmatrix} N_F \\ N_P \end{pmatrix} = \begin{pmatrix} 1 - \epsilon_{\pi^0} & 1 - \epsilon_\gamma \\ \epsilon_{\pi^0} & \epsilon_\gamma \end{pmatrix} \begin{pmatrix} W_{\pi^0} \\ W_\gamma \end{pmatrix}. \quad (4.1)$$

Inverting this equation, we get the true numbers of neutral mesons and photons as:

$$\begin{pmatrix} W_{\pi^0} \\ W_\gamma \end{pmatrix} = \frac{1}{\epsilon_\gamma - \epsilon_{\pi^0}} \begin{pmatrix} \epsilon_\gamma & \epsilon_\gamma - 1 \\ -\epsilon_{\pi^0} & 1 - \epsilon_{\pi^0} \end{pmatrix} \begin{pmatrix} N_F \\ N_P \end{pmatrix}. \quad (4.2)$$

Contributions of systematic uncertainty in ϵ_γ and ϵ_{π^0} to the true number of photons are as follows:

$$\frac{\partial W_\gamma}{\partial \epsilon_\gamma} = -\frac{W_\gamma}{\epsilon_\gamma - \epsilon_{\pi^0}}, \quad (4.3)$$

$$\frac{\partial W_\gamma}{\partial \epsilon_{\pi^0}} = -\frac{W_{\pi^0}}{\epsilon_\gamma - \epsilon_{\pi^0}}. \quad (4.4)$$

When the systematic uncertainties in ϵ_γ and ϵ_{π^0} are $\Delta\epsilon_\gamma$ and $\Delta\epsilon_{\pi^0}$, respectively, the systematic uncertainty in W_γ is written as

$$\frac{\Delta W_\gamma}{W_\gamma} = \frac{1}{\epsilon_\gamma - \epsilon_{\pi^0}} \sqrt{(\Delta\epsilon_\gamma)^2 + \left(\frac{W_{\pi^0}}{W_\gamma} \Delta\epsilon_{\pi^0}\right)^2}. \quad (4.5)$$

Therefore, the larger difference between ϵ_γ and ϵ_{π^0} is, the less the systematic uncertainty of W_γ is. In addition, the better the signal-to-background ratio W_γ/W_{π^0} is, the less the systematic uncertainty of W_γ is.

4.2 χ_{CES}^2 Cut Efficiency

The χ_{CES}^2 cut efficiencies for photons and the background, ϵ_γ and ϵ_{π^0} , are determined by using a detector simulation, because we have no photon test beam. The detector simulation (QFL) based on actual EM shower data from test beam electrons has been developed. Test beam data are taken at beam energies of 5, 10, 25, 50, 100, and 150 GeV. When the QFL simulates EM showers of photons and electrons, test beam events are chosen from the test beam runs with energy immediately above and below the given EM shower energy. Interpolation between the two test beam energies uses the same scaling formula as Equation 3.12 which is the overall energy dependence of the shower fluctuation observed in the test beam runs.

To simulate an EM shower initiated by a photon, the difference between an EM shower initiated by a photon and that by an electron have to be properly taken into account. Since the longitudinal development of photon and electron showers is slightly different, the shower statistics and profile fluctuations are different. The photon identification relies on an accurate accounting of the fluctuations around the mean EM shower profile. Hence an adjustment to the fluctuations of the test beam electrons is made to obtain the expected fluctuations of

an EM shower initiated by a photon in the QFL simulation. The scale of the fluctuations is taken as directly proportional to the square root of the average number of secondary electrons and positrons crossing the CES for a given EM shower energy. This number of secondary electrons and positrons in turn is proportional to the average pulse height observed in the CES. The CES response which is expected on the basis of the longitudinal shower development parameterized with the Γ function is used to characterize the energy dependence of the shower statistics in the CES. The longitudinal shower development is expressed as the development of number of secondary electrons and positrons. The number of secondaries is given as a function of the depth t by

$$\frac{1}{N} \frac{dN}{dt} = \frac{b^{\alpha+1}}{\Gamma(\alpha+1)} \cdot t^{\alpha} e^{-bt} \quad (4.6)$$

where α and b are parameters dependent on the calorimeter material and weakly dependent on the EM shower energy E [29]. The parameter α is written as

$$\alpha = b \cdot (t_{\max} + \delta) \quad (4.7)$$

where t_{\max} is the shower maximum depth. The shower maximum for a photon shower is deeper than that for an electron shower. The energy independent shift δ in shower maximum is taken to be zero for electrons, while that for photons is taken to be $0.6 X_0$.

In the following, estimations of the χ_{CES}^2 cut efficiencies for photons and the background by the QFL simulation are described.

4.2.1 Photon Efficiency

The χ_{CES}^2 cut efficiency for single photons is defined as a ratio of the number of photons with $\chi_{\text{CES}}^2 < 4$ to the number of photons with $\chi_{\text{CES}}^2 < 20$ in a sample of photons. The values have been determined at several p_T 's by using photons simulated by the QFL. The efficiency shows a weak energy dependence but is approximately 0.8 as shown in Figure 4.1.

Fortunately we can cross-check the χ_{CES}^2 cut efficiency obtained from the QFL simulation with a sample of η mesons that two photons from an η decay come into adjacent towers of an EM cluster in the CEM. Every event in the η sample is required to include at least

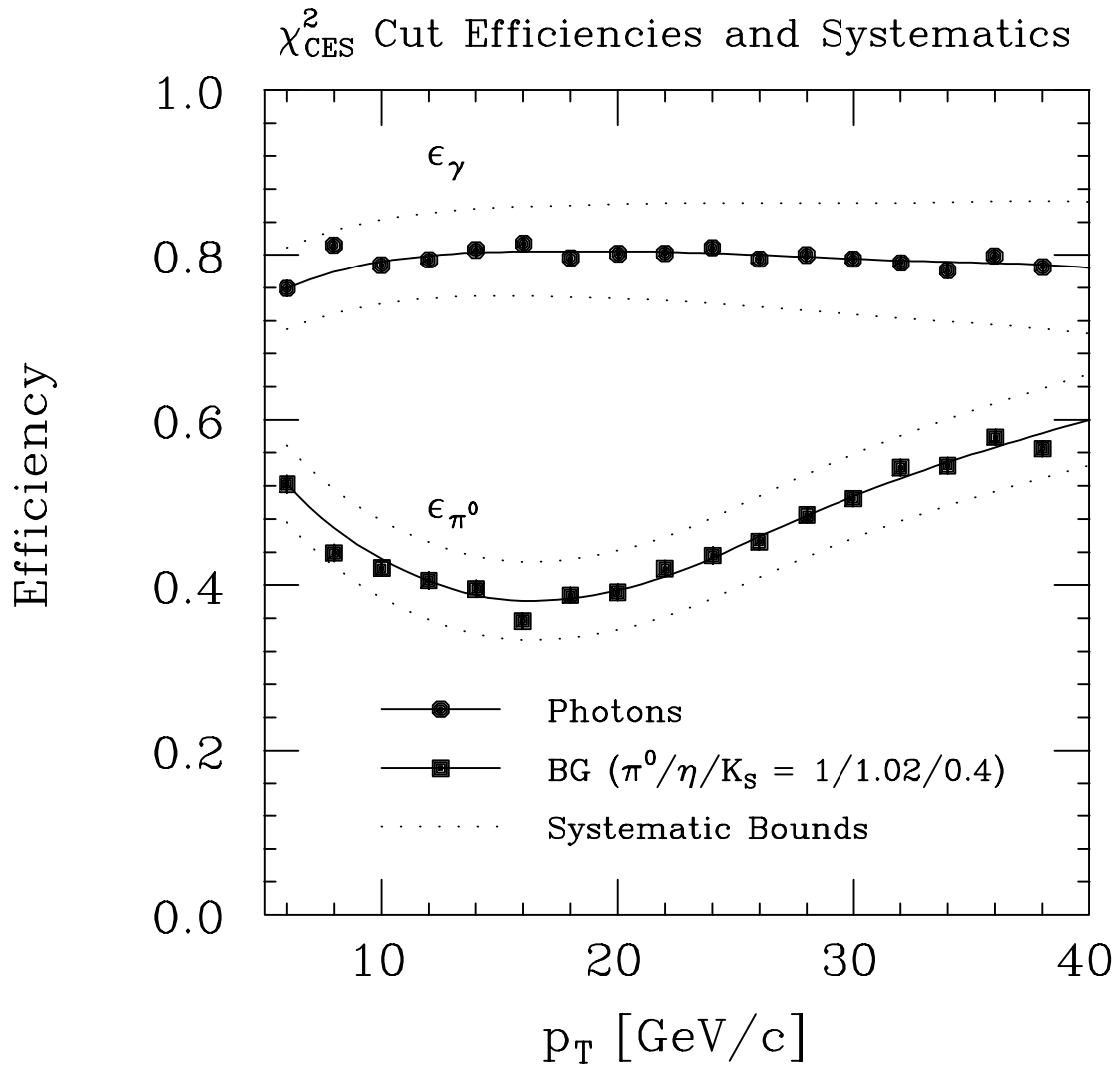


Figure 4.1: χ_{CES}^2 cut efficiencies for photons and the background are shown. These efficiencies are estimated by the QFL simulation.

one isolated EM cluster in the central region. The EM cluster is required to contain two strip clusters in adjacent towers and to contain one or two wire clusters. Each strip cluster must be in a separate tower in the EM cluster to accurately measure the energy of both photons. Since the two photons may overlap in the wire view, one or two wire clusters are less restrictively required in the EM cluster. When there are two wire clusters, we assume that the strip cluster having the highest energy is associated with the wire cluster having the highest energy. The invariant mass of two photons is calculated from the directions of both photons reconstructed from the positions of CES clusters and the event vertex, and the energies of both photons measured in each tower. The η mass peak is shown in Figure 4.2.

We can compare only the χ_{Strip}^2 distributions of the data and the QFL simulation because two wire clusters may overlap. In order to remove contamination due to the background in the η mass region from the χ_{Strip}^2 distribution, the scaled χ_{Strip}^2 distribution of photons in the sideband areas is subtracted from that of photons in the η mass region. In Figure 4.3, the χ_{Strip}^2 distribution of single photons simulated by the QFL is compared with that of single photons with the average energy of 7 GeV ($p_T = 6 \text{ GeV}/c$) in the η mass region. The comparison of the QFL simulation with the data validates the accuracy of the QFL simulation which is used to obtain the χ_{CES}^2 cut efficiency for photons.

4.2.2 Background Efficiency

Because the HAD/EM cut and the isolation cut are applied in the event selection, the background is free of jets but is dominated by single neutral mesons such as π^0 , η , and K_S^0 . Therefore, χ_{CES}^2 efficiency for the background depend on the particle composition of the background.

The relative production rate of η to π^0 , η/π^0 , is measured by reconstructing η and π^0 from two photons in the inclusive photon data. Every event in the η/π^0 sample is required to include at least one isolated EM cluster in the central region. The CES cluster is limited within 3 strips and 3 wires instead of 11 strips and 11 wires for the standard CES clusters, to separate the closely spaced photons from π^0 as well as η . Three channels centered on the shower center is expected to contain 90% of the shower energy on the basis of the standard

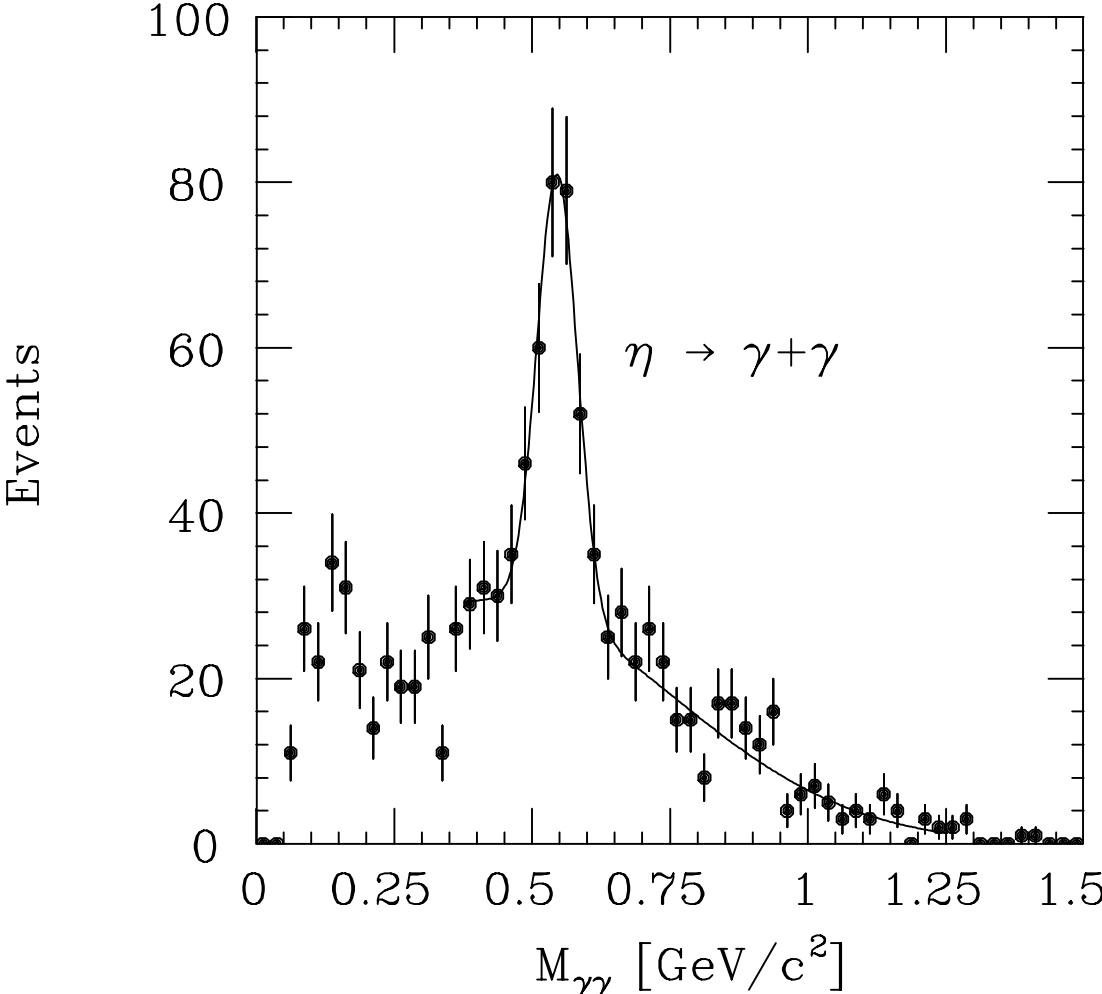


Figure 4.2: Two-photon mass distribution with 11-channel CES clusters. The η meson peak are evident, while the π^0 peak is suppressed by the large clustering window.

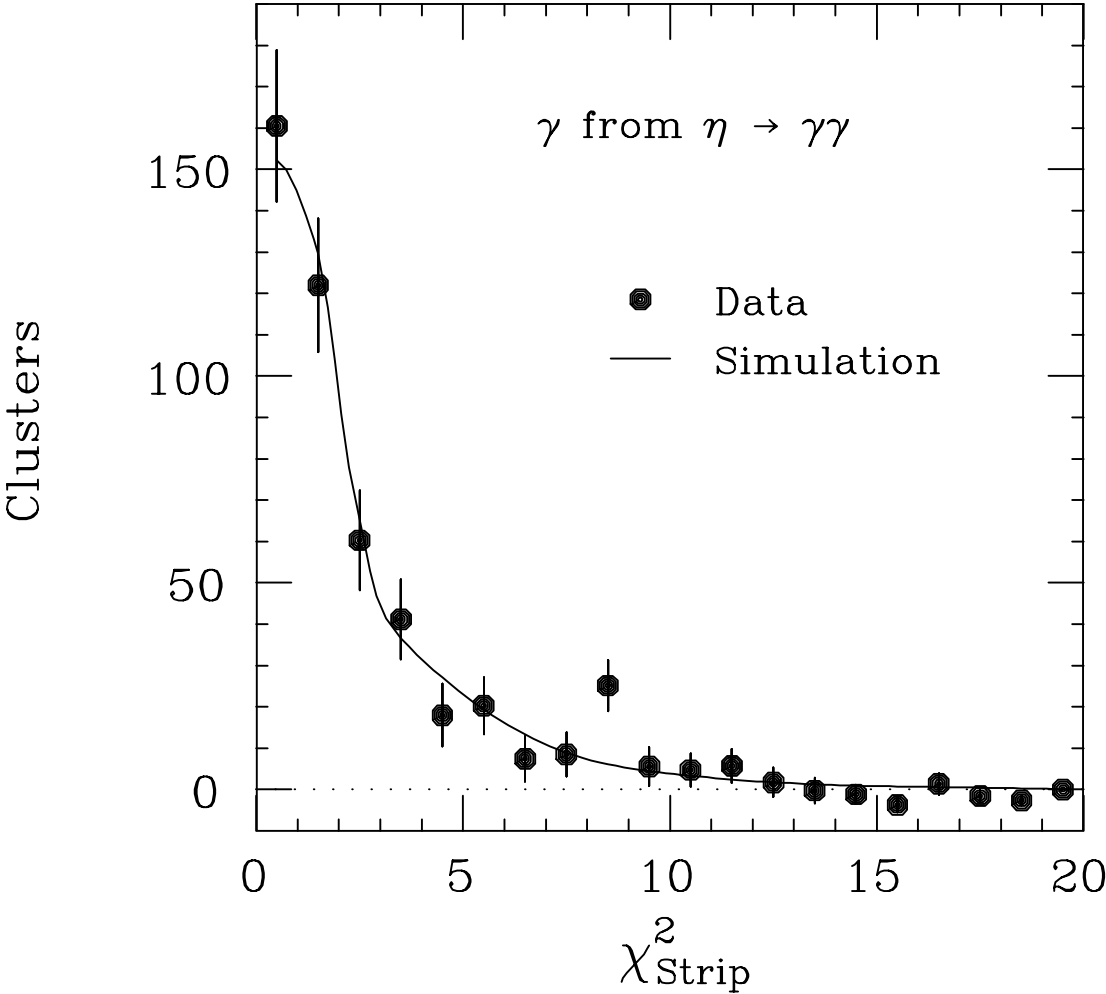


Figure 4.3: The χ^2_{Strip} distribution for photon candidates in the η mass region is compared with simulated single photons from $\eta \rightarrow \gamma\gamma$.

shower profile. The EM cluster is required to contain two strip clusters in adjacent towers and to contain one or two wire clusters. When there are two wire clusters, we assume that the strip cluster with the highest energy is associated with the wire cluster with the highest energy. Multi- π^0 backgrounds are reduced by requiring a ratio of the energy sum of extra CES clusters to that of the highest two CES clusters to be less than 0.3. Misidentification of single photon showers as π^0 at the tower boundary is reduced by using the tower energy asymmetry $|E_1 - E_2|/(E_1 + E_2)$ where E_1 and E_2 are two tower energies in the EM cluster. Two photons from a π^0 decay have a flat distribution of the energy asymmetry, while the energy asymmetry distribution for the misidentified single photon showers centers around 1. Thus the tower energy asymmetry is required to be less than 0.8. The reconstructed invariant mass ($M_{\gamma\gamma}$) is shown in Figure 4.4.

The multi- π^0 background in the invariant mass distribution of the η/π^0 sample is estimated by fitting a function which consists of two Gaussians and a polynomial to the data. The number of events in the η mass region ($475 < M_{\gamma\gamma} < 625$ [MeV/ c^2]) is

$$N_\eta = 368 \pm 19.2$$

and that in the π^0 mass region ($75 < M_{\gamma\gamma} < 225$ [MeV/ c^2]) is

$$N_{\pi^0} = 391 \pm 19.8$$

where the errors are the statistical uncertainties. The multi- π^0 background in the η mass region is

$$B_\eta = 164.4 \pm 12.8 \pm 10$$

and that in the π^0 mass region is

$$B_{\pi^0} = 101.2 \pm 10.1^{+31}_{-36}$$

where the first errors are the statistical uncertainties and the second ones are the systematic uncertainties in the estimated distribution for the multi- π^0 background. The η/π^0 production ratio is obtained from

$$\eta/\pi^0 = \frac{(N_\eta - B_\eta)/A_\eta}{(N_{\pi^0} - B_{\pi^0})/(A_{\pi^0} + \frac{\gamma}{\pi^0} A_\gamma)} \quad (4.8)$$

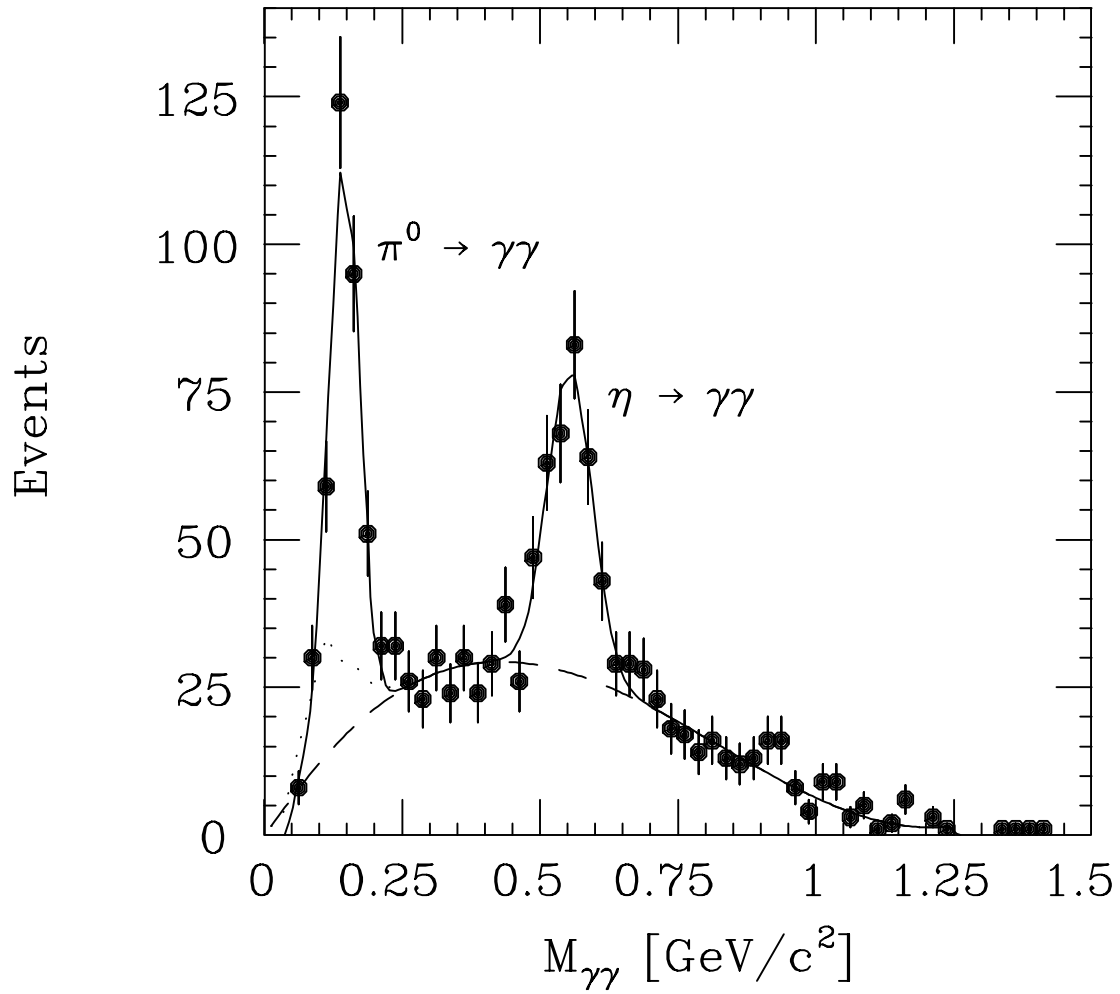


Figure 4.4: Two-photon mass distribution using 3-channel CES clusters. The π^0 and η mesons mass peaks are evident. Also shown is the estimated background distribution (dashed curve) and the sum of single photon contribution plus background (dotted curve). After acceptance correction for η 's and π^0 's, the η/π^0 ratio is $1.02 \pm 0.15(\text{stat}) \pm 0.23(\text{sys})$.

where A_{π^0} is the acceptance for $\pi^0 \rightarrow \gamma\gamma$ and A_η is the acceptance for $\eta \rightarrow \gamma\gamma$ multiplied by the branching ratio. These acceptances are estimated by the QFL simulation and are corrected to the reconstructed mass resolutions. The correction are estimated from two Gaussians in the background fit. The numbers are as follows:

$$\begin{aligned} A_\eta &= (7.76 \pm 0.23 \pm 0.72) \times 10^{-3} \\ A_{\pi^0} &= (8.58 \pm 0.33 \pm 0.54) \times 10^{-3} \\ A_\eta &= (4.44 \pm 0.24 \pm 0.28) \times 10^{-3} \end{aligned}$$

where the first errors are the statistical uncertainties and the second ones are the systematic uncertainties on the correction to the mass resolutions. γ/π^0 is the production ratio of misidentified single photons to π^0 's. To estimate γ/π^0 , the asymmetry of two photons in the η/π^0 sample to which the tower energy asymmetry cut is not applied is compared with that simulated by the QFL. The number is

$$\gamma/\pi^0 = 0.58 \pm 0.16^{+0.24}_{-0.2}$$

where the statistical and systematic uncertainties are taken conservatively. Finally, we have obtained [24, 25]

$$\eta/\pi^0 = 1.02 \pm 0.15(\text{stat}) \pm 0.23(\text{syst}).$$

The systematic uncertainty is calculated from the statistical uncertainties on the number of events in the data and on γ/π^0 . The systematic uncertainty is calculated from the systematic uncertainties on B_{π^0}, B_η , and γ/π^0 , and the statistical and systematic uncertainties on acceptances.

The K_S^0 decay $K_S^0 \rightarrow \pi^0\pi^0$ also contributes slightly to the background to single photons, in particular, at the high p_T region. For completeness of the background simulation by QFL, this contribution is also added to the background composition. K_S^0 's were reconstructed in the charged decay mode $K_S^0 \rightarrow \pi^+\pi^-$, and the K_S^0 production ratio to charged π has been measured [26]. On the basis of this measurement and the isospin invariance, a value of K_S^0/π^0 of 0.4 is used in the QFL simulation.

The χ_{CES}^2 cut efficiency for the background is evaluated by using the QFL simulation with the production ratio of neutral mesons π^0 , η , and K_S^0 . Figure 4.1 shows the p_T dependence of

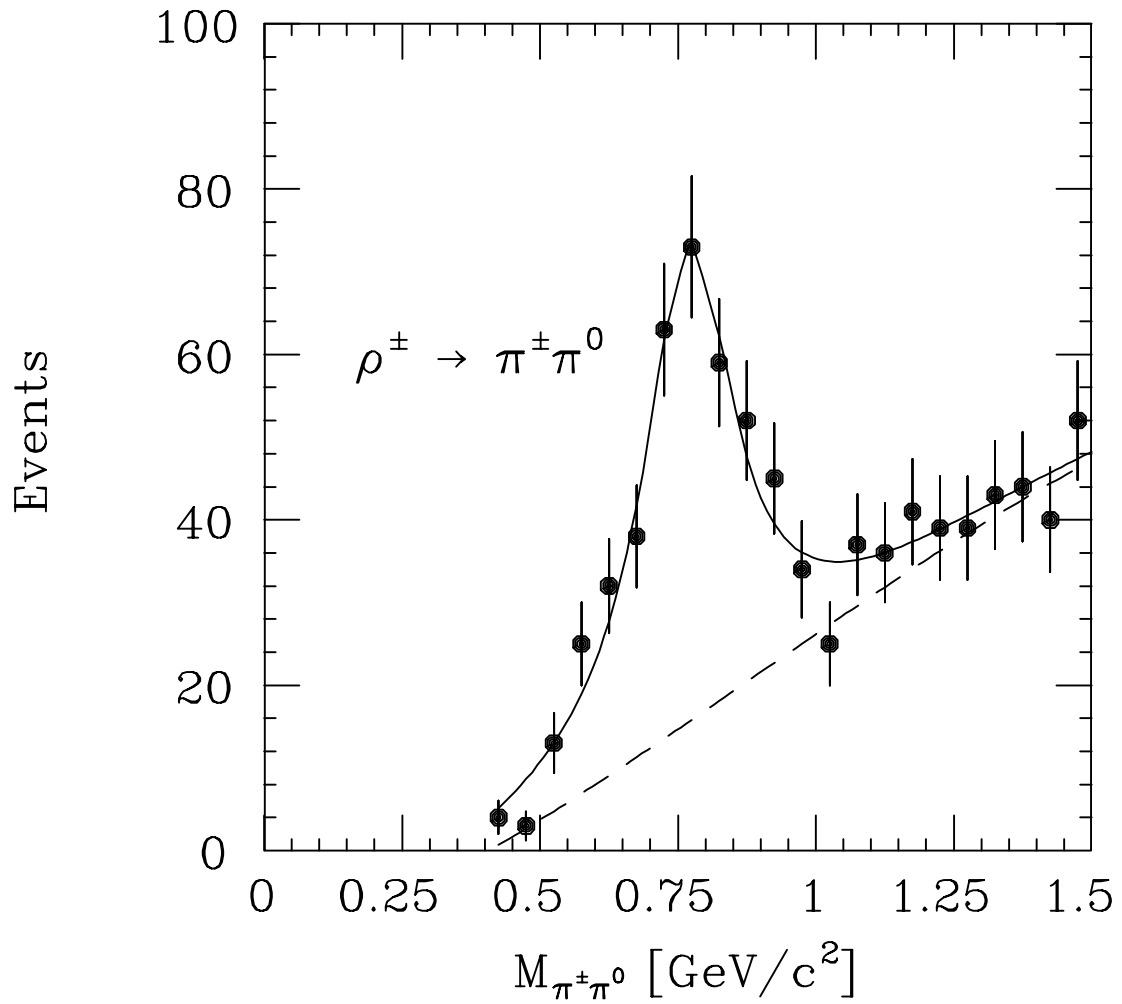


Figure 4.5: Photon candidate plus charged track mass distribution, showing the ρ^{\pm} meson peak used as a cross-check for the χ^2_{CES} efficiency of π^0 's.

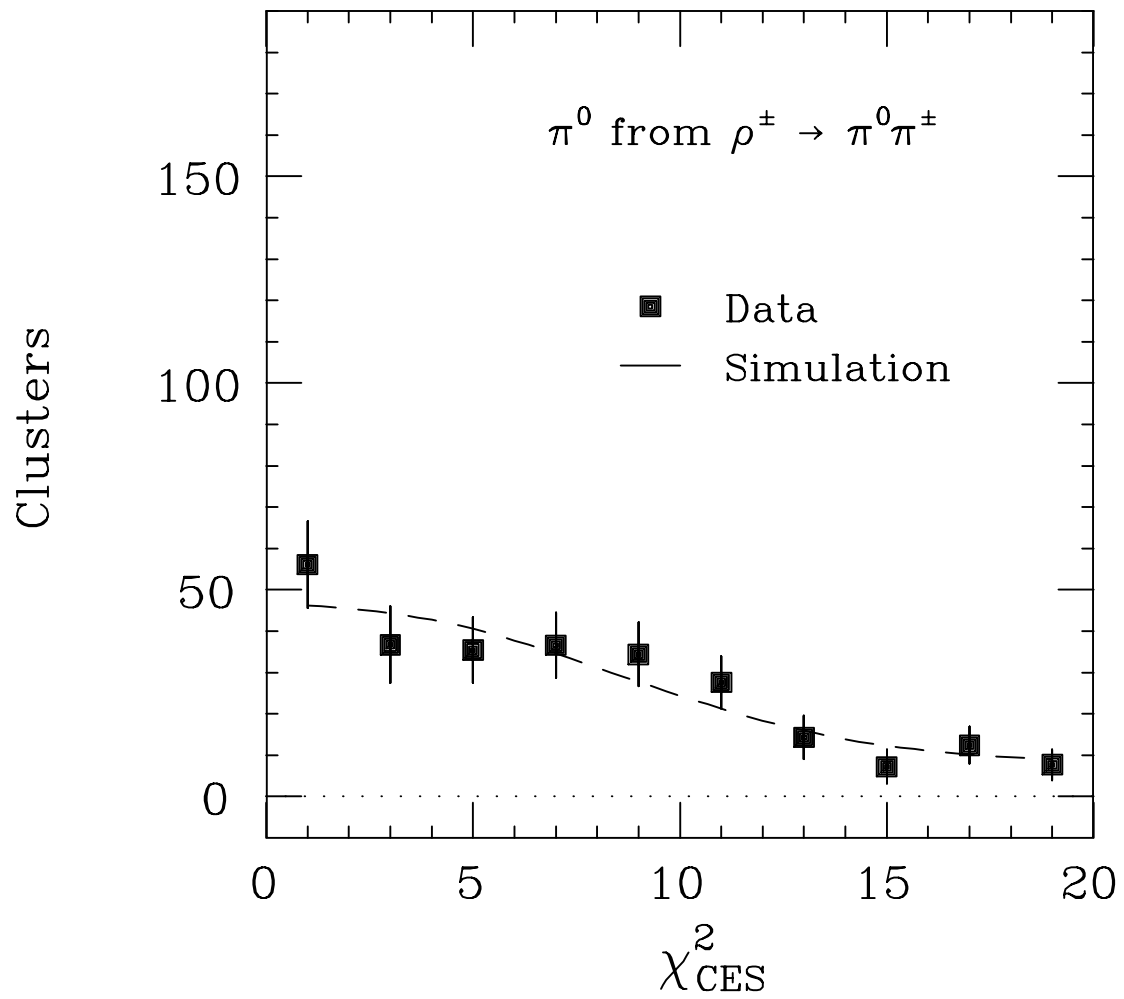


Figure 4.6: The χ_{CES}^2 distribution for the π^0 's from the ρ^\pm mass peak is compared with simulated single π^0 's.

the χ_{CES}^2 cut efficiency for the background. Because two photons from a π^0 decay get close, the EM showers become indistinguishable from a single shower at high p_{T} . Therefore the χ_{CES}^2 cut efficiency for the background rises at high p_{T} . As the p_{T} decreases the likelihood of observing one photon from the η as a single photon increases, causing the χ_{CES}^2 cut efficiency to rise as p_{T} goes down.

In order to cross-check the χ_{CES}^2 cut efficiency for π^0 , we used a sample of ρ^\pm mesons obtained by looking for a neutral EM cluster associated with a single charged track close by. The charged track is required to have $p_{\text{T}} > 0.8$ GeV/ c . The invariant mass of a neutral EM cluster and a charged track is calculated for all such combinations in the ρ^\pm sample. A clear ρ^\pm peak is shown in Figure 4.5. The χ_{CES}^2 distribution for π^0 's from ρ^\pm decays has been constructed by fitting the Breit-Wigner form excess above a smooth background to each bin of the χ_{CES}^2 distribution for π^0 candidates. The data (squares) and the simulation (dotted line) exhibit similarly a good agreement as shown in Figure 4.6.

4.3 Systematics in Photon Efficiency

The χ_{CES}^2 cut efficiency for photons is evaluated by using the QFL simulation which is based on EM shower data of test beam electrons because we have no photon test beam. It is necessary for the accuracy of the QFL simulation to be validated. Difference in the χ_{CES}^2 cut efficiency between electrons in the $W \rightarrow e\nu$ sample and those simulated by the QFL is shown in Figure 4.7 (d). For electron showers at about 40 GeV/ c of p_{T} , the QFL simulation predicts the χ_{CES}^2 cut efficiency to the level of 5%. Difference in the χ_{Strip}^2 cut efficiency between photons in the $\eta \rightarrow \gamma\gamma$ sample and the QFL simulation is also shown, and it constrains the systematic uncertainty at low p_{T} of about 6 GeV/ c .

There are three sources of the systematic uncertainty for simulating photon showers: the difference between photon and electron shower fluctuations, the difference in shower shape between photon and electron showers, and the saturation of the gas gain in the CES. The uncertainties are evaluated by varying each source of uncertainty in the QFL simulation, plotting the difference between the mean χ_{CES}^2 cut efficiency and the systematic bound,

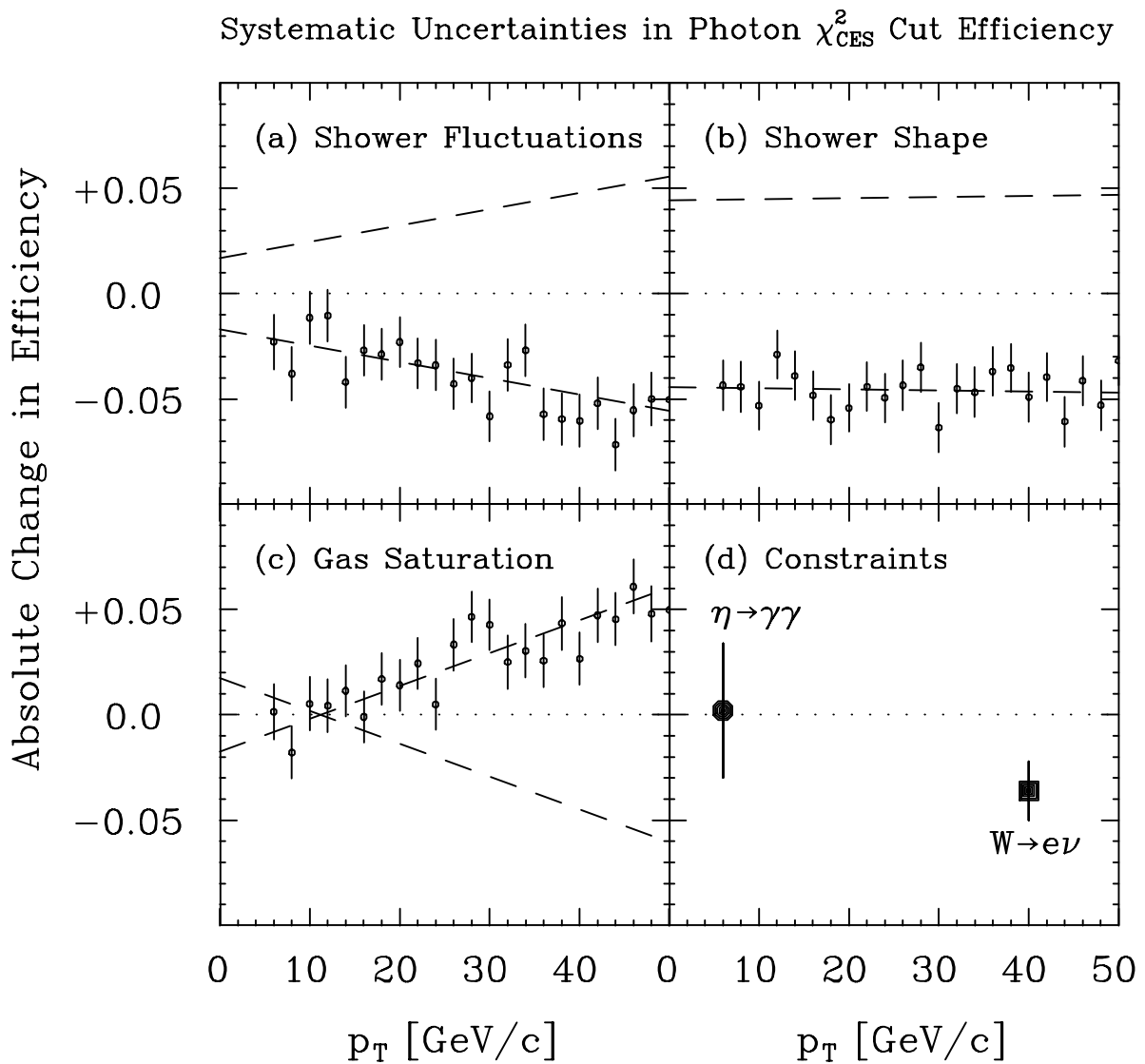


Figure 4.7: The systematic uncertainty on the photon χ_{CES}^2 cut efficiency is shown: (a) The amount of statistical fluctuations in the photon shower, (b) the lateral shape of the photon shower, and (c) the affect of CES gas saturation. (d) Two constraints on the systematic uncertainties are shown: the difference between simulation and data for the χ_{strip}^2 efficiency for photons from $\eta \rightarrow \gamma\gamma$, and the difference between the simulation and data for the χ_{CES}^2 efficiency for W electrons.

fitting a straight line to the plot, and symmetrizing the uncertainty. The three systematic uncertainties are added in quadrature. In Figure 4.1 the overall systematic uncertainty in the χ_{CES}^2 cut efficiency for photons is presented.

4.3.1 Shower Fluctuations

The χ_{CES}^2 is very sensitive to the shower fluctuations, that is, the number of secondary electrons and positrons in an EM shower passing through the CES. The number of secondary particles passing through the CES in a photon induced EM shower is less than that in an electron induced EM shower because the shower maximum occurs later for a photon induced EM shower than for an electron induced EM shower. The QFL simulation takes account of this difference by increasing the position of the shower maximum by $\delta = 0.6 X_0$. This change by $\delta = 0.6 X_0$ in the shower maximum position is in reasonable agreement with an EM shower simulation by GEANT3 [28], when the ratio of number of secondary particles passing through the CES in a photon shower to that in an electron shower is compared [25]. The Particle Data Group estimates $\delta = 1.0 X_0$ for difference in the shower maximum between electrons and photons [27]. Taking the difference between the photon χ_{CES}^2 cut efficiency with $\delta = 0.6 X_0$ and that with $\delta = 1.0 X_0$, we obtain the absolute change in the χ_{CES}^2 cut efficiency as shown in Figure 4.7 (a). The errors on points are statistical uncertainties. The upper systematic uncertainty is taken as the absolute value of the lower systematic uncertainty.

4.3.2 Shower Shape

The χ_{CES}^2 is sensitive to the shape of the shower profile. Since the QFL simulation based on test beam electron showers is used to estimate the χ_{CES}^2 cut efficiency, any differences between photons and electrons in the shape of the lateral shower profile will change the χ_{CES}^2 cut efficiency. To estimate these changes we use test beam electron showers with varying amounts of material in front of the CES. In Figure 4.8, the χ_{CES}^2 cut efficiency for 10-GeV test beam electrons as a function of amount of material in front of the CES. The first circular point, labeled A, corresponds to the amount of material in the test beam when the data for

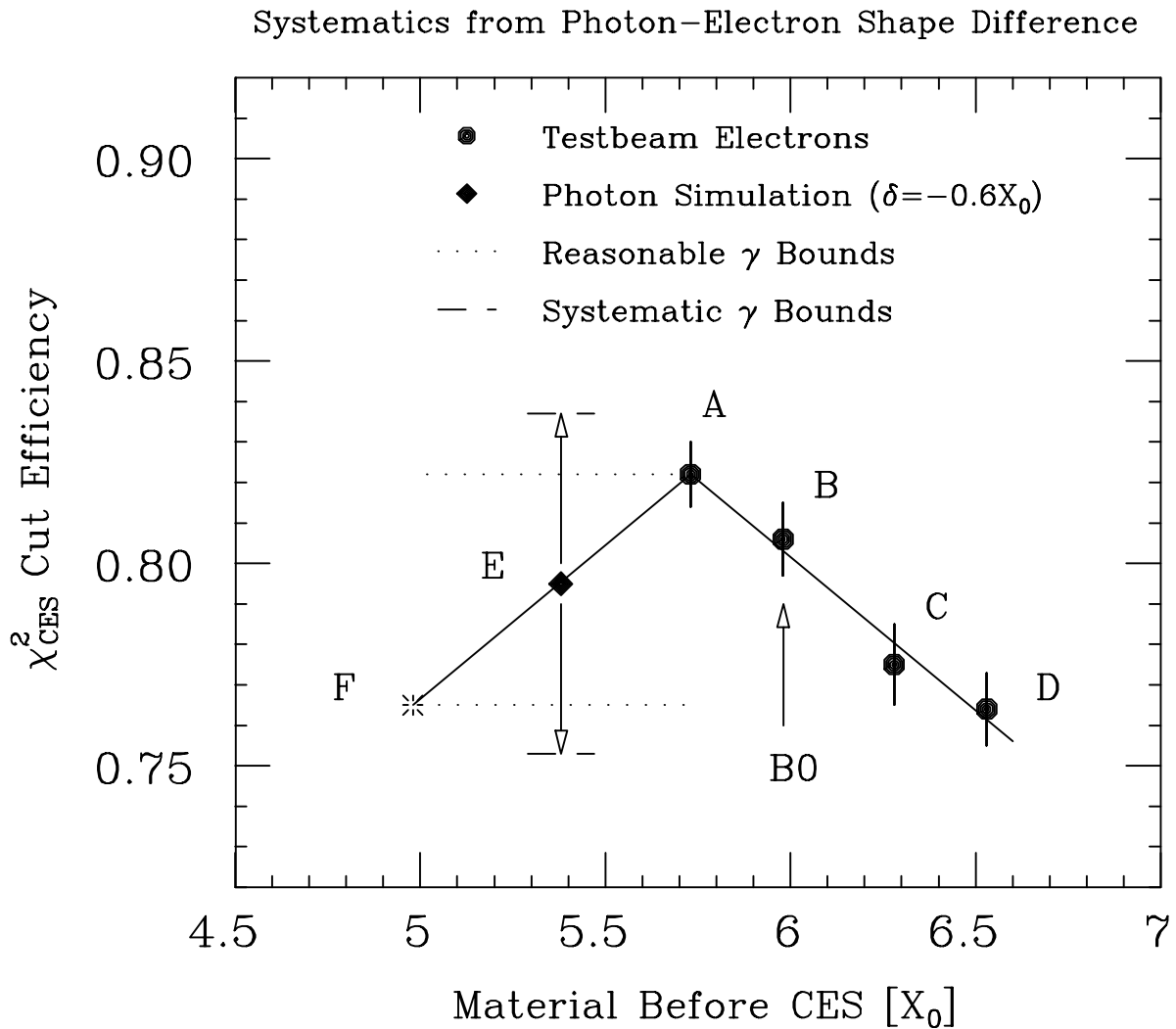


Figure 4.8: The χ_{CES}^2 cut efficiency for 10-GeV test beam electrons (points A–D) is shown as a function of the amount of material in front of the CES together with the expected value (point E) and the systematic bounds for photons. The point F indicates a reasonable lower bound. An arrow indicates the amount of material at B0 and the data at the point A is used to determine the standard shower profiles. The data at the points B and D are used to estimate the final systematic uncertainty of χ_{CES}^2 cut efficiency for photons with respect to difference in the shower shape between photons and electrons.

the standard electron shower profile were taken. As the amount of material increases, the shape changes and the fit of the standard shower profile worsens, reducing the χ_{CES}^2 cut efficiency. The change of the χ_{CES}^2 cut efficiency is linear as shown by the solid line.

If we decrease the amount of material from the point A, we expect the χ_{CES}^2 to worsen as well. We assume the same linear relation as determined when increasing the amount of material. The point marked B corresponds to the amount of material at B0. Photon induced EM showers have the shower maximum deeper by $0.6 X_0$ than electron showers and so we expect photon showers to have the χ_{CES}^2 cut efficiency predicted by moving along the solid line to a point $0.6 X_0$ less than the B0 position. The point, marked E, for photons has roughly the same efficiency as the B0 position for electrons.

Our assumption of linear decrease with material may be wrong. A reasonable upper bound (point A) on the χ_{CES}^2 cut efficiency for photons is to assume no change in the efficiency as decreasing the amount of material, and a reasonable lower bound (point F) is to move $1.0 X_0$ along the line instead of $0.6 X_0$. These bounds on the χ_{CES}^2 cut efficiency for photons are shown by dotted lines.

The difference between points B and D, which are $0.55 X_0$ apart, gives a systematic bound shown by the dashed lines which is more conservative than our reasonable bounds. To estimate the systematic uncertainty we use EM shower data from the point B and the point D in the QFL simulation. We take the difference in the χ_{CES}^2 cut efficiency between the two EM shower data as the systematic uncertainty. This absolute difference in the χ_{CES}^2 cut efficiency is shown in Figure 4.7 (b). The errors on the points are statistical uncertainties. The upper systematic uncertainty is taken as the absolute value of the lower systematic uncertainty.

4.3.3 Gas Saturation

The χ_{CES}^2 is sensitive to the normalized profile of the shower shape, which changes because of saturation of the gas gain. The test beam data used by the QFL simulation has little or no saturation because it was acquired at a relatively low anode voltage HV of 1390 V. The

effect of the saturation is installed in the QFL simulation as the correction which is estimated for the nominal anode voltage HV of 1450 V. The correction is measured by comparing the χ_{CES}^2 of test beam data acquired at $HV = 1470$ V with that at $HV = 1390$ V for test beam electrons of 10 GeV and 50 GeV. Define $\chi_{80}^2(E, HV)$ as the 80% efficient cut point in the χ_{CES}^2 distribution for test beam electrons of energy E acquired with the CES operating at the anode voltage of HV . The multiplication in χ_{80}^2 for gas saturation at 1470 V when going from 10 GeV to 50 GeV is given by

$$K_0 = \frac{\left(\frac{\chi_{80}^2(50 \text{ GeV}, 1470 \text{ V})}{\chi_{80}^2(10 \text{ GeV}, 1470 \text{ V})} \right)}{\left(\frac{\chi_{80}^2(50 \text{ GeV}, 1390 \text{ V})}{\chi_{80}^2(10 \text{ GeV}, 1390 \text{ V})} \right)}. \quad (4.9)$$

We measured K_0 in the strip view to be 1.158 ± 0.061 and K_0 in the wire view is 1.166 ± 0.066 , consistent within errors. Since the CES at B0 is operated at $HV = 1450$ V, three quarters of the way from 1390 V to 1470 V, we reduce the affect to three quarters of its mean value and obtain the multiplier $K_1 = 1.12 \pm 0.03$ in either view. To obtain the multiplier K appropriate for arbitrary energy, we assume a linear rise with energy as

$$K = 1 + (K_1 - 1) \frac{E[\text{GeV}] - 10}{50 - 10}. \quad (4.10)$$

We simulate gas saturation affect on the χ_{CES}^2 by multiplying the fluctuations by K when simulating electrons and photons in the QFL simulation. Since we do not know the exact energy dependence between 10 and 50 GeV, we take the value of the correction as the systematic uncertainty. The absolute difference between the χ_{CES}^2 cut efficiencies with and without the correction is shown in Figure 4.7 (c). The errors on the points are statistical uncertainties. The lower systematic uncertainty is taken to be opposite to the upper systematic uncertainty.

4.4 Systematics in Background Efficiency

The three sources of systematic uncertainty for the photons are also a source of systematic uncertainty for the background since the background consists of multiple photons primarily

from the decay of π^0 and η mesons. We take into account of the shower fluctuations, the shower shape, and the gas saturation and obtain the absolute difference in the χ_{CES}^2 cut efficiency for the background as shown in Figure 4.9. They are completely correlated to the corresponding photon uncertainties.

One additional source of systematic uncertainty is the background composition. The dominant uncertainty comes from the production ratio of η to π^0 mesons. Our measurement of the production ratio is $\eta/\pi^0 = 1.02 \pm 0.15 \pm 0.23$ where the first error is statistical and the second one is systematic. Combining both uncertainties in quadrature gives a total error of 0.27. We therefore run the QFL simulation for the background with $\eta/\pi^0 = 1.02$ for the mean value of the χ_{CES}^2 cut efficiency, and with $\eta/\pi^0 = 0.75$ and $\eta/\pi^0 = 1.30$ for the lower and upper systematic bounds.

The systematic uncertainty which comes from every source is evaluated by varying the source of uncertainty in the QFL simulation, plotting the difference between the mean χ_{CES}^2 cut efficiency and the systematic bound, fitting to a straight line and symmetrizing the uncertainty. The systematic uncertainties are all added in quadrature. In Figure 4.1 the overall systematic uncertainty in the χ_{CES}^2 cut efficiency for the background is presented.

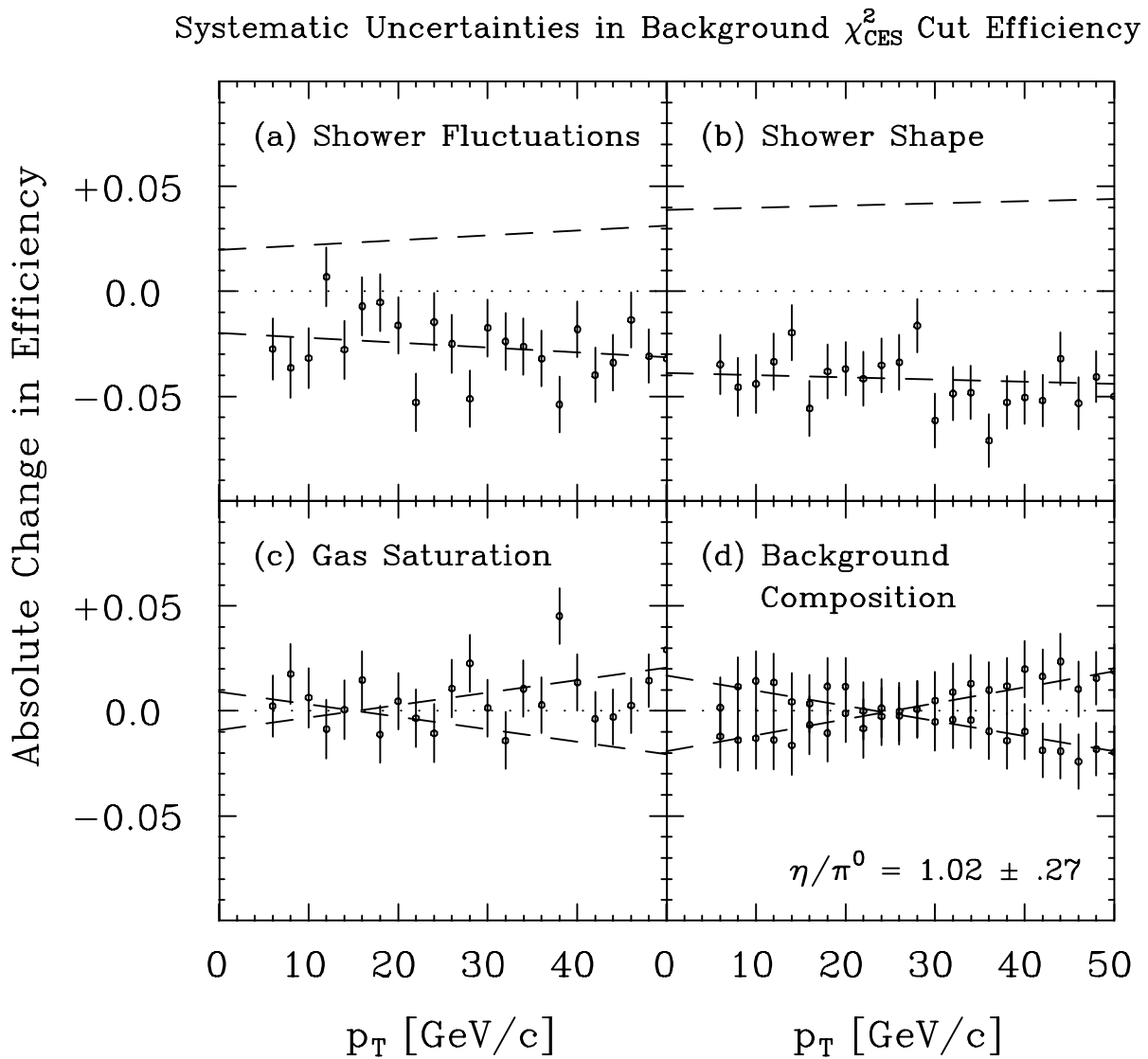


Figure 4.9: The systematic uncertainty on the background χ_{CES}^2 cut efficiency is shown: (a) The amount of statistical fluctuations in the photon shower, (b) the lateral shape of the photon shower, (c) the affect of CES gas saturation, and (d) the background composition.

Chapter 5

Data Analysis

The final event selection is described. The acceptance for the diphoton events is estimated with a Monte Carlo event generator. The photon identification is applied to the final diphoton data to obtain the number of diphoton events. This photon identification subtract the background due to neutral mesons decaying into multiple photons. The statistical and systematic uncertainties in the background subtraction are discussed.

5.1 Final Event Selection

The final event selection is required to make the photon identification effective. In the final event selection, the CES cluster selection, the CES fiducial cut, and p_T cut are applied to the diphoton data.

5.1.1 CES Cluster Selection

To eliminate obvious multi-photon backgrounds, selection criteria for the CES clusters are applied to CES clusters matching with each EM cluster in the diphoton data. Each of two photon candidates is required to have at least one strip cluster and at least one wire cluster in the CES. The strip cluster with the highest energy is assumed to be associated with the wire cluster with the highest energy. When there is the second wire cluster, the energy $E_{\text{Wire}}^{(2)}$

is corrected for the incident angle $\theta^{(1)}$, which is determined by the the highest strip cluster position $Z_{\text{Strip}}^{(1)}$ and the event vertex position Z_{Vertex} , as $E_{\text{Wire}}^{(2)} \rightarrow E_{\text{Wire}}^{(2)} \sin \theta^{(1)}$. When there is the second strip cluster, the energy $E_{\text{Strip}}^{(2)}$ is corrected for the incident angle $\theta^{(2)}$, which is determined by the the second strip cluster position $Z_{\text{Strip}}^{(2)}$ and the event vertex position Z_{Vertex} , as $E_{\text{Strip}}^{(2)} \rightarrow E_{\text{Strip}}^{(2)} \sin \theta^{(2)}$. In addition, $E_{\text{Strip}}^{(2)}$ is divided by the mean ratio $\langle \frac{E_{\text{Strip}}}{E_{\text{Wire}}} \rangle$, and is translated into the energy equivalent to E_{Wire} .

Each of two photon candidates in the diphoton data is required to satisfy the following criteria for the CES clusters:

- $\chi_{\text{Strip}}^2{}^{(1)} < 20$.
- $E_{\text{Strip}}^{(2)} < 1 \text{ GeV}$, if there is the second strip cluster.
- $E_{\text{Wire}}^{(2)} < 1 \text{ GeV}$ or $|X_{\text{Wire}}^{(2)} - X_{\text{Wire}}^{(1)}| < 7 \text{ cm}$, if there the second wire cluster.

Superscripts (1) and (2) indicate the highest energy CES cluster and the second highest energy CES cluster, respectively.

The position (X_{CES} and Z_{CES}) and χ_{CES}^2 of the photon candidate is defined by using those of the highest energy CES cluster as follows:

$$X_{\text{CES}} = X_{\text{Wire}}^{(1)}. \quad (5.1)$$

$$Z_{\text{CES}} = Z_{\text{Strip}}^{(1)}. \quad (5.2)$$

$$\chi_{\text{CES}}^2 = \frac{\chi_{\text{Wire}}^2{}^{(1)} + \chi_{\text{Strip}}^2{}^{(1)}}{2}. \quad (5.3)$$

The selection efficiency for CES clusters is studied with electrons in the W sample and the test beam electrons. Figure 5.1 shows the selection efficiency as a function of the energy of an EM cluster.

Furthermore, χ_{CES}^2 's of both photon candidates in the diphoton data are required to be less than 20 because the χ_{CES}^2 cut efficiency is defined as probability that EM clusters with $\chi_{\text{CES}}^2 < 20$ pass the tighter cut at $\chi_{\text{CES}}^2 = 4$.

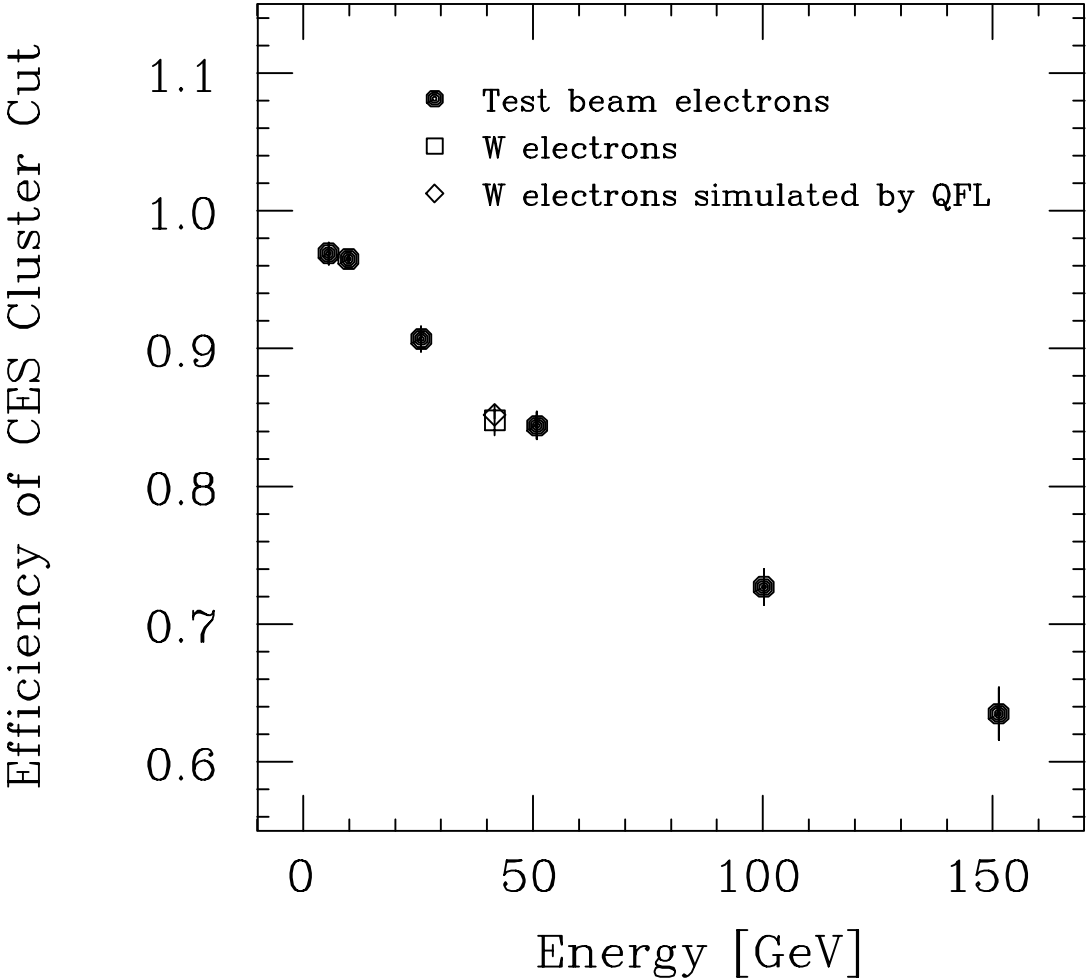


Figure 5.1: The selection efficiency for CES clusters is shown as a function of the EM cluster energy.

5.1.2 Geometrical Cut

Both photon candidates must come into the CES fiducial volume in which the standard shower profile can be properly fitted to CES clusters. The CES fiducial volume is defined in the CES local coordinates as follows:

- $|X_{\text{CES}}| < 17.5 \text{ cm}$.
- $14 < |Z_{\text{CES}}| < 217 \text{ [cm]}$.

The acceptance of the geometrical cut for diphoton events is discussed later.

5.1.3 Kinematical Cut

The kinematical variables for a photon candidate are defined by the corrected the EM cluster energy, the positions of the selected CES clusters, and the event vertex position. The EM cluster energy is corrected for the non-uniformity of energy response within a tower. This correction is based on the electron test beam data, and is accurate to within 1.1% over the CEM fiducial region [13]. The tower-to-tower response is also corrected on the basis of the relative response scale for each tower which is determined by comparing the E/p distributions. A sample of about 17000 electrons with $E_T > 12 \text{ GeV}$ is used to get the E/p distributions for all CEM towers.

By using the corrected EM cluster energy, E , together with the Z position of the selected CES strip cluster, Z_{CES} , and the event vertex Z_{Vertex} , the p_T of a photon candidate is defined as

$$p_T = \frac{R_{\text{CES}}}{\sqrt{R_{\text{CES}}^2 + (Z_{\text{CES}} - Z_{\text{Vertex}})^2}} \cdot E/c \quad (5.4)$$

where R_{CES} is the perpendicular distance from the beam line to the CES. With the X position of the selected CES wire cluster, X_{CES} , the azimuthal angle of the photon candidate is defined as

$$\phi = \phi_0 + \tan^{-1} \frac{X_{\text{CES}}}{R_{\text{CES}}} \quad (5.5)$$

where ϕ_0 is the azimuthal angle of the center of the CEM module which includes the EM cluster.

The kinematical cut requires p_T 's of both photon candidates to be between 10 GeV/ c and 35 GeV/ c . The lower limit comes from the level-2 trigger threshold. The higher p_T limit is bound by the ability of the photon identification by the χ_{CES}^2 cut efficiencies. As shown in Figure 4.1, the higher limit turns out to be about 35 GeV/ c . The higher limit of 35 GeV/ c is fortunately larger than the luminosity limit as shown in Figure 1.1.

5.1.4 Final Diphoton Data

After all these requirements for diphoton candidates, 152 events remain in the final diphoton data set. The selection criteria for the photon candidates are summarized in Table 5.1. Every event in the final diphoton data set includes two photon candidates satisfying those selection criteria.

The missing E_T significance for the final diphoton data is shown in Figure 3.4 (d). The distribution is consistent with the curve expected from the overall energy resolution, and shows that the final diphoton data are ordinary QCD events.

5.2 Acceptance Calculation

The acceptance of the geometrical cut for diphoton events is estimated with the Monte Carlo event generator PYTHIA 5.6 [46, 47, 48, 49]. PYTHIA is used to generate both subprocesses of the quark annihilation ($q\bar{q} \rightarrow \gamma\gamma$) and the gluon fusion ($gg \rightarrow \gamma\gamma$). Events are generated over wider η range ($|\eta| < 2.5$) than the η coverage of the central detector and from lower p_T ($p_T > 5$ GeV/ c) than the level-2 trigger threshold. This is because the kinematics of both photons are smeared owing to the initial parton bremsstrahlung and the k_T smearing. After generating events, both photons in each event are required to come into the central region ($|\eta| < 0.9$).

To estimate the acceptance for the p_T distribution, two p_T distributions before and after

Trigger
$E_T^{\text{Level2}} > 10 \text{ GeV}$
EM Cluster Cut
$\text{HAD/EM} < 0.055 + 0.045 \times E[\text{GeV}]/100$ $\text{LSHR} < 0.2$ No track $I_{\text{Border}} < 0.1$
CES Cluster Cut
$\chi_{\text{Strip}}^{2(1)} < 20$ $E_{\text{Strip}}^{(2)} < 1 \text{ GeV}$ $E_{\text{Wire}}^{(2)} < 1 \text{ GeV}$ or $ X_{\text{Wire}}^{(2)} - X_{\text{Wire}}^{(1)} < 7 \text{ cm}$ $\chi_{\text{CES}}^2 < 20$
CES Fiducial Cut
$ X_{\text{CES}} < 17.5 \text{ cm}$ $14 < Z_{\text{CES}} < 217 [\text{cm}]$
Kinematical Cut
$10 < p_T < 35 [\text{GeV}/c]$

Table 5.1: Selection criteria for both photon candidates in the final diphoton data are summarized.

the geometrical cut are compared. The first p_T distribution is filled with events in which both photons come into the central region ($|\eta| < 0.9$). The second one is filled with events in which both photons come into the CES fiducial volume. Both p_T distributions contain both photons in each event. The acceptance is defined as a ratio of number of photons in a p_T bin after the geometrical cut to that in the same bin before the cut. The acceptance for the p_T distribution is shown in Figure 5.2 where error bars are statistical uncertainties. This acceptance is used for calculating the cross section.

When the acceptance for the p_T distribution was estimated, we used PYTHIA with

Parton Density	Geometrical Acceptance	
	without p_T cut	with p_T cut
EHLQ Set 1	0.437 ± 0.001	0.438 ± 0.003
EHLQ Set 2	0.437 ± 0.001	0.437 ± 0.003
DO Set 1	0.440 ± 0.001	0.444 ± 0.003
DO Set 2	0.438 ± 0.001	0.442 ± 0.003
Q^2 Definition	Geometrical Acceptance	
	without p_T cut	with p_T cut
$Q^2 = 4p_T^2$	0.436 ± 0.001	0.434 ± 0.003
$Q^2 = \frac{1}{4}p_T^2$	0.439 ± 0.001	0.440 ± 0.002

Table 5.2: The geometrical acceptances for diphoton events with and without the kinematical cut are summarized. Events are generated by PYTHIA with several parton distributions and definitions of the factorization scale Q^2 .

EHLQ set 1 [39] for the parton distribution and $Q^2 = p_T^2$ for the factorization scale Q^2 , and the kinematical cut was applied to neither photon. The overall acceptance is 0.437 ± 0.001 , where the overall acceptance is a ratio of total number of photons after the geometrical cut to that before the geometrical cut. When other parton distributions, EHLQ set 2 [40], DO set 1 and set 2 [41], are employed with the factorization scale of $Q^2 = p_T^2$, values of the overall acceptance are about 0.44 without the kinematical cut as shown in Table 5.2. When the kinematical cut is also applied to both photons, values of the overall acceptance are still consistent with those without the kinematical cut. In addition, the overall acceptances calculated with the factorization scales of $Q^2 = 4p_T^2$ and $Q^2 = \frac{1}{4}p_T^2$ for the parton distribution of EHLQ set 1 are also presented in Table 5.2. Those acceptances calculated with several conditions are consistent within the level of about 2%.

In chapter 6, we will study the correlations between the two photons by using three kinematical variables: a ratio of p_T 's of both photons, z ; an opening angle between both photons in the azimuth, $\Delta\phi$; and a vector sum of p_T of both photons, k_T . Acceptances

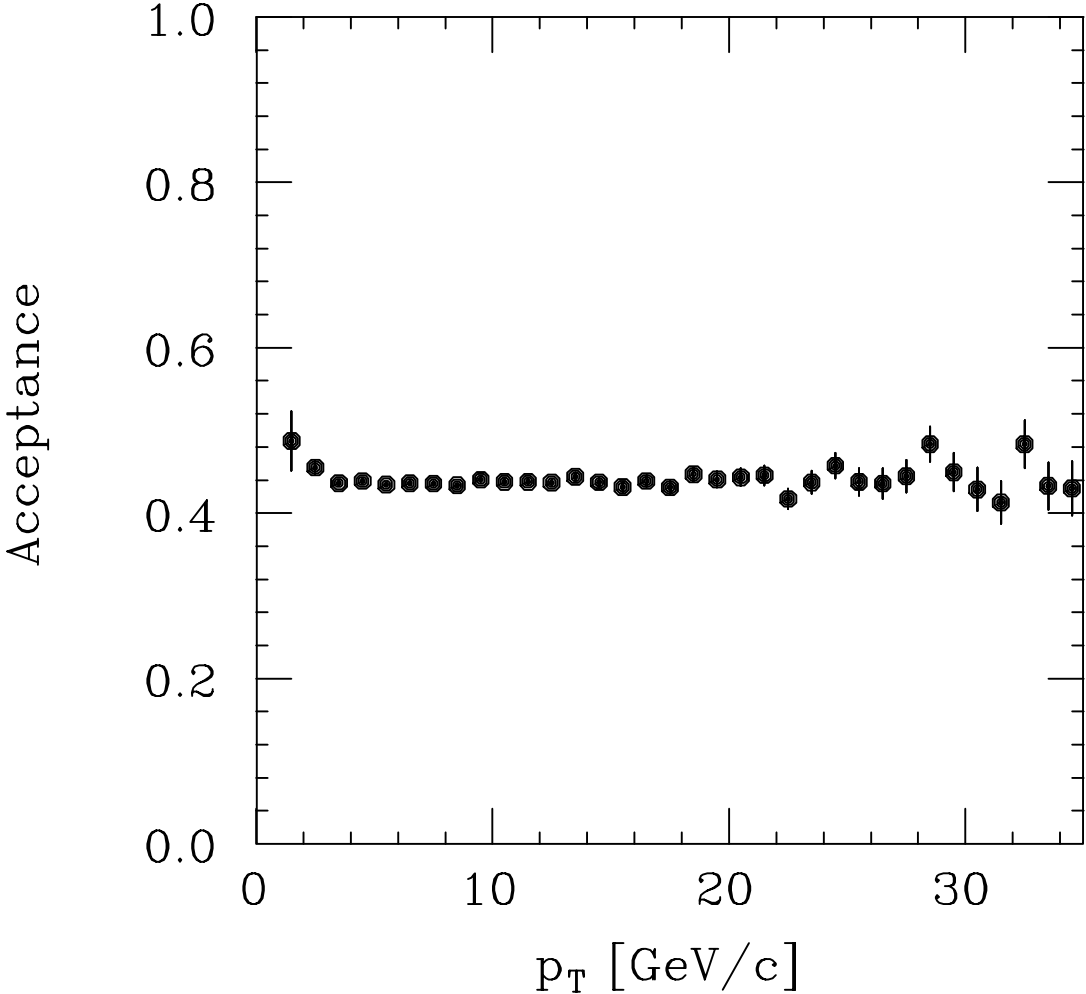


Figure 5.2: The geometrical acceptance for photons in the final diphoton data is shown as a function of p_T . Events to estimate the acceptance are simulated by PYTHIA.

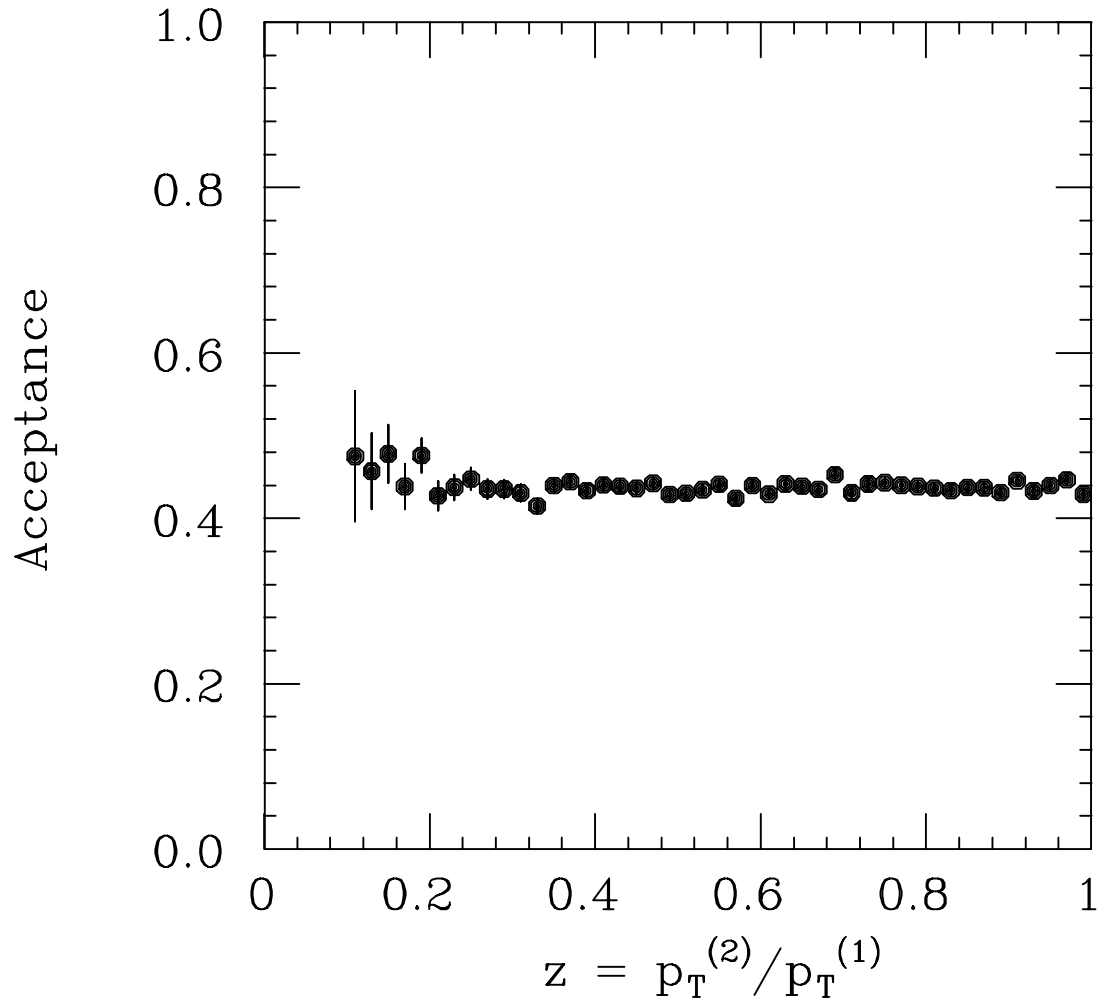


Figure 5.3: The geometrical acceptance for photons in the final diphoton data is shown as a function of the p_T ratio of two photons (z). Events to estimate the acceptance are simulated by PYTHIA.

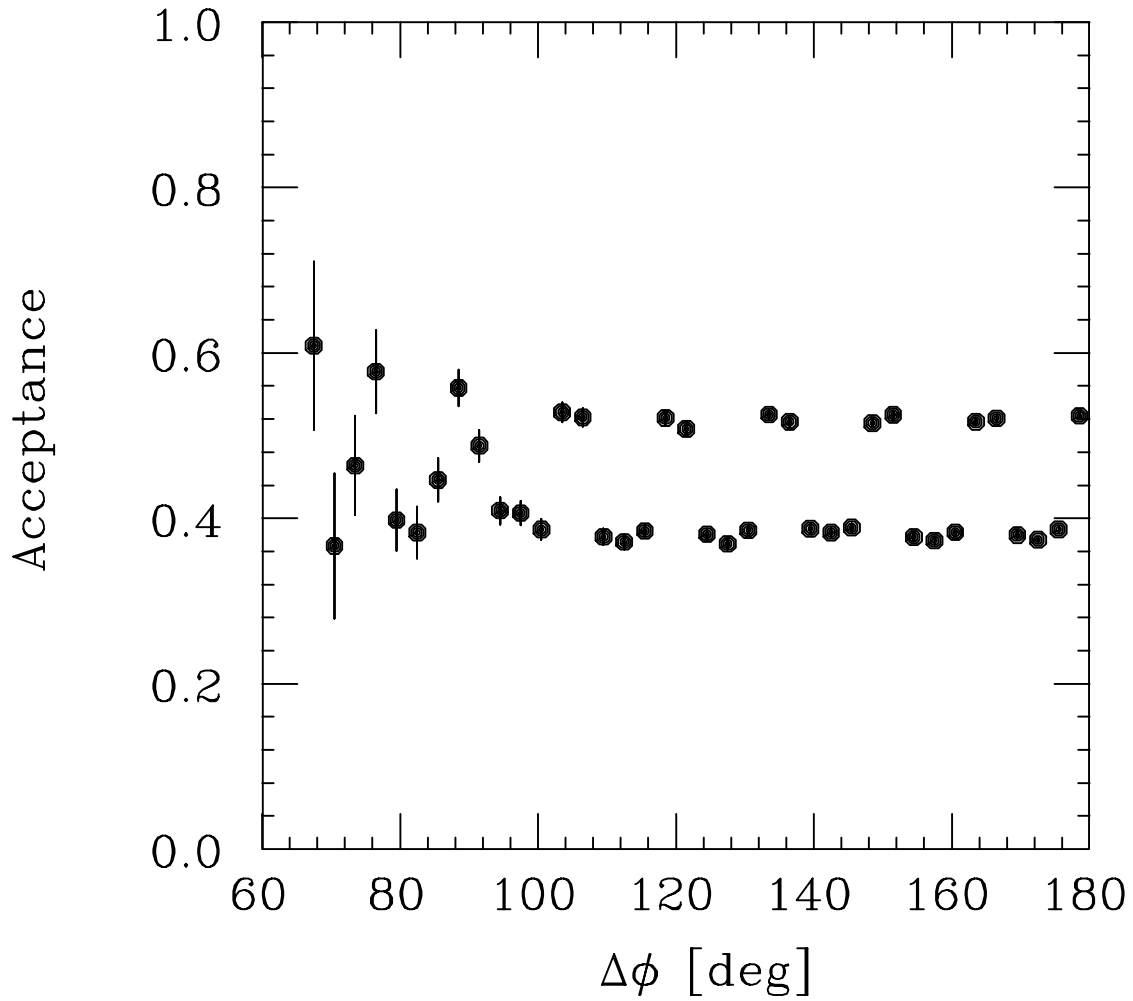


Figure 5.4: The geometrical acceptance for photons in the final diphoton data is shown as a function of the opening angle between two photons in azimuth ($\Delta\phi$). Events to estimate the acceptance are simulated by PYTHIA.

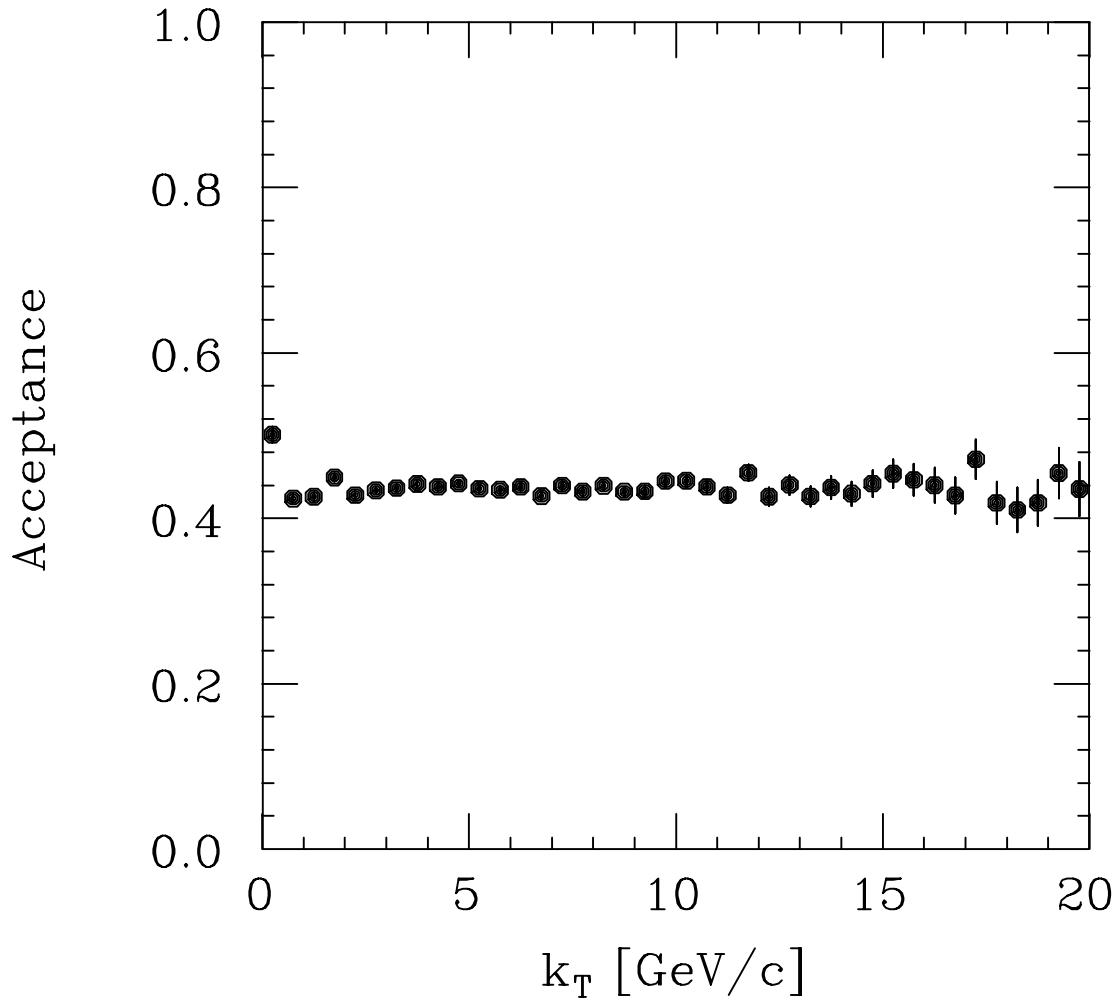


Figure 5.5: The geometrical acceptance for photons passing the final event selection is shown as a function of the transverse momentum of two-photon system (k_T). Events to estimate the acceptance are simulated by PYTHIA.

for distributions of these kinematical variables are estimated in the same way as for the p_T distribution. The acceptances are shown in Figure 5.3, 5.4, and 5.5, respectively.

5.3 Background Subtraction

The background subtraction for single prompt photon data is simply expanded to diphoton data. The background in the final diphoton data is statistically subtracted. The statistical and systematic uncertainties in the background subtraction for the final diphoton data are discussed.

5.3.1 Diphoton Identification Method

The photon identification method for single prompt photon data described in Section 4.1 is simply applied to diphoton data. Every event in a diphoton event sample can be classified into four cases by the χ_{CES}^2 cut:

- Both photon candidates fail the χ_{CES}^2 cut at 4.
- The highest p_T photon candidate fails the χ_{CES}^2 cut and the second one passes the cut.
- The highest p_T photon candidate passes the χ_{CES}^2 cut and the second one fails the cut.
- Both photon candidates pass the χ_{CES}^2 cut.

Let numbers of events classified into each case be n_{FF} , n_{FP} , n_{PF} , and n_{PP} , respectively. We define a vector n for the classification of an event in the sample as

$$n = \begin{pmatrix} n_{\text{FF}} \\ n_{\text{FP}} \\ n_{\text{PF}} \\ n_{\text{PP}} \end{pmatrix}. \quad (5.6)$$

When we consider only one event in the sample, the vector n must be one of the following four vectors:

$$n = \begin{pmatrix} 1 \\ 0 \\ 0 \\ 0 \end{pmatrix}, \begin{pmatrix} 0 \\ 1 \\ 0 \\ 0 \end{pmatrix}, \begin{pmatrix} 0 \\ 0 \\ 1 \\ 0 \end{pmatrix}, \text{ or } \begin{pmatrix} 0 \\ 0 \\ 0 \\ 1 \end{pmatrix}. \quad (5.7)$$

The event can be also classified into the following four cases:

- Both photon candidates are the background.
- The highest p_T photon candidate is the background and the second one is a true photon.
- The highest p_T photon candidate is a true photon and the second one is the background.
- Both photon candidates are true photons.

Suppose the weights of the event for each case are $w_{\pi^0\pi^0}$, $w_{\pi^0\gamma}$, $w_{\gamma\pi^0}$, and $w_{\gamma\gamma}$, respectively. Then we define a vector w for these event weights as

$$w = \begin{pmatrix} w_{\pi^0\pi^0} \\ w_{\pi^0\gamma} \\ w_{\gamma\pi^0} \\ w_{\gamma\gamma} \end{pmatrix}. \quad (5.8)$$

If we know the χ_{CES}^2 cut efficiencies for photons and the background, ϵ_γ and ϵ_{π^0} , we can express the event classification n by the event weight w and the efficiency matrix E as

$$n = Ew. \quad (5.9)$$

The efficiency matrix E is defined as

$$E = \begin{pmatrix} \bar{\epsilon}_{\pi^0(1)}\bar{\epsilon}_{\pi^0(2)} & \bar{\epsilon}_{\pi^0(1)}\bar{\epsilon}_\gamma(2) & \bar{\epsilon}_\gamma(1)\bar{\epsilon}_{\pi^0(2)} & \bar{\epsilon}_\gamma(1)\bar{\epsilon}_\gamma(2) \\ \bar{\epsilon}_{\pi^0(1)}\epsilon_{\pi^0(2)} & \bar{\epsilon}_{\pi^0(1)}\epsilon_\gamma(2) & \bar{\epsilon}_\gamma(1)\epsilon_{\pi^0(2)} & \bar{\epsilon}_\gamma(1)\epsilon_\gamma(2) \\ \epsilon_{\pi^0(1)}\bar{\epsilon}_{\pi^0(2)} & \epsilon_{\pi^0(1)}\bar{\epsilon}_\gamma(2) & \epsilon_\gamma(1)\bar{\epsilon}_{\pi^0(2)} & \epsilon_\gamma(1)\bar{\epsilon}_\gamma(2) \\ \epsilon_{\pi^0(1)}\epsilon_{\pi^0(2)} & \epsilon_{\pi^0(1)}\epsilon_\gamma(2) & \epsilon_\gamma(1)\epsilon_{\pi^0(2)} & \epsilon_\gamma(1)\epsilon_\gamma(2) \end{pmatrix} \quad (5.10)$$

where superscripts (1) and (2) indicate the first and second highest p_T photon candidates in the event, respectively. The efficiency $\bar{\epsilon}_\gamma$ is the probability that a photon fails the χ_{CES}^2 cut, and the efficiency $\bar{\epsilon}_{\pi^0}$ is the probability that the background fails the χ_{CES}^2 cut. These efficiencies can be written as

$$\bar{\epsilon}_\gamma = 1 - \epsilon_\gamma, \quad (5.11)$$

$$\bar{\epsilon}_{\pi^0} = 1 - \epsilon_{\pi^0}. \quad (5.12)$$

Therefore, we can obtain the event weight w from the event classification n and the inverse efficiency matrix $C = E^{-1}$ by

$$w = Cn. \quad (5.13)$$

For convenience, define elements of the matrix C as

$$C = \begin{pmatrix} C_{\text{FF}}^{\pi^0\pi^0} & C_{\text{FP}}^{\pi^0\pi^0} & C_{\text{PF}}^{\pi^0\pi^0} & C_{\text{PP}}^{\pi^0\pi^0} \\ C_{\text{FF}}^{\pi^0\gamma} & C_{\text{FP}}^{\pi^0\gamma} & C_{\text{PF}}^{\pi^0\gamma} & C_{\text{PP}}^{\pi^0\gamma} \\ C_{\text{FF}}^{\gamma\pi^0} & C_{\text{FP}}^{\gamma\pi^0} & C_{\text{PF}}^{\gamma\pi^0} & C_{\text{PP}}^{\gamma\pi^0} \\ C_{\text{FF}}^{\gamma\gamma} & C_{\text{FP}}^{\gamma\gamma} & C_{\text{PF}}^{\gamma\gamma} & C_{\text{PP}}^{\gamma\gamma} \end{pmatrix}. \quad (5.14)$$

Thus we can obtain the event weight for each event.

Next, we consider a diphoton sample such as a bin in a histogram filled with diphoton event candidates. Define the event classification for the sample as

$$N = \begin{pmatrix} N_{\text{FF}} \\ N_{\text{FP}} \\ N_{\text{PF}} \\ N_{\text{PP}} \end{pmatrix} = \sum n \quad (5.15)$$

where the event classification for each event, n , is summed up over all events in the sample.

The event weight for the sample is similarly written as

$$W = \begin{pmatrix} W_{\pi^0\pi^0} \\ W_{\pi^0\gamma} \\ W_{\gamma\pi^0} \\ W_{\gamma\gamma} \end{pmatrix} = \sum w = \sum Cn \quad (5.16)$$

where the inverse efficiency matrix C must be calculated event by event because the efficiencies ϵ_γ and ϵ_{π^0} depend on p_T of each photon. Finally, the true number of diphoton events in the sample, $W_{\gamma\gamma}$, can be written by using elements of the inverse efficiency matrix C . The summation of the event weights is separated into four terms of event classification as

$$W_{\gamma\gamma} = \sum w_{\gamma\gamma} = \sum_{\text{FF}} C_{\text{FF}}^{\gamma\gamma} + \sum_{\text{FP}} C_{\text{FP}}^{\gamma\gamma} + \sum_{\text{PF}} C_{\text{PF}}^{\gamma\gamma} + \sum_{\text{PP}} C_{\text{PP}}^{\gamma\gamma}. \quad (5.17)$$

The numbers of classified events and the event weights obtained from the final diphoton data are shown in Table 5.3. Photons instead of events are counted for each bin. The first error of $W_{\gamma\gamma}$ is the statistical uncertainty and the second one is the systematic uncertainty in the background subtraction. These uncertainties are described in the next section.

p_T [GeV/ c]	N_{FF}	$N_{\text{FP}} + N_{\text{PF}}$	N_{PP}	$W_{\pi^0\pi^0}$	$W_{\pi^0\gamma} + W_{\gamma\pi^0}$	$W_{\gamma\gamma}$
10 – 12	14	30	23	34	11	$22 \pm 12^{+5}_{-3}$
12 – 15	18	49	45	33	35	$44 \pm 20^{+19}_{-14}$
15 – 19	14	33	27	32	15	$27 \pm 18^{+11}_{-8}$
19 – 29	5	23	16	0	38	$6 \pm 7^{+4}_{-3}$
10 – 19	46	112	95	99	61	$93 \pm 28^{+35}_{-25}$
10 – 29	51	135	111	99	99	$99 \pm 29^{+39}_{-28}$

Table 5.3: Events in the final diphoton data set are classified by the χ_{CES}^2 cut. Numbers of photon candidates classified by the χ_{CES}^2 cut are listed for each p_T bin. Event weights are obtained in process of the background subtraction. Numbers of photons and background mesons are also listed for each p_T bin.

5.3.2 Uncertainty in the background subtraction

The true number of diphoton events, $W_{\gamma\gamma}$, can be expressed as

$$W_{\gamma\gamma} = \langle C_{\text{FF}}^{\gamma\gamma} \rangle \cdot N_{\text{FF}} + \langle C_{\text{FP}}^{\gamma\gamma} \rangle \cdot N_{\text{FP}} + \langle C_{\text{PF}}^{\gamma\gamma} \rangle \cdot N_{\text{PF}} + \langle C_{\text{PP}}^{\gamma\gamma} \rangle \cdot N_{\text{PP}} \quad (5.18)$$

where $\langle C_{pq}^{\gamma\gamma} \rangle$ is the average of the element $C_{pq}^{\gamma\gamma}$ ($pq = \text{FF}, \text{FP}, \text{PF}, \text{or PP}$) for the sample and is defined by

$$\langle C_{pq}^{\gamma\gamma} \rangle = \frac{\sum C_{pq}^{\gamma\gamma}}{N_{pq}} \quad (pq = \text{FF}, \text{FP}, \text{PF}, \text{or PP}). \quad (5.19)$$

Hence the statistical uncertainty in $W_{\gamma\gamma}$ is expressed as

$$\Delta W_{\gamma\gamma}^{\text{Statistic}} = \sqrt{\begin{aligned} & \{ \langle C_{\text{FF}}^{\gamma\gamma} \rangle \cdot \sqrt{N_{\text{FF}}} \}^2 + \{ \langle C_{\text{FP}}^{\gamma\gamma} \rangle \cdot \sqrt{N_{\text{FP}}} \}^2 \\ & + \{ \langle C_{\text{PF}}^{\gamma\gamma} \rangle \cdot \sqrt{N_{\text{PF}}} \}^2 + \{ \langle C_{\text{PP}}^{\gamma\gamma} \rangle \cdot \sqrt{N_{\text{PP}}} \}^2 \end{aligned}}. \quad (5.20)$$

To estimate the statistical uncertainty in the cross section, we take the acceptance and the event selection efficiency, $A \cdot \epsilon$, into account. The event weight is corrected for the acceptance and the event selection efficiency as

$$v = \frac{w}{A \cdot \epsilon} = \begin{pmatrix} v_{\pi^0\pi^0} \\ v_{\pi^0\gamma} \\ v_{\gamma\pi^0} \\ v_{\gamma\gamma} \end{pmatrix}. \quad (5.21)$$

Then the true number of diphoton events is corrected for the acceptance and the event selection efficiency as

$$V_{\gamma\gamma} = \sum v_{\gamma\gamma} = \sum_{\text{FF}} \frac{C_{\text{FF}}^{\gamma\gamma}}{A \cdot \epsilon} + \sum_{\text{FP}} \frac{C_{\text{FP}}^{\gamma\gamma}}{A \cdot \epsilon} + \sum_{\text{PF}} \frac{C_{\text{PF}}^{\gamma\gamma}}{A \cdot \epsilon} + \sum_{\text{PP}} \frac{C_{\text{PP}}^{\gamma\gamma}}{A \cdot \epsilon}. \quad (5.22)$$

This can be rewritten by using average coefficients as

$$V_{\gamma\gamma} = \langle \frac{C_{\text{FF}}^{\gamma\gamma}}{A \cdot \epsilon} \rangle \cdot N_{\text{FF}} + \langle \frac{C_{\text{FP}}^{\gamma\gamma}}{A \cdot \epsilon} \rangle \cdot N_{\text{FP}} + \langle \frac{C_{\text{PF}}^{\gamma\gamma}}{A \cdot \epsilon} \rangle \cdot N_{\text{PF}} + \langle \frac{C_{\text{PP}}^{\gamma\gamma}}{A \cdot \epsilon} \rangle \cdot N_{\text{PP}} \quad (5.23)$$

where the average element of the matrix C corrected for the acceptance and the event selection efficiency is defined as

$$\langle \frac{C_{pq}^{\gamma\gamma}}{A \cdot \epsilon} \rangle = \frac{\sum \frac{C_{pq}^{\gamma\gamma}}{A \cdot \epsilon}}{N_{pq}} \quad (pq = \text{FF}, \text{FP}, \text{PF}, \text{or PP}). \quad (5.24)$$

Then the statistical uncertainty in $V_{\gamma\gamma}$ can be expressed as

$$\Delta V_{\gamma\gamma}^{\text{Statistic}} = \sqrt{\begin{aligned} & \left\{ \langle \frac{C_{\text{FF}}^{\gamma\gamma}}{A \cdot \epsilon} \rangle \cdot \sqrt{N_{\text{FF}}} \right\}^2 + \left\{ \langle \frac{C_{\text{FP}}^{\gamma\gamma}}{A \cdot \epsilon} \rangle \cdot \sqrt{N_{\text{FP}}} \right\}^2 \\ & + \left\{ \langle \frac{C_{\text{PF}}^{\gamma\gamma}}{A \cdot \epsilon} \rangle \cdot \sqrt{N_{\text{PF}}} \right\}^2 + \left\{ \langle \frac{C_{\text{PP}}^{\gamma\gamma}}{A \cdot \epsilon} \rangle \cdot \sqrt{N_{\text{PP}}} \right\}^2 \end{aligned}}. \quad (5.25)$$

The statistical uncertainties $\Delta W_{\gamma\gamma}^{\text{Statistic}}$ and $\Delta V_{\gamma\gamma}^{\text{Statistic}}$ is expected to be equal to $\sqrt{W_{\gamma\gamma}}$ and $\sqrt{V_{\gamma\gamma}}$, respectively. In fact, the statistical uncertainties $\Delta W_{\gamma\gamma}^{\text{Statistic}}$ and $\Delta V_{\gamma\gamma}^{\text{Statistic}}$ are larger than expected uncertainties because the statistical uncertainties includes terms of $\sqrt{N_{\text{FF}}}$, $\sqrt{N_{\text{FP}}}$, and $\sqrt{N_{\text{PF}}}$ together with $\sqrt{N_{\text{PP}}}$. We define the equivalent number of diphoton events, N_{eq} , as

$$\frac{\Delta V_{\gamma\gamma}^{\text{Statistic}}}{V_{\gamma\gamma}} = \frac{1}{\sqrt{N_{\text{eq}}}}. \quad (5.26)$$

The statistical uncertainty in the true number of diphoton events shown in Table 5.3 is estimated as

$$\Delta W_{\gamma\gamma}^{\text{Statistic}} = \frac{W_{\gamma\gamma}}{V_{\gamma\gamma}} \cdot \Delta V_{\gamma\gamma}^{\text{Statistic}}. \quad (5.27)$$

To estimate the systematic uncertainty in the background subtraction, we change the χ_{CES}^2 cut efficiencies for photons and background by the units of systematic uncertainties described in Chapter 4. Let the number of diphoton events obtained with the mean χ_{CES}^2 cut efficiencies be $V_{\gamma\gamma}$, and let that with the χ_{CES}^2 cut efficiencies changed by the units of systematic uncertainties be $V_{\gamma\gamma}'$. Then the systematic uncertainty in the number of diphoton events is defined as

$$\Delta V_{\gamma\gamma}^{\text{Systematic}} = V_{\gamma\gamma}' - V_{\gamma\gamma}. \quad (5.28)$$

With this, the systematic uncertainty in the background subtraction shown in Table 5.3 is estimated as

$$\Delta W_{\gamma\gamma}^{\text{Systematic}} = \frac{W_{\gamma\gamma}}{V_{\gamma\gamma}} \cdot \Delta V_{\gamma\gamma}^{\text{Systematic}}. \quad (5.29)$$

Chapter 6

Results

The overall event characteristics are quite similar to W production process except for the missing E_T , as expected. The missing E_T distribution (see Figure 3.4 (c) and (d)) must show the typical characteristics which are observed in the QCD processes and is already satisfied at the early stage of event selection. In this chapter we discuss the event topology and finally the differential cross section. The result is compared with theoretical predictions and other experiments.

6.1 Event Topology

We first look into two kinematical variables of the diphoton events. The p_T ratio of the second photon to the leading photon, $z = p_T^{(2)}/p_T^{(1)}$, and the opening angle between two photons in azimuth, $\Delta\phi$, are studied.

The z distribution is shown in Figure 6.1 together with the prediction by PYTHIA 5.6 [46, 47, 48, 49], which is normalized to the data. If only the quark annihilation and the gluon fusion are taken into account, but if the parton bremsstrahlung and primordial k_T smearing are not considered, only the energy resolution of the CEM can contribute to the z distribution. When both photons have p_T 's of 10 GeV, the energy resolution gives rise to

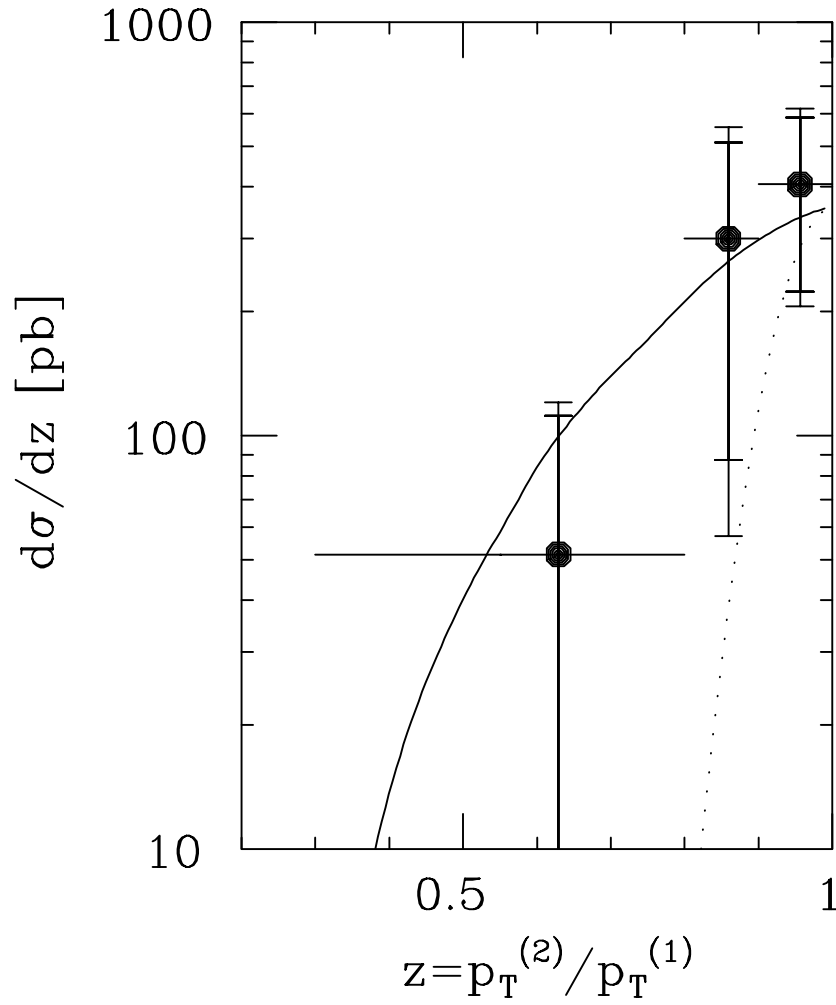


Figure 6.1: The p_T ratio of two photons, z , in the final diphoton data is shown. The PYTHIA prediction normalized to the data is shown by a solid curve. A dotted curve presents a contribution of only the energy resolution to z .

deviation of z from $z = 1$. The standard deviation σ_z is estimated as

$$\frac{\sigma_z}{z} = \sqrt{2} \times \left\{ \frac{13.5\%}{\sqrt{10} [\text{GeV}]} \oplus 2\% \right\} = 6.6\%. \quad (6.1)$$

If the z distribution contains both $z = p_T^{(2)}/p_T^{(1)}$ and $z = p_T^{(1)}/p_T^{(2)}$, the z distribution due to the energy resolution of the CEM has the mean value of $z = 1$ with the standard deviation of $\sigma_z = 7\%$ at most. The dotted line in Figure 6.1 shows this z distribution only due to the energy resolution, and is scaled to the PYTHIA prediction at $z = 1$. The z distribution due to the energy resolution is not as broad as the data, while the z distribution predicted by PYTHIA is comparable with the data.

The opening angle in azimuth, $\Delta\phi$, is shown in Figure 6.2 together with the prediction by PYTHIA, which is normalized to the data. The PYTHIA prediction is comparable with the data. The standard deviation of $\Delta\phi$ is estimated from the logical distance between wires in the CES and the radius to middle of the CES from the beam line. If the position resolution of the CES in the X direction is assumed to be about a half of the logical wire distance, the standard deviation $\sigma_{\Delta\phi}$ is calculated as

$$\sigma_{\Delta\phi} = \sqrt{2} \times \tan^{-1} \left(\frac{1.453 \text{ cm} \div 2}{183.9 \text{ cm}} \right) = 0.32^\circ. \quad (6.2)$$

This naive estimation of $\sigma_{\Delta\phi} = 0.32^\circ$ results in a very narrow $\Delta\phi$ distribution around $\Delta\phi = 180^\circ$, and is not comparable with the data.

The system of two photons in the final diphoton data has transverse momentum larger than that predicted from the detector resolution. PYTHIA simulates not only subprocesses but also the parton bremsstrahlung and the k_T smearing which can give transverse momentum to the photon pair. The initial parton bremsstrahlung add jets in a diphoton event. Number of jets which the jet clustering algorithm JETCLU [31] reconstructs in a diphoton event are summarized in Table 6.1. Two jets corresponding to both photons are removed from jets reconstructed by JETCLU. Number of jets which have corrected E_T greater than 15 GeV and come into the region of $|\eta| < 2.4$ is -0.07 ± 0.12 for the final diphoton data. The number can be compared with jet multiplicity [33] for the W data in which W 's decay into either electron or muon, because jets are selected by the same requirements for both the final diphoton data and the W data. The mean number of selected jets is 0.252 ± 0.043

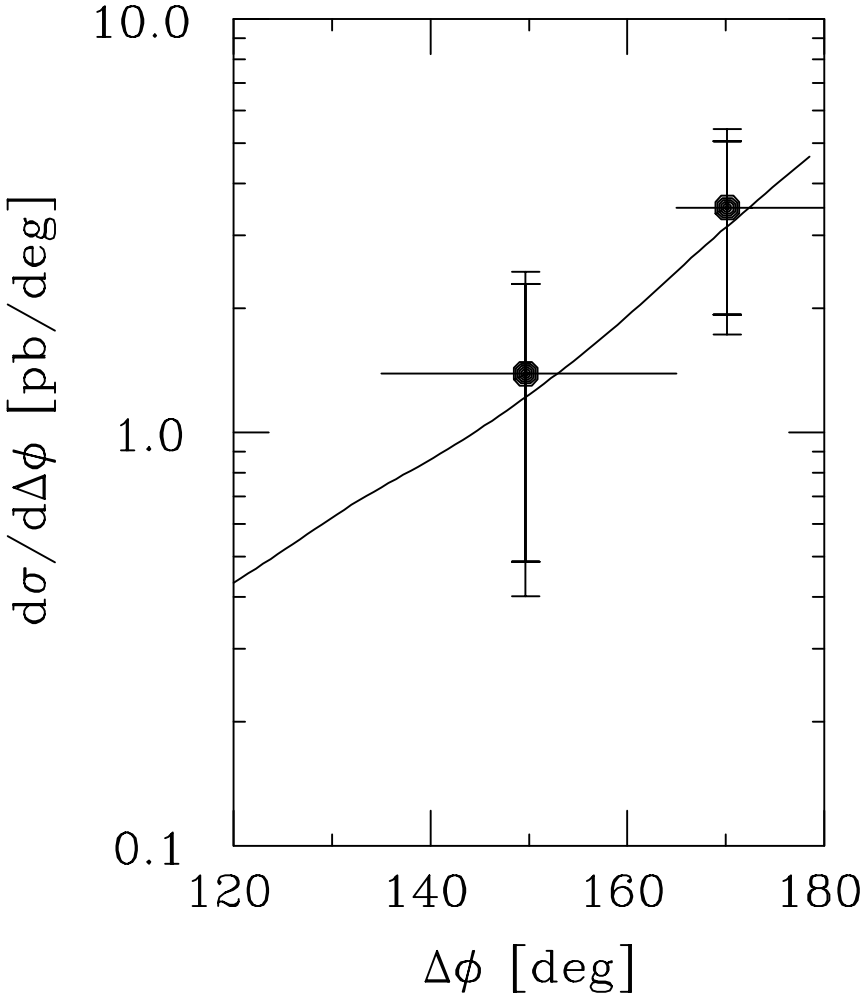


Figure 6.2: The opening angle between two photons in azimuth, $\Delta\phi$, in the final diphoton data is shown together with the PYTHIA prediction normalized to the data.

	Mean	SD	$W_{\gamma\gamma}$	$\Delta W_{\gamma\gamma}^{\text{Statistic}}$	N_{eq}
Selected jets	-0.07 ± 0.12	0.252	46.1	21.8	4.45
All jets	1.79 ± 0.60	1.55	54.5	21.0	6.73
$\Sigma E_{\text{T}}^{\text{jet}}$ [GeV]	8.1 ± 2.2	6.40	45.8	15.6	8.59

Table 6.1: Number of selected jets, number of all jets, and the scalar sum of E_{T} of jets in the final diphoton data are presented. Two jets corresponding to two photons are removed from jets reconstructed by JETCLU. The mean value with statistical uncertainty, the standard deviation, number of diphoton events with statistical uncertainty, and the equivalent number of diphoton events are shown for each.

for the W data. Both the final diphoton data and the W data have few jets with $E_{\text{T}} > 15$ GeV.

In addition, we look into all jets in the final diphoton data. Number of all jets is 1.79 ± 0.60 for the final diphoton data. The scalar sum of E_{T} of all jets found by JETCLU is 8.1 ± 2.2 GeV. Therefore, there are 1.79 ± 0.60 jets in a diphoton event, and each jet has E_{T} of 4.5 ± 1.9 GeV in average. This shows that a photon pair has a little transverse momentum and that there are a few recoil jets in the diphoton event.

The transverse momentum of a photon pair, k_{T} , is defined as

$$k_{\text{T}} = |\vec{p}_{\text{T}}^{(1)} + \vec{p}_{\text{T}}^{(2)}|. \quad (6.3)$$

The k_{T} distribution for the final diphoton data is shown in Figure 6.3 together with that for the $W \rightarrow e\nu$ data [34]. The two distributions are similar except for their absolute values. The mean p_{T} of W 's is $p_{\text{T}}^W = 5.02 \pm 0.43$ GeV/ c . The mean k_{T} for the final diphoton data is $k_{\text{T}} = 5.1 \pm 1.1$ GeV/ c , and is consistent with the mean p_{T}^W . This similarity of the kinematics between the diphoton events and the W events supports use of the border E_{T} distribution of the W sample for estimating the isolation cut efficiency, because the underlying events for the EM clusters should be also comparable with each other.

In Figure 6.4, the mean k_{T} for the final diphoton data is compared with those measured

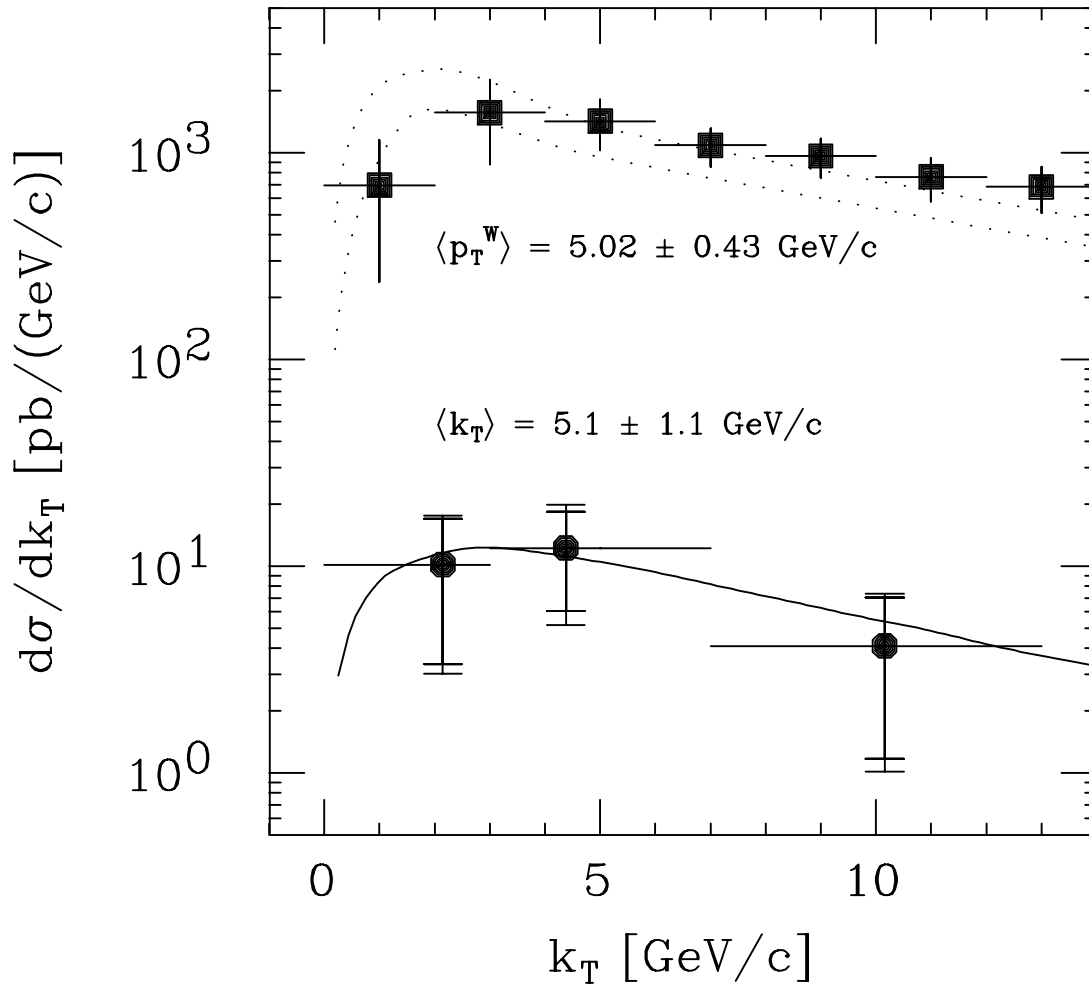


Figure 6.3: The transverse momentum of two-photon system, k_T , is shown by circles. A solid curve presents the PYTHIA prediction normalized to the data. Squares shows transverse momentum of W bosons, p_T^W , [34] and the band shown by two dotted curves are a NLL theoretical prediction [35, 36, 37]. The mean values of k_T and p_T^W are also given.

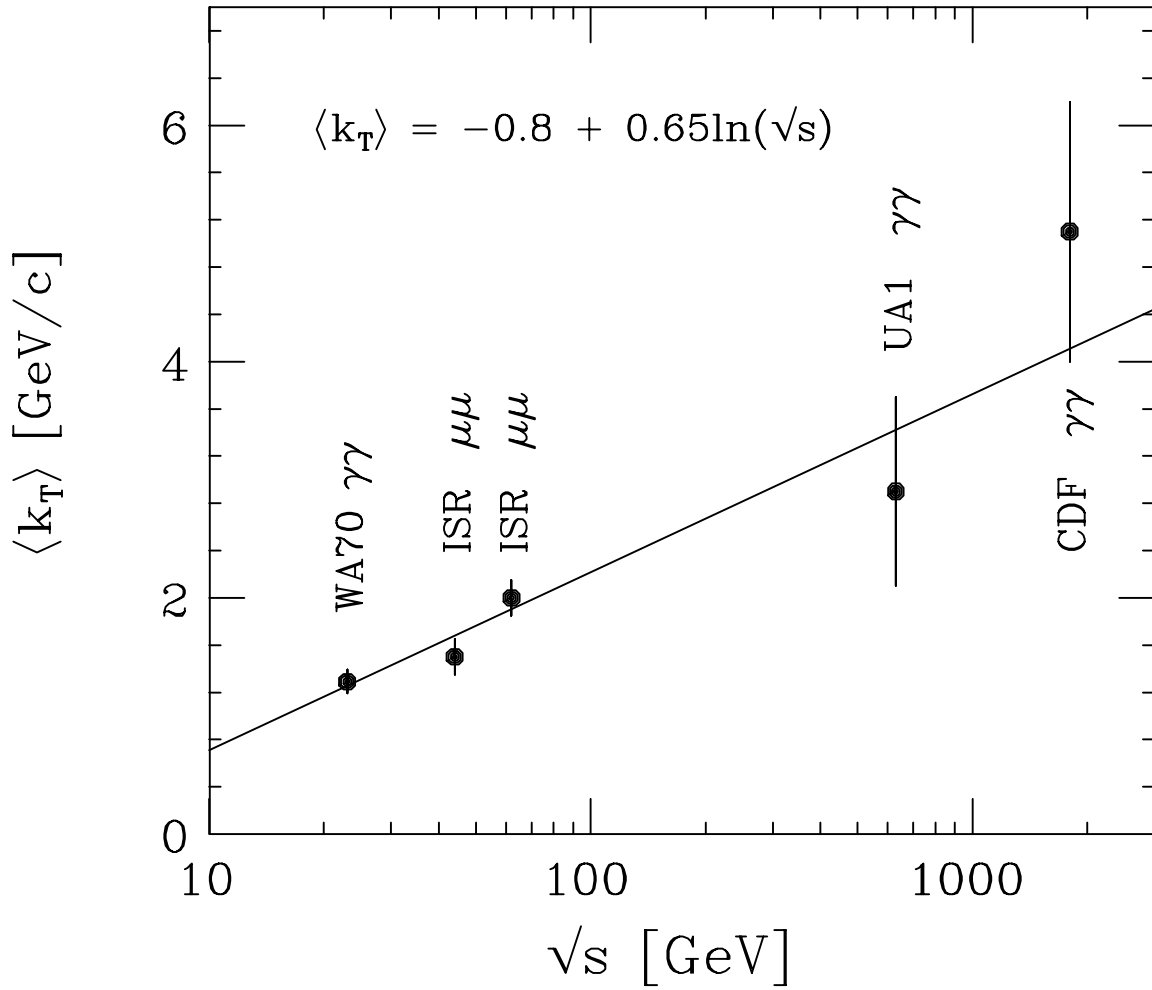


Figure 6.4: The mean k_T 's measured in several experiments are compared with our measurement. These data points are roughly proportional to $\ln(s)$. The solid line is a straight line fitted to these points.

in other experiments. WA70 measured $\langle k_T \rangle$ for diphoton events at $\sqrt{s} = 22.9$ GeV [5]. The means p_T of muon pairs are measured by D.Antreasyan *et al.* at $\sqrt{s} = 62$ and 44 GeV in CERN ISR [38]. UA1 reported six candidates of the diphoton production at $\sqrt{s} = 630$ GeV, in which 0.9 ± 0.45 event of the background was expected [6]. We calculated the mean k_T from the table presenting the event kinematics by assuming equal weights for the six events. The mean value is also shown. The mean k_T is roughly proportional to $\ln(s)$ as shown in Figure 6.4.

6.2 Cross Section

We have 152 events in the final diphoton data set. The background due to neutral mesons still remains in the data, and can be statistically subtracted by using the difference in the χ_{CES}^2 cut efficiency for photons and the background as described in Chapter 5. The background subtraction gives a weight as a diphoton event, $w_{\gamma\gamma}$, to every event in the final diphoton data set. We can obtain the differential cross section as a function of a kinematical variable X from the integrated luminosity $\int \mathcal{L} dt$, the event weights $w_{\gamma\gamma}$, the acceptance A , and the event selection efficiency ϵ as follows:

$$\frac{d\sigma}{dX} = \frac{V_{\gamma\gamma}}{\int \mathcal{L} dt \cdot \Delta X} = \frac{\sum \frac{w_{\gamma\gamma}}{A \cdot \epsilon}}{\int \mathcal{L} dt \cdot \Delta X}. \quad (6.4)$$

The event weights corrected for the acceptance and the event selection efficiencies are summed over all events in the range between X and $X + \Delta X$. Detailed discussion on the luminosity are given in Appendix C. The event selection efficiency is a product of the trigger efficiencies, $\epsilon_{\text{L2T}}^{(1)}$ and $\epsilon_{\text{L2T}}^{(2)}$, the isolation cut efficiencies, $\epsilon_{\text{ISO}}^{(1)}$ and $\epsilon_{\text{ISO}}^{(2)}$, and the selection efficiency for the CES clusters, $\epsilon_{\text{CES}}^{(1)}$ and $\epsilon_{\text{CES}}^{(2)}$, and is written as

$$\epsilon = \epsilon_{\text{CES}}^{(1)} \cdot \epsilon_{\text{CES}}^{(2)} \cdot \epsilon_{\text{ISO}}^{(1)} \cdot \epsilon_{\text{ISO}}^{(2)} \cdot \epsilon_{\text{L2T}}^{(1)} \cdot \epsilon_{\text{L2T}}^{(2)} \quad (6.5)$$

where superscripts (1) and (2) indicate the highest- p_T photon and the second photon.

Uncertainties in efficiencies of the level-2 trigger, the isolation cut, and the χ_{CES}^2 cut are taken account into the systematic uncertainty of the cross section. The uncertainty in

p_T [GeV/c]	$\langle p_T \rangle$ [GeV/c]	$d\sigma/dp_T$ [pb/(GeV/c)]	Uncertainty [%]	
			Statistical	Systematic
10 – 12	11.1	17.5	57	+31 –21
12 – 15	13.5	11.6	46	+45 –35
15 – 19	17.4	4.2	65	+41 –29
19 – 29	27.3	0.9	109	+64 –46
10 – 19	13.3	9.6	31	+37 –27
10 – 29	14.6	5.0	30	+40 –29

Table 6.2: The diphoton differential cross section is summarized together with the p_T bin size, the mean p_T in each bin, the statistical and systematic uncertainties.

the level-2 trigger efficiency comes from the statistics of the Drell-Yan sample from which the trigger efficiency is estimated. The uncertainty in the event selection is mainly that in the isolation cut efficiency. For the uncertainty in the isolation cut efficiency, the value of correction $\pm(1 - \epsilon_{\text{ISO}})$ is taken because the underlying event in W events instead of diphoton events is used to estimate the efficiency. The systematic uncertainty in the χ_{CES}^2 cut efficiencies for photons and the background comes from the difference in the shower fluctuation and the shower shape between photons and electrons, and from the saturation of the CES gas gain. Also the systematic uncertainty in the background efficiency includes the uncertainty in the composition of neutral mesons π^0 , η , and K_S^0 .

The p_T distribution of photons in the final diphoton data is shown in Figure 6.5 together with several theoretical curves. Both photons in each event are taken into account, so that the cross section multiplied by integrated luminosity, $\sigma \cdot \int \mathcal{L} dt$, gives number of photons instead of number of events. Inner error bars in Figure 6.5 are statistical uncertainties, and outer ones are total uncertainties in which both statistical and systematic uncertainties are combined in quadrature independently for either upper or lower side. The differential cross section, the mean p_T , statistical and systematic uncertainties for each p_T bin are listed in Table 6.2. The cross section of photons with p_T in the range of $10 < p_T < 29$ [GeV/c] is

$95 \pm 28(\text{stat})_{-27}^{+38}(\text{syst}) \text{ pb}$.

The lowest-order (LO) calculation which consists of the quark annihilation ($q\bar{q} \rightarrow \gamma\gamma$) and the gluon fusion ($gg \rightarrow \gamma\gamma$) is shown by a dotted curve and is compared with the data in Figure 6.5. The differential cross section is integrated over the η ranges of $|\eta| < 0.9$ for both photons. The calculation involves a parton distribution in a nucleon, which is referred to as EHLQ set 1 [39], and takes account of four flavors in a quark loop. The following definition of the factorization scale Q^2 is used for the calculation.

$$Q^2 = p_T^2 \tag{6.6}$$

where p_T is transverse momentum of either photon ($p_T = p_T^{(1)} = p_T^{(2)}$). Since the initial parton bremsstrahlung and the primordial k_T smearing are not taken into account, p_T 's of the two photons are equal. The solid curve presents the LO calculation including the higher-order QCD correction which multiply each lowest-order subprocess by an approximate K factors [51] described in Appendix A. Both predictions are lower than the data.

UA2 measured the differential cross section for diphoton production over the range of $10 < p_T < 30$ [GeV/c] at $\sqrt{s} = 630$ GeV [7]. The UA2 data is also shown in Figure 6.5. Since the UA2 data is limited to $|\eta| < 0.76$, it is corrected to the range of $|\eta| < 0.9$ by simply multiplying by an overall correction factor in order to compare with the CDF data. The overall correction factor for the η coverage is the ratio of the cross section calculated with $|\eta| < 0.9$ to that calculated with $|\eta| < 0.76$. Both cross sections are calculated by the LO calculation at $\sqrt{s} = 630$ GeV, are integrated over the range of $10 < p_T < 30$ [GeV/c]. The LO prediction for the UA2 data corrected to the CDF coverage is shown by a dashed curve. The LO prediction at the CDF energy is about twice as large as that at the UA2 energy, whereas the rise of the cross section in the data is larger than that predicted by the LO calculation.

More three types of theoretical prediction are compared with the CDF data in Figure 6.6.

- A prediction by PYTHIA is compared with the data. This calculation by PYTHIA includes both the quark annihilation and the gluon fusion, and involves the parton

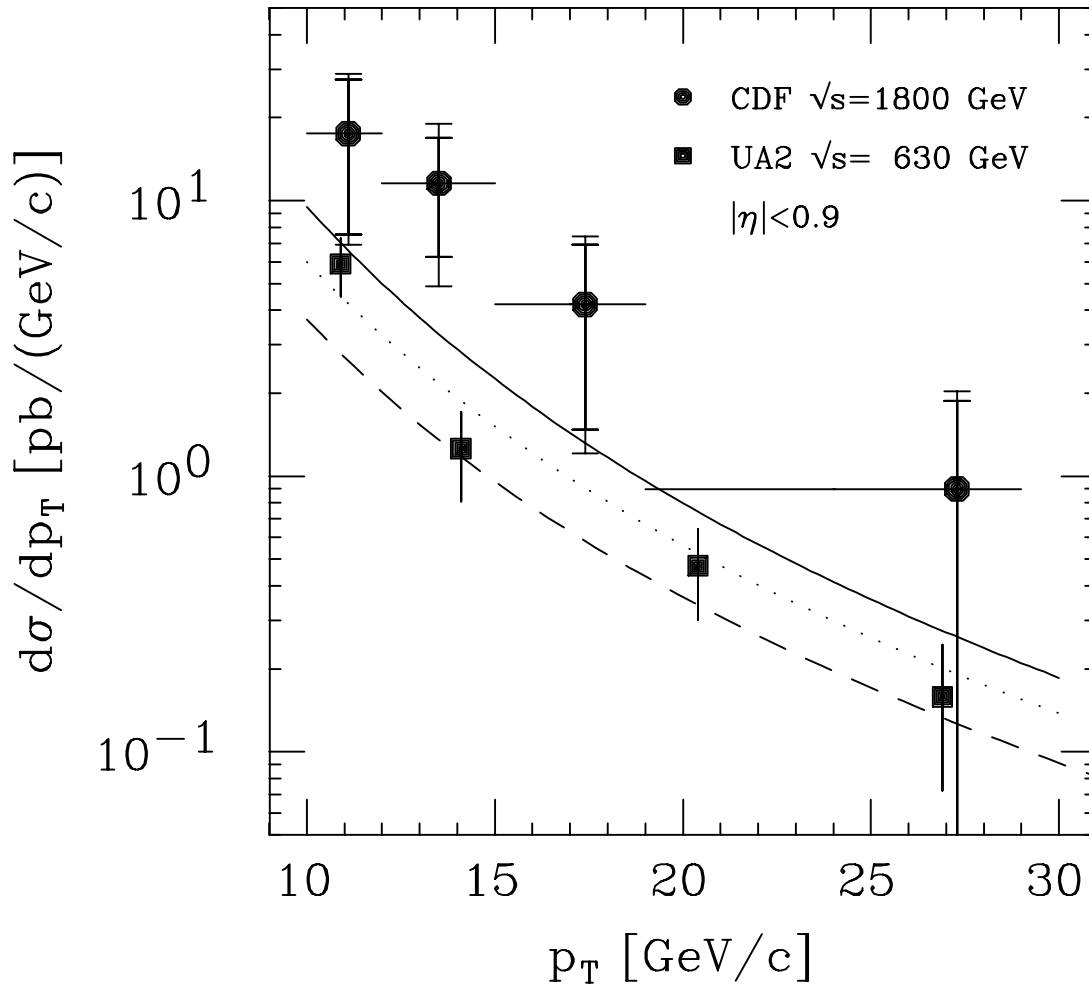


Figure 6.5: The diphoton differential cross section with respect to p_T is shown by circles. The UA2 data [7] shown by squares is compared with our measurement. Two theoretical prediction is also compared with our measurement: A dotted curve is the LO prediction, and a solid curve is the LO calculation corrected with K factors. A dashed curve is the LO prediction for the UA2 data.

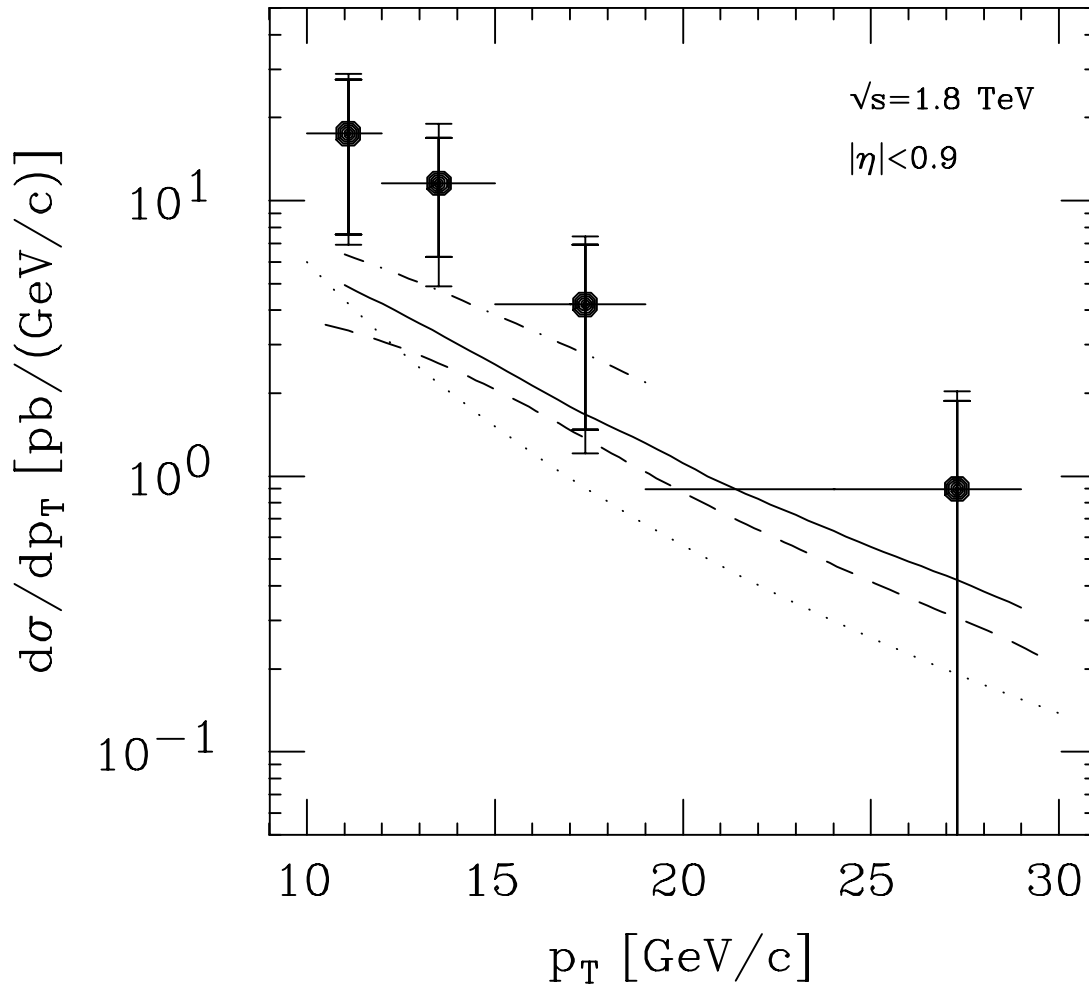


Figure 6.6: The diphoton differential cross section with respect to p_T is compared with four theoretical predictions: A dotted curve is the LO calculation, a dashed curve is the PYTHIA prediction, a dot-dashed curve is the PYTHIA prediction including bremsstrahlung, and a solid curve is the NLL calculation.

Cross section [pb]	
LO calculation	20
LO corrected with K Factors	30
PYTHIA	21
PYTHIA with Bremsstrahlung	38
NLL calculation	27
CDF data	$86 \pm 27 \begin{smallmatrix} +32 \\ -23 \end{smallmatrix}$

Table 6.3: Several theoretical predictions of the diphoton cross section are compared with the data. The cross sections are integrated over $|\eta| < 0.9$ for both photons, $10 < p_T^{(1)} < 35$ [GeV/ c] for the highest- p_T photon, and $10 < p_T^{(2)} < 19$ [GeV/ c] for the second photon.

distribution of EHLQ set 1 with the following definition of the factorization scale.

$$Q^2 = \frac{\hat{t}\hat{u}}{\hat{s}} = \frac{1}{2} \left((p_T^{(1)})^2 + (p_T^{(2)})^2 \right). \quad (6.7)$$

PYTHIA includes the initial parton bremsstrahlung and the primordial k_T smearing. The differential cross section is integrated over the η range of $|\eta| < 0.9$. The kinematical cut ($10 < p_T < 35$ [GeV/ c]) are applied to both photons. This prediction is shown by a dashed curve.

- Another prediction by PYTHIA is also shown by a dot-dashed curve. This calculation includes the single photon production with a bremsstrahlung photon from the away-side jet as well as the quark annihilation and the gluon fusion. A parton distribution called HMRS B-190 [42] is employed with the following Q^2 definition.

$$Q^2 = \hat{s}. \quad (6.8)$$

The large momentum transfer Q^2 for calculating the strong coupling α_S is transformed as $Q^2 \rightarrow \frac{1}{4}Q^2$. The differential cross section is integrated over the central η coverage ($|\eta| < 0.9$). The kinematical cut ($10 < p_T < 35$ [GeV/ c]) and the isolation cut ($I_{\text{Border}} < 0.1$) are applied to both photons.

- The next-to-leading logarithmic (NLL) QCD calculation [52] is compared with the data. This NLL prediction is presented by a solid curve. The differential cross section is integrated over the central η coverage ($|\eta| < 0.9$). The kinematical cut ($10 < p_T < 35$ [GeV/ c]) and the isolation cut ($I_{\text{Border}} < 0.1$) are applied to both photons.

Those theoretical predictions for the diphoton cross section are summarized in Table 6.3, and are numerically compared with the CDF data. The cross sections in Table 6.3 are integrated over $|\eta| < 0.9$ for both photons, $10 < p_T^{(1)} < 35$ for the highest- p_T photon, and $10 < p_T^{(2)} < 19$ for the second highest- p_T photon. The PYTHIA predictions including bremsstrahlung and the NLL calculation are comparable with the data. Those theoretical predictions, however, are all lower than the data.

Chapter 7

Conclusion

We took data of integrated luminosity $\int \mathcal{L} dt = 4.3 \text{ pb}^{-1}$ for diphoton events in proton-antiproton collisions at $\sqrt{s} = 1.8 \text{ TeV}$ during the 1988–1989 collider run. The missing E_T significance in the data is consistent with the overall energy resolution of the CDF calorimetry. Therefore the data is dominated by ordinary QCD subprocesses. After event selection, we obtain 152 events of diphoton in the central region ($|\eta| < 0.9$). The background subtraction using the lateral shower profile in the CES is applied to the data. Finally we obtained $49 \pm 15(\text{stat}) \text{ }^{+20}_{-14}(\text{syst})$ events of the diphoton production in the range of $10 < p_T < 29 \text{ [GeV}/c]$. The cross section is $95 \pm 28(\text{stat}) \text{ }^{+38}_{-27}(\text{syst}) \text{ pb}$. The diphoton events exhibit parallels to W boson production in many regards; the degree of isolation of electrons from W decays and that of photons, the number of jets produced in association, and recoil momentum against the associating jets. The only difference is in the cross section, which is approximately 100 times larger than the W production. Another important observation is that the diphoton production process is totally comparable with the QCD calculation, except for the numerical discrepancy in the cross section. The measured cross section is from 2 to 3 times larger than any calculation which we compared with the data. This is an interesting question from the theoretical stand point of view, but no obvious explanation for the difference is yet found. The shape of the differential cross section is well reproduced by the QCD calculation, and we observed no anomalies or deviations from QCD.

Appendix A

Diphoton Production Cross Section

In this appendix, calculations of the cross section of the diphoton production are described. Those calculations are shown in Figure 1.1, 6.5, and 6.6. First, the kinematics in a two-body scattering ($ab \rightarrow cd$) and a general formulation of the differential cross section are presented. The initial parton bremsstrahlung and the primordial k_T smearing are not considered, where the primordial k_T is transverse momentum of two initial partons. Integrated the general formulation, we can obtain a formula of the differential cross section with respect to the transverse momentum. The differential cross sections for subprocesses of the diphoton production are last presented.

Let us consider the reaction of a parton a inside a beam hadron A and a parton b inside a target hadron B , where particles c and d are scattered off in the final state. When the initial partons a and b and the final partons c and d have four-momenta, p_a , p_b , p_c , and p_d , respectively, the Mandelstam variables are defined as:

$$\hat{s} = (p_a + p_b)^2, \quad (\text{A.1})$$

$$\hat{t} = (p_a - p_c)^2, \quad (\text{A.2})$$

$$\hat{u} = (p_b - p_c)^2. \quad (\text{A.3})$$

A caret symbol $\hat{}$ will be placed over variables with regard to a subprocess. The Mandelstam variables are Lorentz invariant. The conservation of energy and momentum, $p_a + p_b = p_c + p_d$, can be expressed as $\hat{s} + \hat{t} + \hat{u} = m_a^2 + m_b^2 + m_c^2 + m_d^2$, where m denotes mass of each particle. In

high-energy processes we can neglect quark masses. Suppose that parton a carries a fraction x_a of the momentum of hadron A and parton b carries a momentum fraction of x_b of hadron B in the rest frame of the hadron-hadron reaction. If we can neglect masses and transverse momenta of initial partons, the four-momenta of partons a and b can be written by

$$p_a = x_a \frac{\sqrt{s}}{2} (1, 0, 0, +1) \quad (\text{A.4})$$

$$p_b = x_b \frac{\sqrt{s}}{2} (1, 0, 0, -1) \quad (\text{A.5})$$

where \sqrt{s} is the center-of-mass energy.

The cross section of the hadron-hadron reaction involving a large momentum transfer can be factorized into the parton distribution function, the fragmentation function, and a hard-scattering subprocess according to the prescription provided by the parton model. Thus the invariant cross section of the hadron-hadron reaction $AB \rightarrow cd$ is written as

$$\begin{aligned} d\sigma(AB \rightarrow cd) &= \frac{1}{2s} \sum_{ab} G_{a/A}(x_a) dx_a G_{b/B}(x_b) dx_b \\ &\quad \sum |\mathcal{M}(ab \rightarrow cd)|^2 (2\pi)^4 \delta^4(p_a + p_b - p_c - p_d) \frac{d^3 p_c}{(2\pi)^3 2E_c} \frac{d^3 p_d}{(2\pi)^3 2E_d}, \end{aligned} \quad (\text{A.6})$$

where $G_{a/A}(x_a) dx_a$ is the probability of finding a parton a in a hadron A with a momentum fraction between x_a and $x_a + dx_a$ and similarly $G_{b/B}(x_b) dx_b$ for a parton b . The invariant amplitude squared of the hard scattering subprocess, $|\mathcal{M}(ab \rightarrow cd)|^2$, can be perturbatively calculated as long as it takes place involving a large momentum transfer. In this formulation, $2s$ is referred to as the initial flux in the center-of-mass frame and

$$d\text{Lips} = (2\pi)^4 \delta^4(p_a + p_b - p_c - p_d) \frac{d^3 p_c}{(2\pi)^3 2E_c} \frac{d^3 p_d}{(2\pi)^3 2E_d}, \quad (\text{A.7})$$

is called the Lorentz invariant phase space factor.

If we use the transverse and longitudinal momentum, p_T and p_z , for an outgoing particles, the rapidity y is defined as

$$y = \frac{1}{2} \ln \frac{E + p_z}{E - p_z}. \quad (\text{A.8})$$

When particles c and d have rapidities y_1 and y_2 , respectively, the four-momenta for outgoing particles c and d can be written by

$$p_c = p_T (\cosh y_1, +1, 0, \sinh y_1) \quad (\text{A.9})$$

$$p_d = p_T(\cosh y_2, -1, 0, \sinh y_2). \quad (\text{A.10})$$

Integration of the invariant cross section over the phase space of the final state gives

$$\frac{d\sigma}{dy_1 dy_2 dp_T^2}(AB \rightarrow cd) = \sum_{ab} x_a G_{a/A}(x_a) x_b G_{b/B}(x_b) \frac{d\hat{\sigma}}{d\hat{t}}(ab \rightarrow cd) \quad (\text{A.11})$$

where the differential cross section for the two-body parton scattering subprocess is denoted by

$$\frac{d\hat{\sigma}}{d\hat{t}}(ab \rightarrow cd) = \frac{1}{16\pi\hat{s}^2} \sum |\mathcal{M}(ab \rightarrow cd)|^2. \quad (\text{A.12})$$

The momentum fractions of incoming partons are constrained by the observed final state as follows:

$$x_a = \frac{p_T}{\sqrt{s}}(e^{y_1} + e^{y_2}), \quad (\text{A.13})$$

$$x_b = \frac{p_T}{\sqrt{s}}(e^{-y_1} + e^{-y_2}). \quad (\text{A.14})$$

In addition, the invariant mass M is defined as

$$M^2 = 2p_T^2(1 + \cosh(y_1 - y_2)) \quad (\text{A.15})$$

and the invariant mass distribution is written down as

$$\frac{d\sigma}{dy_1 dy_2 dM} = \frac{M}{1 + \cosh(y_1 - y_2)} \frac{d\sigma}{dy_1 dy_2 dp_T^2}. \quad (\text{A.16})$$

If we can measure transverse momenta and rapidities of the final partons and know the parton distribution well, we can study the hard-scattering subprocess. Furthermore, if we can measure transverse momenta and rapidities of the final partons and can specify the hard-scattering subprocess $ab \rightarrow cd$ occurring under the hadron-hadron reaction $AB \rightarrow cd$, we can measure the parton distributions $G_{a/A}(x_a)$ and $G_{b/B}(x_b)$.

The lowest-order (LO) subprocess of the diphoton production is the quark annihilation ($q\bar{q} \rightarrow \gamma\gamma$) which includes two electromagnetic vertices shown in Figure 1.1. The Feynman diagram for the quark annihilation is presented in Figure A.1 (a). The differential cross section of this subprocess, which is proportional to α^2 , is written as

$$\frac{d\sigma}{d\hat{t}}(q\bar{q} \rightarrow \gamma\gamma) = \pi\alpha^2 e_q^4 \frac{1}{3} \frac{2}{\hat{s}^2} \left(\frac{\hat{u}}{\hat{t}} + \frac{\hat{t}}{\hat{u}} \right) \quad (\text{A.17})$$

e_q is electric charge of a quark which takes part in the reaction. Another lowest-order subprocess is the gluon fusion ($gg \rightarrow \gamma\gamma$) [50] which includes a quark loop as shown in Figure A.1 (b). The differential cross section, which is proportional to $\alpha^2\alpha_S^2$, is written as

$$\frac{d\sigma}{dt}(gg \rightarrow \gamma\gamma) = \alpha^2 \left(\sum_{i=1}^{N_f} e_q^2 \right)^2 \alpha_S^2 \frac{1}{8\pi\hat{s}^2} \{ |A(w)|^2 + |B(w)|^2 + |B(1-w)|^2 + 5 \} \quad (\text{A.18})$$

where N_f is number of flavors which is involved in the quark loop. $A(w)$, $B(w)$, and w are defined as:

$$A(w) = 1 + (2w - 1) \ln \frac{1-w}{w} + \frac{1}{2} (w^2 + (1-w)^2) \left(\ln^2 \frac{1-w}{w} + \pi^2 \right), \quad (\text{A.19})$$

$$B(w) = 1 - \left(1 - \frac{2}{w} \right) (\ln(1-w) + i\pi) + \frac{1}{2w^2} (1 + (1-w)^2), \ln(1-w)(\ln(1-w) + i2\pi) \quad (\text{A.20})$$

and

$$w = -\frac{\hat{u}}{\hat{s}}. \quad (\text{A.21})$$

For next-to-leading logarithmic (NLL) corrections to the Born terms, approximate K factors [51] are calculated by Contogouris *et al.* The approximate K factors are of the form

$$K = 1 + \frac{\alpha_S}{2\pi} C \pi^2 \quad (\text{A.22})$$

where C is a color factor. For the quark annihilation, a color factor C is given as

$$C(q\bar{q} \rightarrow \gamma\gamma) = C_F = \frac{4}{3} \quad (\text{A.23})$$

where C_F is the color factor in the color SU(3). For the gluon fusion, a color factor C is given as

$$C(gg \rightarrow \gamma\gamma) = N_c = 3 \quad (\text{A.24})$$

where N_c is number of colors in the color SU(3).

Aurenche *et al.* has carried a complete calculation of next-to-leading logarithmic corrections for the quark annihilation ($q\bar{q} \rightarrow \gamma\gamma$) and the bremsstrahlung ($qg \rightarrow q\gamma\gamma$ and $q\bar{q} \rightarrow g\gamma\gamma$), which is called the beyond leading logarithmic (BLL) QCD calculation. This

BLL calculation includes the full integration over the phase space for the opposite-side photon in the diphoton production. Because of difference in the η range, we can not compare this BLL calculation with our data.

Whereas Owens *et al.* presented the NLL calculation using a Monte Carlo integration method [52]. The Monte Carlo calculation can be adapted to our experimental conditions. Furthermore, the Monte Carlo calculation allows us to study the NLL corrections for several observables. A result of the NLL corrections using the Monte Carlo calculation is shown in Figure 6.6.

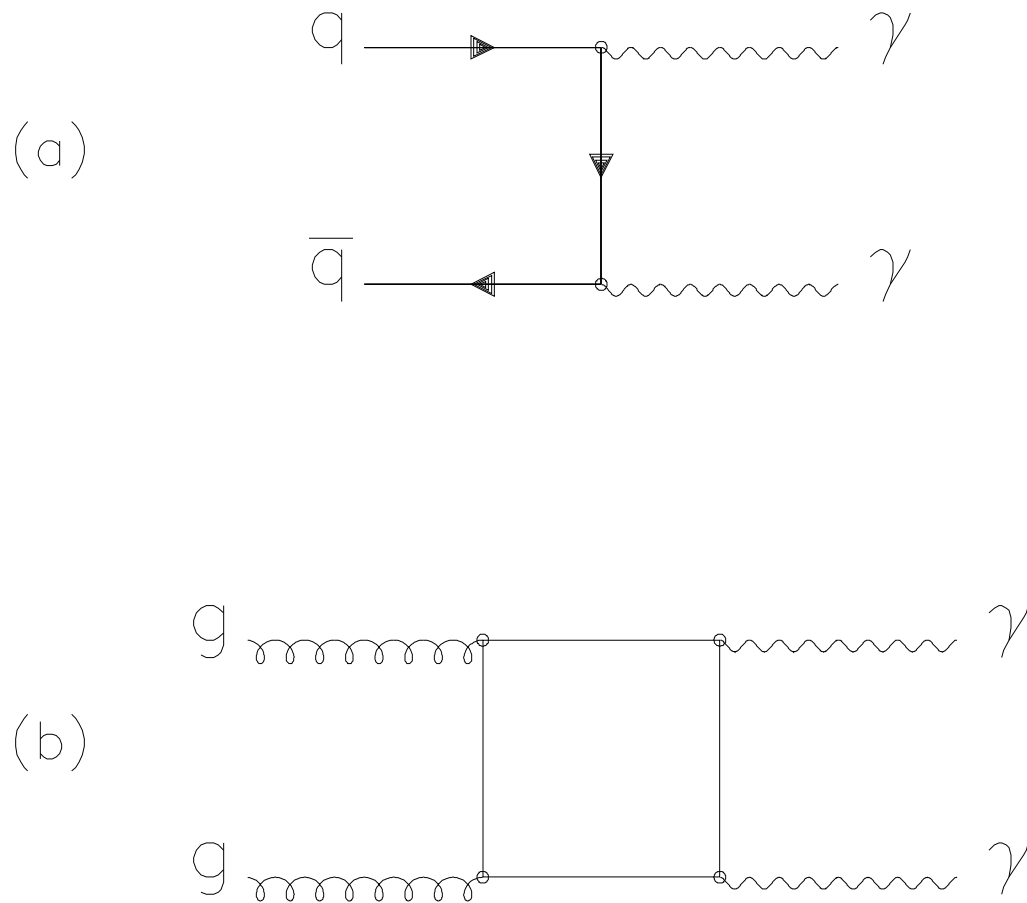


Figure A.1: Feynman diagrams for the diphoton production are shown: (a) The quark annihilation ($q\bar{q} \rightarrow \gamma\gamma$), (b) the gluon fusion ($gg \rightarrow \gamma\gamma$).

Appendix B

Missing Transverse Energy Significance

In ordinary QCD processes, there is not either high- p_T neutrino or high- p_T muon whose energy can not be directly measured with a calorimeter. There may be neutrinos and muons from hadron decays, but these momenta should be statistically balanced in the azimuth. Therefore, the vector sum of energy deposits in calorimeter towers should be centered around zero in the X - Y plane. We often use the missing E_T significance rather than the missing E_T itself to distinguish a kind of strange events, such as cosmic ray backgrounds, from ordinary events. The distribution of the missing E_T significance is described below.

We define projections of missing transverse energy \cancel{E}_T onto X and Y axis:

$$\cancel{E}_X = - \sum_j E_j \sin \theta_j \cdot \cos \phi_j, \quad (\text{B.1})$$

$$\cancel{E}_Y = - \sum_j E_j \sin \theta_j \cdot \sin \phi_j. \quad (\text{B.2})$$

E_j is the total energy deposit in the j -th tower. θ_j and ϕ_j are the polar and azimuthal angles of the tower center when the origin of the coordinate system is put at the event vertex. The magnitude of the missing E_T is define as

$$\cancel{E}_T = \sqrt{\cancel{E}_X^2 + \cancel{E}_Y^2}. \quad (\text{B.3})$$

The missing E_T significance S is defined as

$$S = \frac{\cancel{E}_T}{\sqrt{\Sigma E_T}} \quad (\text{B.4})$$

where ΣE_T is the total E_T sum. The total E_T sum is defined as

$$\Sigma E_T = \sum_j E_j \sin \theta_j. \quad (\text{B.5})$$

We can also define projections of S onto X or Y axis as:

$$S_X = \frac{\cancel{E}_X}{\sqrt{\Sigma E_T}}, \quad (\text{B.6})$$

$$S_Y = \frac{\cancel{E}_Y}{\sqrt{\Sigma E_T}}. \quad (\text{B.7})$$

Let's consider a calorimeter with total number of towers n . Simply suppose that each tower always measures the average transverse energy E with the standard deviation $\sigma(E)$. Then we can expect means of both \cancel{E}_X and \cancel{E}_Y are zero. Furthermore, we can estimate the standard deviations of \cancel{E}_X and \cancel{E}_Y , $\sigma(\cancel{E}_X)$ and $\sigma(\cancel{E}_Y)$, as follows:

$$\sigma(\cancel{E}_X) \sim \sigma(\cancel{E}_Y) \sim \sqrt{\sum_j \sigma(E)^2 \cos^2 \phi_j} = \sqrt{\frac{n}{2}} \cdot \sigma(E). \quad (\text{B.8})$$

We can also estimate the total E_T sum ΣE_T as

$$\Sigma E_T \sim \sum_j E = n \cdot E. \quad (\text{B.9})$$

In this simple case, the standard deviations of projection of the missing E_T significance, $\sigma(S_X)$ and $\sigma(S_Y)$, correspond to a coefficient of the stochastic part in a formulation of energy resolution of the calorimeter.

$$\sigma(S_X) \sim \sigma(S_Y) \sim \frac{1}{\sqrt{2}} \cdot \frac{\sigma(E)}{\sqrt{E}} \equiv \bar{\sigma}. \quad (\text{B.10})$$

Therefore we can regard both S_X and S_Y as a Gaussian distribution with the standard deviation $\bar{\sigma}$ as

$$g(x) = \frac{1}{\sqrt{2\pi}\bar{\sigma}} \exp\left[-\frac{x^2}{2\bar{\sigma}^2}\right]. \quad (\text{B.11})$$

Thus we can expect a bi-Gaussian for the missing E_T significance. We estimate the distribution of the missing E_T significance on the basis of hypothesis as follows:

$$f(S) = \iint g(S_X)g(S_Y) \delta(S - \sqrt{S_X^2 + S_Y^2}) dS_X dS_Y = \frac{S}{\bar{\sigma}^2} \exp\left[-\frac{S^2}{2\bar{\sigma}^2}\right]. \quad (\text{B.12})$$

From this simple discussion, we expect that \cancel{E}_X and \cancel{E}_Y in our data have a standard deviation $\bar{\sigma}$ corresponding to the overall energy resolution. Furthermore, we expect that a bi-Gaussian with the standard deviation $\bar{\sigma}$ is fitted to the missing E_T significance in our data. Figure 3.4 (a) and (b) show \cancel{E}_X and \cancel{E}_Y in the diphoton data, to which a Gaussian with a common standard deviation is fitted well. Figure 3.4 (c) shows the missing E_T significance in the data, which the bi-Gaussian with the standard deviation fits. The missing E_T significance in the final diphoton data shown in Figure 3.4 (d) also displays a bi-Gaussian form. Therefore, our data are consistent with ordinary QCD events.

Appendix C

Luminosity Calculation

The number of events, \mathcal{N} , which we observed is given by

$$\mathcal{N} = \sigma \cdot \int \mathcal{L} dt \quad (\text{C.1})$$

where σ denotes the cross section of a hadron-hadron reaction and $\int \mathcal{L} dt$ denotes the integrated luminosity. Thus we must know the luminosity \mathcal{L} to measure the cross section. The luminosity calculation is explained below.

Suppose a beam which consists of particles with the mass m , the momentum P , and the energy E , goes along the z axis. We consider motion of the beam in the x direction. The two variables of Hamiltonian mechanics, the position q and momentum p , are defined as:

$$q = x, \quad (\text{C.2})$$

$$p = p_x. \quad (\text{C.3})$$

The transverse motion of a particle in the beam can be mapped onto a trajectory in the phase space. Particles in the beam occupy an area in the phase space. The shape of the area may change as the motion proceeds, but the area $\int p dq$ is conserved according to Liouville's theorem. The divergence x' is defined as

$$x' = \frac{dx}{dz} = \frac{p_x}{P}. \quad (\text{C.4})$$

With this, Liouville's theorem can be written as

$$\int p dq = P \int x' dx. \quad (\text{C.5})$$

The emittance $\pi\epsilon$ is defined as

$$\int x' dx = \pi\epsilon. \quad (\text{C.6})$$

In addition, the normalized emittance ϵ^* is defined as

$$\epsilon^* = \frac{cP}{mc^2}\epsilon. \quad (\text{C.7})$$

Thus Liouville's theorem is rewritten as

$$\int pdq = P \cdot \pi\epsilon = mc \cdot \pi\epsilon^*. \quad (\text{C.8})$$

Suppose particles in the beam are in simple harmonic motion with a wave length $\beta(s)$ which changes along the beam line s . Then the maxima of x and x' are

$$x_{\max} = \sqrt{\epsilon^*\beta(s)}, \quad (\text{C.9})$$

$$x'_{\max} = \sqrt{\frac{\epsilon^*}{\beta(s)}}. \quad (\text{C.10})$$

For head-on collisions of two bunches containing N of protons and \bar{N} of antiprotons the machine luminosity is given by

$$\mathcal{L} = f \frac{N\bar{N}}{A} \quad (\text{C.11})$$

where f is the frequency of beam crossing, and A is the effective area of the bunch-bunch overlap. N and \bar{N} can be directly obtained by measuring the circulating currents. In term of the transverse beam profiles for protons and antiprotons, $i(x, y)$ and $\bar{i}(x, y)$, the factor $\frac{1}{A}$ is given by

$$\frac{1}{A} = \frac{\int i(x, y) \cdot \bar{i}(x, y) dx dy}{\int i(x, y) dx dy \cdot \int \bar{i}(x, y) dx dy}. \quad (\text{C.12})$$

The transverse beam profiles are measured by the flying wire technique. In this method thin solid wires are swept through each beam fast enough not to disturb the beam and not to melt the wires themselves. By detecting the rate of beam-wire interactions with a suitable monitor, one can measure $i(x)$, $i(y)$, $\bar{i}(x)$, and $\bar{i}(y)$. Under the assumptions $i(x, y) = i_x(x) \cdot i_y(y)$ and $\bar{i}(x, y) = \bar{i}_x(x) \cdot \bar{i}_y(y)$, one can derive the factor $\frac{1}{A}$. We assume bi-Gaussians for the transverse beam profiles as follows:

$$i_x(x) = \frac{1}{\sqrt{2\pi}\sigma_x} \exp\left[-\frac{x^2}{2\sigma_x^2}\right], \quad (\text{C.13})$$

$$i_y(x) = \frac{1}{\sqrt{2\pi}\sigma_y} \exp\left[-\frac{y^2}{2\sigma_y^2}\right], \quad (\text{C.14})$$

$$\bar{i}_x(x) = \frac{1}{\sqrt{2\pi}\bar{\sigma}_x} \exp\left[-\frac{x^2}{2\bar{\sigma}_x^2}\right], \quad (\text{C.15})$$

$$\bar{i}_y(x) = \frac{1}{\sqrt{2\pi}\bar{\sigma}_y} \exp\left[-\frac{y^2}{2\bar{\sigma}_y^2}\right]. \quad (\text{C.16})$$

Then the effective area A is given by

$$A = 4\sqrt{\frac{\pi\sigma_x^2 + \pi\bar{\sigma}_x^2}{2} \cdot \frac{\pi\sigma_y^2 + \pi\bar{\sigma}_y^2}{2}}. \quad (\text{C.17})$$

The normalized emittances can be defined by the following geometrical relation:

$$\pi\sigma_x^2 = \beta_x\epsilon_x^*, \quad (\text{C.18})$$

$$\pi\sigma_y^2 = \beta_y\epsilon_y^*. \quad (\text{C.19})$$

Using the normalized emittances, we can express the effective area A as

$$A = 4\sqrt{\beta_x\beta_y} \sqrt{\frac{\epsilon_x^* + \bar{\epsilon}_x^*}{2} \cdot \frac{\epsilon_y^* + \bar{\epsilon}_y^*}{2}}. \quad (\text{C.20})$$

Therefore, the luminosity is written with beam parameters as

$$\mathcal{L} = f \frac{N\bar{N}}{\sqrt{\beta_x\beta_y} \sqrt{\frac{\epsilon_x^* + \bar{\epsilon}_x^*}{2} \cdot \frac{\epsilon_y^* + \bar{\epsilon}_y^*}{2}}}. \quad (\text{C.21})$$

The flying wires to measure the transverse beam profiles must be thin relative to the beam width. In addition, their speed of traversal is in practice forced to be very high to avoid melting the wire after a few traversals. Therefore, the accuracy of the flying wire method is likely to suffer from statistical limitations.

One can measure the luminosity in a collider not only by direct measurement of the beam parameters but also by measurement of a reaction with a known rate. We have used a combination of these methods to measure the integrated luminosity. The Tevatron run at two different energies, $\sqrt{s} = 546$ GeV and $\sqrt{s} = 1800$ GeV. We have used the interaction rate as measured with the BBC's at both energies, together with the beam parameters measured by the Fermilab Accelerator division. We have also used the $\bar{p}p$ cross sections measured by UA4 at the $S\bar{p}p$ S collider at CERN to calibrate our luminosity measurement.

By monitoring the rate of hits in the BBC's we have a reaction to which we can normalize all other cross section measurements. To get an absolute normalization of the BBC cross section σ_{BBC} , we use the rate seen by the BBC's and the luminosity measured with the beam parameters. The transverse beam profile is measured with flying wires. Resistive wall current monitors measure both bunch intensities and the longitudinal beam profile. The luminosity at B0 straight intersection is calculated from the beam profiles and the accelerator lattice function. The overall uncertainty on the accelerator luminosity is estimated to be 10%, and is independent of energy. At both $\sqrt{s} = 546$ GeV and $\sqrt{s} = 1800$ GeV, we measure the beam parameters and the rate in the BBC's (R_{BBC}). We are then able to measure how σ_{BBC} changes with \sqrt{s} , via the ratio of the accelerator luminosity (\mathcal{L}_{Tev}) calculated from beam parameters. The ratio has a systematic uncertainty free from the overall normalization uncertainty. By normalizing at $\sqrt{s} = 546$ GeV, where UA4 with similar geometry to the BBC's have been measured the $\bar{p}p$ cross sections, we can measure the effective cross section seen by the BBC's at $\sqrt{s} = 1800$ GeV and extract the integrated luminosity recorded. We use the relation

$$\frac{\sigma_{\text{BBC}}(1800 \text{ GeV})}{\sigma_{\text{BBC}}(546 \text{ GeV})} = \frac{\frac{R_{\text{BBC}}(1800 \text{ GeV})}{\mathcal{L}_{\text{Tev}}}}{\frac{R_{\text{BBC}}(546 \text{ GeV})}{\mathcal{L}_{\text{Tev}}}} = 1.30 \pm 0.06 \quad (\text{C.22})$$

to extrapolate the BBC cross section σ_{BBC} from 546 GeV to 1800 GeV.

The value of $\frac{R_{\text{BBC}}}{\mathcal{L}_{\text{Tev}}}$ at 1800 GeV has been corrected by $(-3 \pm 2)\%$ for dynamic beam-beam interaction effects, which change the focal properties of the Tevatron lattice. These effects predict linear or quadratic dependence of the ratio with the luminosity. The correction is extrapolated to low luminosity where the beam-beam effects are found to be negligible. The uncertainty of this correction comes from the difference between the linear and quadratic extrapolations.

We use two methods to calculate $\sigma_{\text{BBC}}(546 \text{ GeV})$. The first is to use the accelerator luminosity as calculated from the beam parameters. This method gives an effective BBC cross section of 32.8 ± 3.6 mb. The second method is to use values reported by the UA4 collaboration [54, 54]. The UA4 experiment used trigger counters similar in geometry to the BBC's. From UA4 measurements, the effective cross section of the double-arm coincidence is

$\sigma_{\text{DA}} = 38.9 \pm 1.8$ mb. Using the MBR Monte Carlo simulation which generates minimum bias events, we then calculate the relative acceptance of the BBC's to the UA4 trigger counters. This correction is necessary because the UA4 trigger counters cover a different geometrical area ($3.0 < |\eta| < 5.6$) from the BBC's ($3.3 < |\eta| < 5.9$). The correction due to different η coverage is $(-2.1 \pm 2.1)\%$.

We also correct for the inefficiencies in the BBC's due to radiation damage suffered during the course of the data taking. Radiation damage at 1800 GeV are measured from data triggered solely on beam crossings. The magnitude of this correction at 1800 GeV is -0.7% . This inefficiency is extrapolated to 546 GeV by using the MBR Monte Carlo simulation, giving an inefficiency of $(2.2 \pm 2.2\%)$.

The value for $\sigma_{\text{BBC}}(546 \text{ GeV})$ from this method is

$$\sigma_{\text{BBC}}(546 \text{ GeV}) = 0.979 \times 0.978 \times 38.9 \text{ mb} = 37.2 (\pm 5.3\%) \text{ mb.} \quad (\text{C.23})$$

To derive the final value of $\sigma_{\text{BBC}}(546 \text{ GeV})$, we average the measurements from the accelerator calculation and the UA4 normalization weighted by their respective uncertainties. In summary, we obtain $\sigma_{\text{BBC}}(546 \text{ GeV}) = 36.2 \pm 1.7$ mb. We calculate $\sigma_{\text{BBC}}(1800 \text{ GeV}) = 47.0 \pm 2.21 \pm 2.17$ mb, where the first error represents the contribution from $\sigma_{\text{BBC}}(546 \text{ GeV})$ and the second error is the contribution from the luminosity ratio. Thus we can get the luminosity \mathcal{L} from the BBC cross section σ_{BBC} and the BBC trigger rate R_{BBC} as

$$\mathcal{L} = \frac{R_{\text{BBC}}}{\sigma_{\text{BBC}}}. \quad (\text{C.24})$$

Bibliography

- [1] C.Kourkouvelis *et al.*, *Z. Phys.* C16 (1982) 101.
- [2] AFS Collaboration, T.Akesson *et al.*, *Z. Phys.* C32 (1986) 491.
- [3] NA3 Collaboration, J.Badier *et al.*, *Phys. Lett.* 164B (1985) 184.
- [4] WA70 Collaboration, E.Bonvin *et al.*, *Z. Phys.* C41 (1989) 591.
- [5] WA70 Collaboration, E.Bonvin *et al.*, *Phys. Lett.* B236 (1990) 523.
- [6] UA1 Collaboration, C.Albajar *et al.*, *Phys. Lett.* B209 (1988) 385.
- [7] UA2 Collaboration, J.Alitti *et al.*, *Phys. Lett.* B288 (1992) 386.
- [8] F.Abe *et al.*, *Nucl. Instrum. Methods* A271 (1988) 387.
- [9] F.Snider *et al.*, *Nucl. Instrum. Methods* A268 (1988) 75.
- [10] F.Bedeschi *et al.*, *Nucl. Instrum. Methods* A268 (1988) 50.
- [11] S.Bhadra *et al.*, *Nucl. Instrum. Methods* A268 (1988) 92.
- [12] L.Balka *et al.*, *Nucl. Instrum. Methods* A267 (1988) 272.
- [13] K.Yasuoka *et al.*, *Nucl. Instrum. Methods* A267 (1988) 315.
- [14] Y.Fukui *et al.*, *Nucl. Instrum. Methods* A267 (1988) 280.
- [15] G.Brandenburg *et al.*, *Nucl. Instrum. Methods* A267 (1988) 257.
- [16] S.Bertolucci *et al.*, *Nucl. Instrum. Methods* A267 (1988) 301.

- [17] S.Cihangir *et al.*, Nucl. Instrum. Methods A267 (1988) 249.
- [18] G.Ascoli *et al.*, Nucl. Instrum. Methods A268 (1988) 33.
- [19] L.Byrum *et al.*, Nucl. Instrum. Methods A268 (1988) 46.
- [20] G.Drake *et al.*, Nucl. Instrum. Methods A269 (1988) 68.
- [21] E.Barsotti *et al.*, Nucl. Instrum. Methods A269 (1988) 82.
- [22] D.Amidei *et al.*, Nucl. Instrum. Methods A269 (1988) 51.
- [23] G.W.Foster *et al.*, Nucl. Instrum. Methods A269 (1988) 93.
- [24] CDF Collaboration, F.Abe *et al.*, Phys. Rev. Lett. 68 (1992) 2734.
- [25] CDF Collaboration, F.Abe *et al.*, Phys. Rev. D48 (1993) 2998.
- [26] CDF Collaboration, F.Abe *et al.*, Phys. Rev. Lett. 40 (1989) 3791.
- [27] Particle Data Group, K.Hisaka *et al.*, Phys. Rev. D45 (1975).
- [28] R.Brun *et al.*, CERN-DD/EE/84-1.
- [29] E.Longo and I.Sestili, Nucl. Instrum. Methods 128 (1975) 283.
- [30] S.Miyashita, in *Proceedings of the XXIIIrd Rencontre de Moriond, Les Arcs, France, 1988*, edited by J.Tran Thanh Van (Editions Frontières, Gif-sur-Yvette, France, 1988).
- [31] CDF Collaboration, F.Abe *et al.*, Phys. Rev. D45 (1992) 1448.
- [32] CDF Collaboration, F.Abe *et al.*, Phys. Rev. D44 (1991) 29.
- [33] CDF Collaboration, F.Abe *et al.*, Phys. Rev. Lett. 70 (1993) 4042.
- [34] CDF Collaboration, F.Abe *et al.*, Phys. Rev. Lett. 66 (1991) 2951.
- [35] P.Arnold and M.H.Reno, Nucl. Phys. B319 (1989) 37.
- [36] P.Arnold and M.H.Reno, Nucl. Phys. B330 (1990) 284.

- [37] P.Arnold and R.P.Kauffman, *Phys. Lett.* B349 (1991) 381.
- [38] D.Antreasyan *et al.*, *Phys. Rev. Lett.* 47 (1981) 12.
- [39] E.Eichten, I.Hinchliffe, K.Lane, and C.Quigg, *Rev. Mod. Phys.* 56 (1984) 579.
- [40] E.Eichten, I.Hinchliffe, K.Lane, and C.Quigg, *Rev. Mod. Phys.* 58 (1984) 1065.
- [41] D.W.Duke and J.F.Owens, *Phys. Rev.* D30 (1984) 49.
- [42] P.N.Harriman, A.D.Martin, R.G.Roberts, and W.J.Stirling, *Phys. Rev.* D42 (1990) 798.
- [43] T.Ferbel and W.R.Molzon, *Rev. Mod. Phys.* 56 (1984) 181.
- [44] J.F.Owens, *Rev. Mod. Phys.* 59 (1987) 465.
- [45] E.L.Berger, E.Braaten, and R.D.Field, *Nucl. Phys.* B239 (1984) 52.
- [46] T.Sjöstrand, *PYTHIA 5.6 and JETSET 7.3 Physics and Manual*, CERN-TH.6488/92 (1992).
- [47] T.Sjöstrand, *Computer Physics Commun.* 39 (1986) 347.
- [48] T.Sjöstrand and M.Bengtsson, *Computer Physics Commun.* 43 (1987) 367.
- [49] H.-U.Bengtsson and T.Sjöstrand, *Computer Physics Commun.* 46 (1987) 43.
- [50] B.L.Combridge, *Nucl. Phys.* B174 (1980) 243.
- [51] A.P.Contogouris, N.Mebarki, and H.Tanaka, *Phys. Rev.* D35 (1987) 1590.
- [52] B.Bailey, J.F.Owens, and J.Ohnemus, *Phys. Rev.* D46 (1992) 2018.
- [53] P.Aurenche, R.Baier, A.Douiri, M. Fontannaz, and D.Schiff *Z. Phys.* C29 (1985) 459.
- [54] UA4 Collaboration, M.Bozzo *et al.*, *Phys. Lett.* 147B (1984) 392.
- [55] UA4 Collaboration, D.Bernard *et al.*, *Phys. Lett.* 198B (1987) 583.